ATLAS NOTE

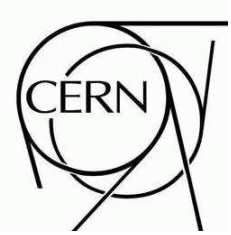

14th December 2007

Local Hadronic Calibration of Single Pion Data from the Combined ATLAS Testbeam of 2004

ATL-CAL-PUB-2007-001
18 December 2007

E. Bergeaas[1], Ç. İşsever[2], K. Jon-And[1], B.T. King[3],
K. Lohwasser[2], D. Milstead[1]

[1] *Stockholm University* [2] *University of Oxford* [3] *University of Liverpool*

Abstract

For the first time, the local hadronic calibration scheme has been applied to real data from the combined test beam of 2004. In this note, the performance of the weighting of the combined test beam data is shown in relation to Monte Carlo simulations. The performance of the local calibration scheme when applied to simulated jets in full ATLAS set-up has also been demonstrated, and compared with the current default jet calibration, the "global" method.

The local hadronic calibration achieves a calorimeter linearity within 3%, and the linearities of simulation and test beam data after weighting are in agreement. The calibration improves the resolution of simulated test beam data for beam energies larger than 8 GeV, and energies larger than 20 GeV for the data.

In addition, the local hadronic calibration is shown to be a stable method for compensating the calorimeter system of ATLAS.

Contents

1 Introduction

ATLAS, A Toroidal LHC ApparatuS, is a general-purpose detector, currently under construction at the Large Hadron Collider (LHC) at CERN, designed to fully exploit the potential of the high-energy proton-proton collisions. The calorimeters of ATLAS, the sub-detectors used to measure the energy of the collision products, are non-compensating, and thus some of the energy deposited by hadrons is fundamentally undetectable by the calorimeters. When the calorimeters have been calibrated on the electromagnetic scale, the energy of electrons, positrons and photons is correctly reconstructed. However, the reconstructed energy of hadrons of the same nominal energy is lower, for the ATLAS calorimeters typically by a factor of 10 to 20% [1]. The reasons for this behaviour of the hadrons are explained in Section 2, where the calorimeters of ATLAS are also described in greater detail. Obtaining the correct energy scale for hadrons from the electromagnetic energy scale is an important step in the process of calibrating non-compensating calorimeter systems.

The current default method for calibrating hadronic jets in ATLAS is a global method, the so-called global H1 scheme, where the reconstructed energy of a jet is optimised with respect to the full energy deposited, as obtained from simulation [2, 3]. This method compensates for detector and physics effects in one step, making the scheme dependent on the jet algorithm and the physics sample used.

In contrast, the local hadronic calibration schemes aim to apply weights not to large objects like jets, but instead calibrate topological clusters [1)] in the calorimeter before constructing physics objects like jets. The advantage of such an approach is that the corrections can be modular, i.e. the correction for hadronic invisible energy loss is made independently of correction for energy losses in dead regions of the detector, or leakage. The local corrections are also totally independent of jet algorithms, but corrections for biases introduced by the physics reconstruction algorithms must be applied separately. The local calibration is, as all methods used for calibrating non-compensating calorimeters, based on simulations only, and a good understanding of the precision with which the Monte Carlo simulations can describe real data is needed. Thus it is crucial to test the local hadronic calibration schemes on real data whenever possible.

In this note we describe a method for local hadronic calibration of single pions in the ATLAS calorimeter system using a non-iterative software compensation technique, by weighting the energy on cell level. This method has been successfully applied to the liquid argon calorimeters of the H1 detector at HERA [6, 7].

[1)] Topological clusters are formed from energy depositions in the calorimeter cells, based on their energy content and closeness to neighbours. See section 3 and references [4, 5].

To obtain the weights, we have simulated the response to single pions in a test-beam environment. The development of the weights is described in Section 3, where we also demonstrate the performance of the weights on an independent simulated sample.

In Section 4 we present the results of applying these weights on real data from the combined testbeam runs at the H8 beam line in 2004. The opportunity to try the method on real data from single pions of known energy in a controlled environment is the main reason for doing the simulation study in the test-beam environment, rather than in a simulation of the full ATLAS set-up[2)].

To check the stability of the method, we have deliberately altered and distorted the weights in various ways and the results of these studies can be found in Section 5. In that section, we also compare our results with other methods for hadronic calibration, in particular the current default version of local calibration, where the global energy scale is the energy of a single cluster [8].

In Section 6, the local hadronic calibration is applied to simulated jets in full ATLAS set-up, and comparisons with the performance of the global H1 scheme are given.

The Monte Carlo sample used for the derivation of the weights has been simulated using the simulation toolkit GEANT4 [9] within the ATHENA framework [10]. The test beam was simulated with ATHENA version 11.0.42, see Section 2.4 for details. For the simulation of jets in the full ATLAS set-up, ATHENA version 12 was used, see Section 6.

2 The ATLAS detector at LHC

ATLAS, A Toroidal LHC ApparatuS, is a general-purpose detector currently being built at the Large Hadron Collider, LHC, at CERN. LHC is scheduled to start in 2008 and will provide proton-proton collisions at 14 TeV centre-of-mass energy. The design luminosity is 10^{34} cm^{-2} s^{-1}, and the collisions will happen every 25 ns [11]. The ATLAS detector is designed to fully take advantage of the discovery potential of new physics at such high energies [12].

ATLAS has a cylindric shape with an outer radius of approximately 11 metres, a length of 46 metres and a total weight of 7000 tonnes. The main sub-systems are, in order from smaller to larger radii, the inner detector, the electromagnetic calorimeters, the hadronic calorimeters and the muon system [13].

The inner detector has a cylindric shape of radius 1.15 m. and length 7 m. The purpose of the inner detector is to measure track and vertex positions of the particles created in the collisions. The calorimeter system of ATLAS consists of several non-compensating sampling calorimeters, which are described in Section 2.1. The outer radius of the calorimeter system is 4.25 m and its length is 12.20 m. The outer part of the ATLAS detector consists of the muon system, where the momenta of muons escaping the calorimeters are measured.

[2)] Studies of local calibration in full ATLAS set-up are in progress, see for example [8].

In the coordinate system of ATLAS, the z-axis is along the beam pipe, the x-axis points towards the center of the LHC ring and the y-direction is upwards. These directions form a right-handed coordinate system. In polar coordinates, the angle θ is the polar angle to the beam pipe, and ϕ is the angle in the x-y-plane. The polar angle can be used to compute the pseudorapidity η, where

$$\eta = -\ln\left(\tan\left(\frac{\theta}{2}\right)\right). \tag{1}$$

For high-energetic particles, the pseudorapidity is a good approximation of the rapidity y, $y = \frac{1}{2}\ln\left(\frac{E+p_L}{E-p_L}\right)$, where E is the energy of the particle and p_L the momentum component along the beam [14].

2.1 The ATLAS calorimeter system

The calorimeter system of ATLAS consists of several non-compensating sampling calorimeters. Detailed descriptions of the calorimeters can be found in [1, 15, 16].

In the central part of the detector, at low $|\eta|$, the innermost calorimeter is the electromagnetic liquid argon calorimeter (in this note referred to as "LAr"), which is subdivided into the barrel part at $|\eta| < 1.475$ and the endcap at $1.375 < |\eta| < 3.2$. The electromagnetic LAr calorimeter uses liquid argon as active material and lead as absorber. The electrodes are folded in an accordion shape, to ensure full ϕ coverage. In Figure 1, an overview of a LAr barrel module is given. The first sampling layer in the LAr barrel consists of the strips, which are very fine-grained in η, with a granularity of $\Delta\eta \times \Delta\phi \times \Delta r = 0.0031 \times 0.098 \times 4.3X_0$. One interaction length X_0 in the LAr barrel module is approximately 21.1 mm. The typical cell volume in this layer is between 92,000 and 155,000 mm^3, where the larger cells are found at higher η. The second sampling layer, the middle one, has the granularity $\Delta\eta \times \Delta\phi \times \Delta r = 0.025 \times 0.0245 \times 16X_0$. In cell volume, this corresponds to sizes between 640,000 and 720,000 mm^3. The granularity of the third, back, sampling layer is $\Delta\eta \times \Delta\phi \times \Delta r = 0.05 \times 0.0245 \times 2X_0$, with typical cell volumes between 350,000 and 900,000 mm^3.

The LAr barrel calorimeter is surrounded by a cryostat which cools the liquid argon. The inner radius of the cryostat is 1385 mm, and its outer radius is 2132 mm. Inside the cryostat close to the inner wall, the LAr pre-sampler (sometimes referred to as "LAr0") is placed. Its purpose is to correct for energy losses before the calorimeters. See also Section 4.4 for the usage of the pre-sampler information.

Outside the electromagnetic LAr calorimeter, the hadronic calorimeter system is placed. At $|\eta| < 1.7$, the calorimeter is made out of iron with scintillator tiles as active medium, and it is often referred to as the "Tile" calorimeter. Its inner and outer radii are 2280 and 4230 mm, respectively. The Tile barrel covers the $|\eta| < 1.0$ region, and the Tile parts at $0.8 < |\eta| < 1.7$ is the extended barrel. A Tile barrel module is divided into three longitudinal segments, or sampling layers, which from smaller to larger radii are the A-cells, the BC-cells and the D-cells, see Figure 2 for an overview. The granularity is $\Delta\eta \times \Delta\phi = 0.1 \times 0.1$ for the A-cells and the BC-cells, and $\Delta\eta \times \Delta\phi = 0.2 \times 0.1$ for the D-cells. The volumes of the A-cells are between

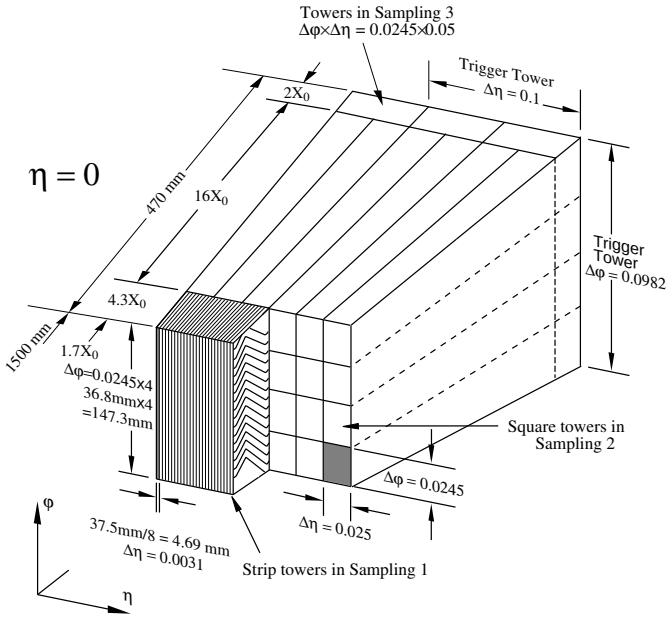

Figure 1: Layout of a LAr barrel module. See text for cell sizes and layer descriptions. (Figure from [15]).

$18 \cdot 10^6$ and $24 \cdot 10^6$ mm^3. The BC-cells are slightly larger at $30 \cdot 10^6 - 90 \cdot 10^6$ mm^3, and the D-cells are the largest ones at $105 \cdot 10^6 - 135 \cdot 10^6$ mm^3.

Some distance from the interaction point in the z direction and at high η values, the hadronic endcap (HEC) and the forward calorimeters (FCAL) are placed. These calorimeters are placed inside the same cryostat as the LAr endcap calorimeter. The HEC, that covers the $1.5 < |\eta| < 3.2$ range, is a copper/LAr calorimeter with an outer radius of 2.03 m. At the highest η values, between 3.1 and 4.9, the forward calorimeter is placed. The absorber material in the forward calorimeter is copper in the section closest to the interaction point, and tungsten in the other sections.

For the study described in Sections 3-5, simulations and results from the combined test-beam of 2004 have been analysed. Only runs with beams targeted at the region of the calorimeter that will correspond to $\eta = 0.45$ in the final detector have been considered. This part is in the barrel region, and thus only read-out from the LAr and Tile barrel calorimeters will be used. The full ATLAS study described in Section 6 uses simulations of jets in all calorimeters.

2.2 Energy deposition in the calorimeters

Calorimeters detect energy through total absorption of the particles. High-energy positrons or electrons lose their energy through bremsstrahlung, which gives rise to an electromagnetic energy shower in the calorimeter. High-energy hadrons can lose their energy in many different

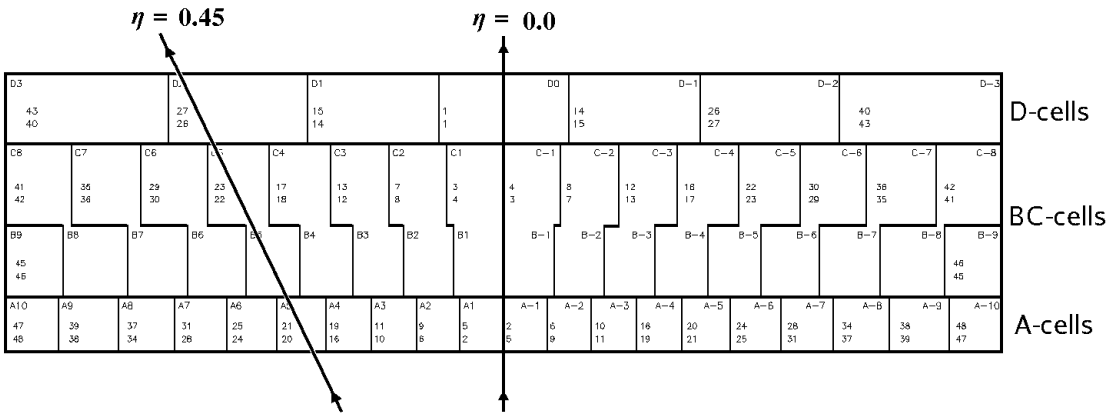

Figure 2: Layout of a Tile barrel module. See the text for a description of the layers and the cell sizes. The runs used for the analysis are targeted at $\eta = 0.45$, as indicated. (Modification of a figure from [16]).

ways, for example via ionisation (if the hadron is charged) or through strong interactions. The nature of the strong interactions a hadron might undergo in the calorimeter material is such that some of the energy dissipated that way is invisible to the calorimeter, such as energy lost in nuclear break-ups.

The fraction of the hadron energy that can be detected by the calorimeters depends on the initial energy of the hadron, where larger initial hadron energy means that a larger percentage of the total energy will be detected by the calorimeter. This is an effect of more neutral pions being produced in the hadronic shower when the energy of the initial hadron is higher. Once a π^0 is formed, it no longer gives rise to secondary hadrons but rapidly decay into two photons, and all its energy is deposited electromagnetically [17].

The undetected energy of hadronic showers is called *invisible energy*, as opposed to the *visible energy* that can be detected. When a non-compensating calorimeter is calibrated on the *electromagnetic scale*, the electromagnetic showers are correctly calibrated, while the invisible energy is still unaccounted for. Some particles, mostly neutrinos, leave the detector completely undetected, and the energy loss they represent is called *escaped energy*.

Electromagnetic showers are shorter and denser than hadronic ones as a consequence of the different processes involved. Due to the production of neutral pions in the hadronic showers, the visible energy fraction fluctuates heavily from event to event, which results in a worse energy resolution for hadrons compared to electrons.

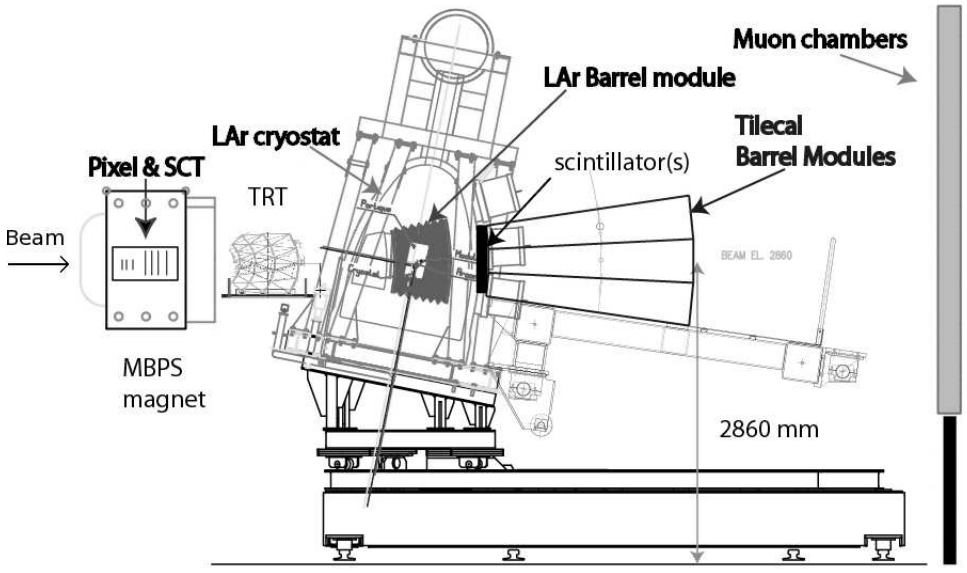

Figure 3: Set-up of the 2004 combined test-beam. The beam direction is from left to right in the figure. (Figure from [18]).

2.3 The 2004 ATLAS combined test-beam

In the autumn of 2004, a slice of the barrel section of the ATLAS detector was tested in a combined sub-detector test beam, thus testing parts of the inner detector, the pre-sampler, the LAr barrel, the Tile barrel and the muon chambers together [18]. In Figure 3, a schematic view of the combined test beam set-up is shown, and Figure 4 shows the relative positions of the calorimeter sampling layers. The combined test beam of the barrel parts of ATLAS was performed in the H8 beam line, using beams created by the Super Proton Synchrotron SPS at CERN [19].

For the analysis presented in this note, we have used information from the calorimeter read-out of the test-beam, as well as information from muon detection scintillators. Due to an instability in the read-out from the inner detector, signals from that sub-detector are unreliable for some of the runs in the early data taking period [20]. Since we want to treat all runs as similarly as possible, we need to make the same cuts on all runs. Thus no information from the inner detector is used in this analysis.

2.4 Simulation and real data from the combined test beam

The Monte Carlo samples used to make the hadronic compensation factors consist of $10,000$ events from 53 different energies in the range 0.5-316.23 GeV. The energies are 0.5, 0.75, 1.0, 1.12, 1.26, 1.41, 1.6, 1.77, 2.0, 2.24, 2.51, 2.82, 3.16, 3.55, 4.0, 4.467, 5.0, 5.623, 6.0, 7.0, 7.94,

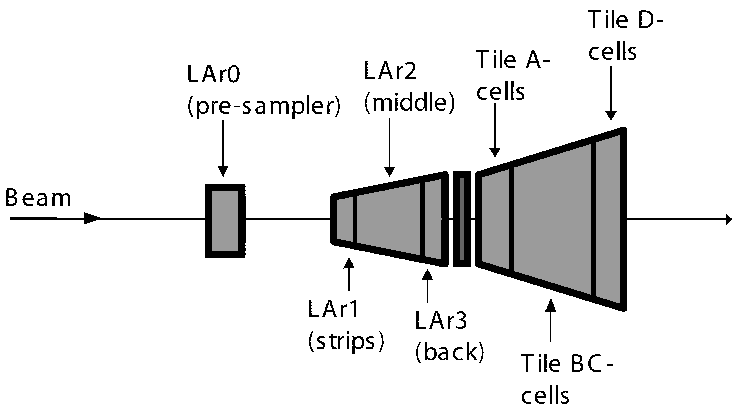

Figure 4: Schematic drawing of the relative positions of the calorimeters in the combined test beam of 2004, with the calorimeter sampling layers indicated. The beam direction is from left to right in the figure. It should be noted that this figure is only approximately to scale. In the direction of the beam, the sampling layers are LAr0 (pre-sampler), LAr1 (strips), LAr2 (middle), LAr3 (back), Tile A-cells, Tile BC-cells, Tile D-cells. (Adaptation of a figure from [18]).

9.0, 10.0, 11.22, 12.59, 14.13, 15.85, 17.78, 20.0, 22.39, 25.0, 28.18, 30.0, 35.48, 40.0, 44.67, 50.0, 56.23, 60.0, 70.0, 80.0, 90.0, 100.0, 112.20, 125.89, 141.25, 158.49, 180.0, 200.0, 223.87, 250.0, 281.83 and 316.23 GeV. The energies are chosen to be logarithmically equidistant. In addition to these events, 10,000 extra events of the same energies, independent of the first sample, were also produced for systematic studies. 20,000 events of the beam energies 1.5, 3, 15, 150 and 300 GeV were also produced.

The simulations, digitizing and reconstructions were done using ATHENA version 11.0.42, which employs the GEANT4 simulation engine[3)].

From the real data of the combined test beam of 2004, seven runs have been used in this note, two high-energetic negative pion runs at 180 and 250 GeV respectively, three positive pion runs at 20, 50 and 100 GeV, one positron run at 180 GeV, and one low-energetic negative run at 9 GeV with a mixture of electrons and pions. From each of the runs, 10,000 events have been reconstructed using ATHENA version 11.0.41[4)]. See Section 4 for a full description of the runs used and the cuts implemented to clean the data.

The 100 GeV π^+ real data run, run 2102355, is the run on which the simulations are based, i.e. all beam line scintillators, beam chambers etc. in simulation are placed as for run 2102355.

[3)]The full version number for the GEANT4 release used by default in ATHENA version 11.0.4 is geant4.7.1.p01.clhep1.9.2.1, see [21].

[4)]The only difference between version 11.0.41 and 42 lies in the simulation stage, since .42 contains a GEANT bug fix. This means that reconstructions with 11.0.41 and .42 are equivalent.

3 Development of the weights

As described in the previous section, the calorimeters of ATLAS are non-compensating, i.e. some of the energy deposited by hadronic showers is undetectable by the calorimeters.

In this analysis, we start from topological clusters [4,8], (often referred to as "topo clusters") which are formed by selecting calorimeter cells with an energy signal larger than 4σ over the noise level. The cluster is then expanded in three dimensions by including all neighbouring cells with an energy signal larger than 2σ over noise. When no more neighbouring cells that fulfill the selection criterion can be found, all cells on the cluster perimeter, regardless of energy, are added to the cluster. Finally, if the topo cluster contains more than one cell with energy deposition larger than all its immediate neighbours, the cluster is split to separate the local energy maxima within the cluster, so that each final cluster only contains one energy maximum. The splitting only occurs if the local energy maxima is larger than 500 MeV.

The topo clusters have been calibrated on the electromagnetic scale [1,16], so that the energy from electrons and photons is given correctly, while the hadronic energy is too low. We achieve compensation for the invisible hadronic energy loss by applying a weight to the electromagnetic scale cell energy. The weights have been determined from simulated samples, as the mean of the ratio $E^{truth}_{cell}/E^{0}_{cell}$,

$$w_{cell} = \langle E^{truth}_{cell}/E^{0}_{cell} \rangle, \tag{2}$$

where E^{truth}_{cell} is the energy truly deposited in the cell, as given from the simulation, and E^{0}_{cell} is the reconstructed energy on the electromagnetic scale.

In this section, we discuss the choice of weight parametrisation, take a closer look at the parameters chosen, give a brief overview of noise estimations and finally determine the weight tables given in Section 3.5. In Section 3.6, the performance of the weights when applied to independent simulated samples is shown.

3.1 Weight parametrisation

As mentioned in Section 2.2, the fraction of the hadron energy that can be detected by the calorimeters depends on the initial energy of the hadron, where larger initial hadron energy means that a larger percentage of the total energy can be detected by the calorimeter.

In order to compensate for the invisible hadronic energy loss we face two problems: we must find a way to select the hadrons, since we do not want to disturb the energy deposited by electrons and photons, and we must find a way to estimate the total energy of the incoming hadron.

From Section 2.2 we know that the shower from a photon or an electron is more dense than the shower from a hadron. Thus the energy density in a cell within an electromagnetic shower is, on average, larger than the energy density in a cell within a hadronic shower. This relation can be used to separate hadrons from electrons or photons. The total energy of the incoming

hadron can be estimated as the reconstructed electromagnetic energy in the topo clusters that fall within a cone around the most-energetic cluster of the event, see Section 3.3.

In order to separate hadrons from photons/electrons and also keep track of the initial hadron energy, the weights have been parametrised with the cell energy density and the cone energy.

3.2 Energy density

The cell energy density, $\rho_E = E^0_{cell}/V_{cell}$, where E^0_{cell} is the energy recorded in the cell which is calibrated on the electromagnetic scale and V_{cell} the cell volume, can be used to distinguish electromagnetic showers from hadronic ones, as described in the previous section. In Figures 5 and 6, the cell energy densities for the various layers of the calorimeters, as given by a pion beam of initial energy 10 GeV, are shown. All cells that fall within a topo cluster have been included. For comparison, the cell energy densities from a 100 GeV beam are shown in Figures 7-8.

From Figures 5-8 we can see some general trends in the cell energy density distributions. In the 10 GeV beam case, the highest densities are found in layer 1 of the electromagnetic calorimeter (the strips). These cells are closest to the impact point. Then the maximal energy densities found are smaller the farther away from the impact point we get. For the 100 GeV beam, this pattern is changed. The maximal energy densities are recorded in layer 2 of the electromagnetic calorimeter, although they are only slightly larger than the energy densities found in layer 1. This reflects the development of the shower in the calorimeter, where the shower penetrates deeper in the calorimeter the more energetic the initial particle is. We also see that the maximal cell energy density in the electromagnetic calorimeter is approximately 0.02 MeV/mm^3 for the 10 GeV beam, and about 0.08 MeV/mm^3 in the 100 GeV case. For Tile, these values are $4.5 \cdot 10^{-4}$ MeV/mm^3 (10 GeV events) and $4.5 \cdot 10^{-3}$ MeV/mm^3 (100 GeV events). The difference in energy density values recorded in the various calorimeters is mainly an effect of the difference in cell volumes, since the cells of the Tile calorimeter are about two orders of magnitude larger than the cells of the LAr calorimeter, see Section 2.1. A comparison between the energy density from 10 and 100 GeV beams is given in Figures 9-10. These histograms are not normalised, but reflect the differences at the various beam energies. In the 100 GeV beam, the maximum energy density deposited in any cell is significantly larger than in the 10 GeV beam, and the number of cells involved in the hadronic shower is larger.

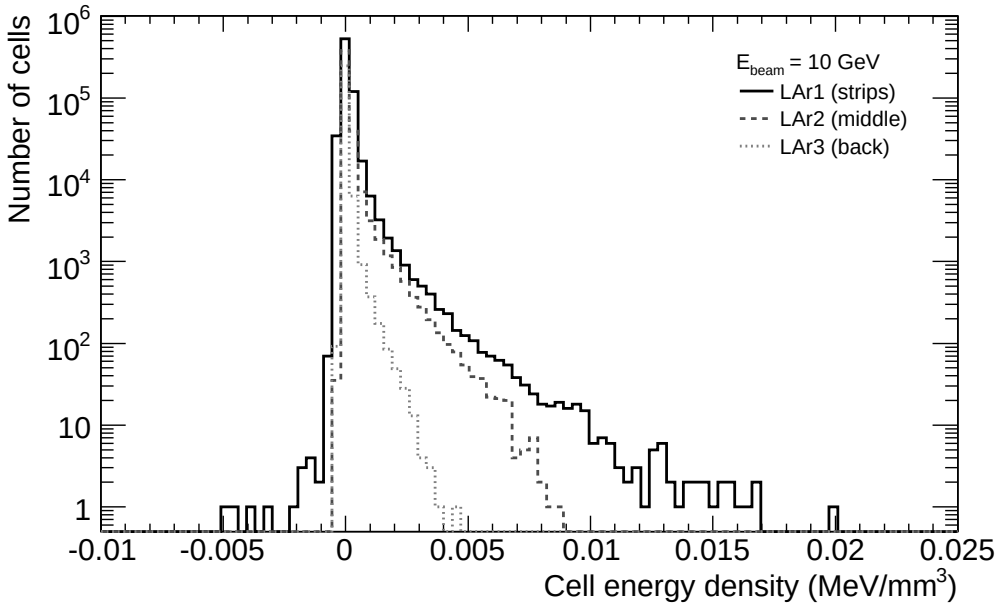

Figure 5: Cell energy density distribution in the various LAr sampling layers, for a 10 GeV pion beam.

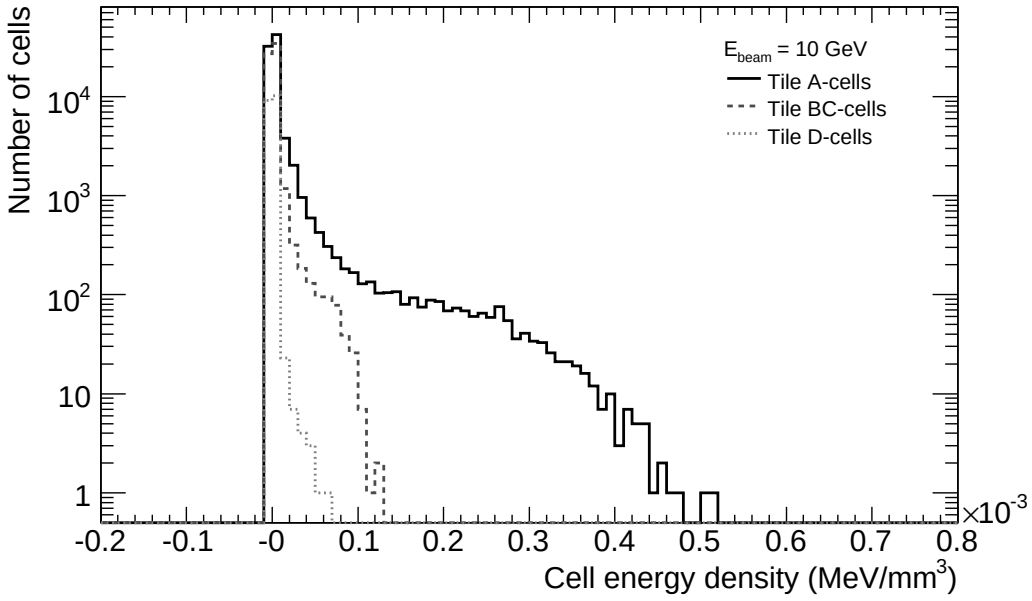

Figure 6: Cell energy density distribution in the various Tile sampling layers, for a 10 GeV pion beam.

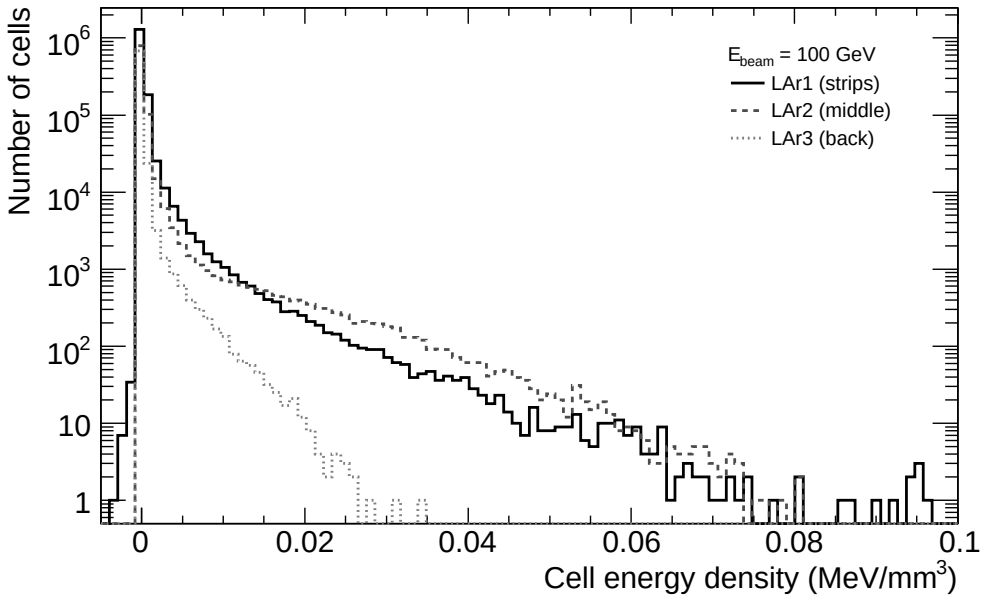

Figure 7: Cell energy density distribution in the various LAr sampling layers, for a 100 GeV pion beam.

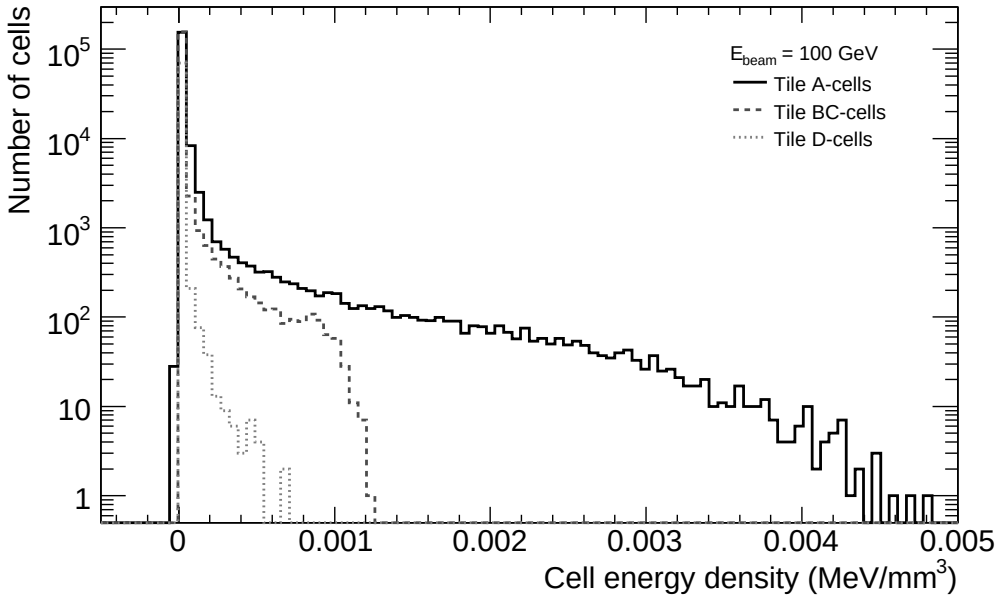

Figure 8: Cell energy density distribution in the various Tile sampling layers, for a 100 GeV pion beam.

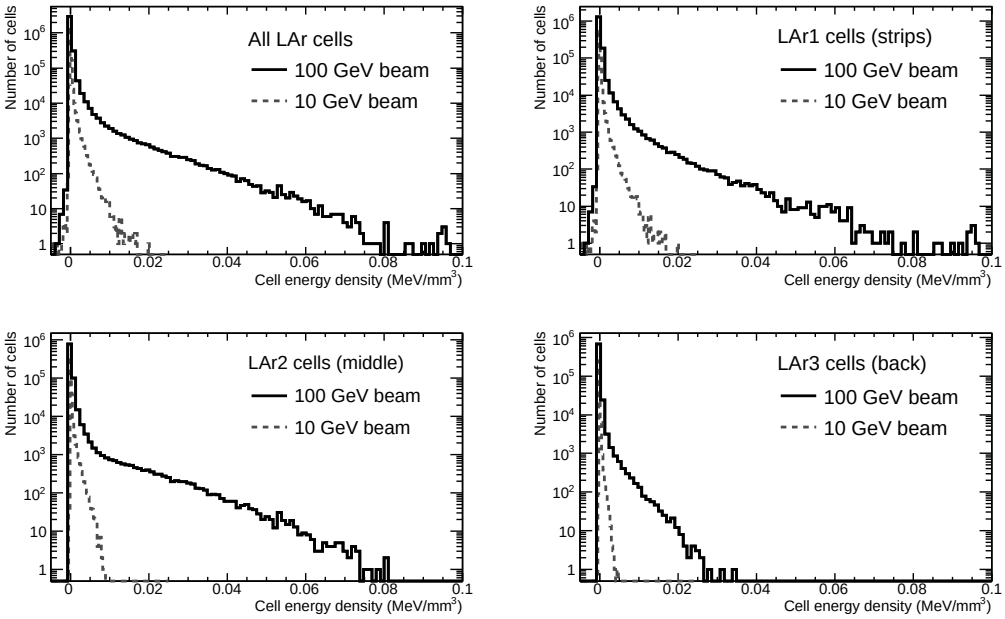

Figure 9: Cell energy density distribution in the various LAr sampling layers. Comparison between the energy densities in a 10 GeV and a 100 GeV pion beam.

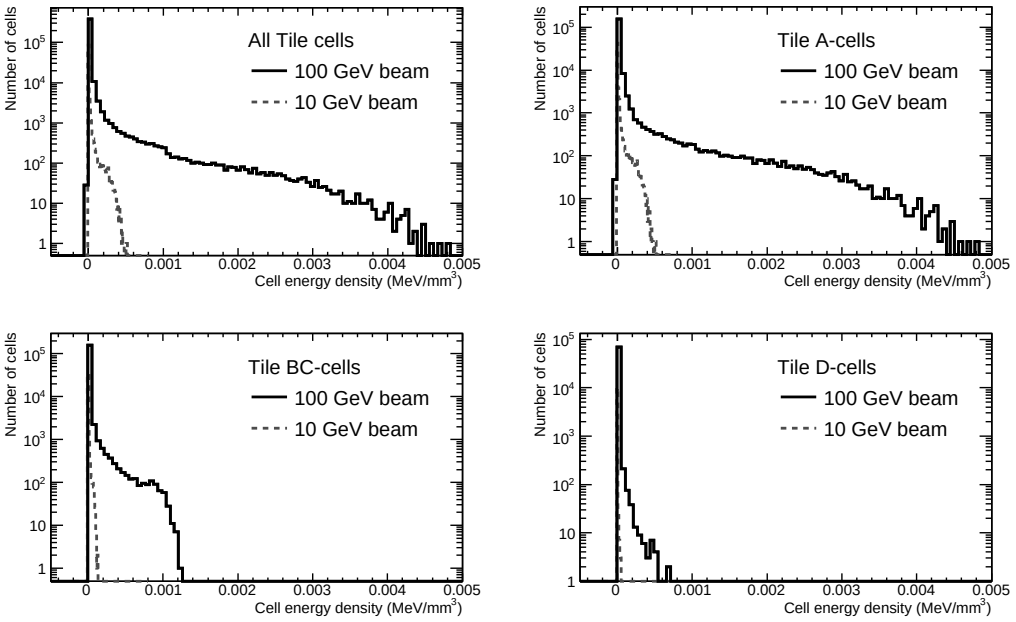

Figure 10: Cell energy density distribution in the various Tile sampling layers. Comparison between the energy densities in a 10 GeV and a 100 GeV pion beam.

3.3 Cone energy

The energy of all clusters that fall within a cone is the second parameter of the weights. The cone energy is determined in the following way:

- Find the topo cluster with the highest energy in the calorimeter.
- Draw a cone axis through the most energetic cluster and the primary vertex.
- Make a cone with an opening angle (i.e. angle between axis and cone surface) of 11 degrees around the axis. Include all topo clusters whose energy center-of-mass falls within the cone and sum their energies.

If some of the clusters of the event fall outside the most energetic cone, these steps are repeated to make secondary cones, including only clusters that belong to no other cone.

When computing the weights, only the primary, most energetic, cone is considered. Since the most energetic cone generally contains all or almost all of the single pion energy of the event, this is a fair estimation of the beam energy. If secondary cones are present, they occur in the outskirts of the shower. The physical processes there are different from the ones in the core, and the fluctuations there are larger, generally giving a lower hadronic energy content. If included, weights derived from low-energy secondary cones from high-energy events could distort the weight tables for the low-energy regions.

Distributions of cone energies for a 10 GeV beam and a 100 GeV beam are shown in Figures 11-12. The energy of the primary cone divided by the beam energy is given as a function of the beam energy in Figure 13, as well as a comparison with the fraction of the beam energy that is reconstructed on the electromagnetic scale. The majority of the electromagnetic scale energy of each event fall within the primary cone, as demonstrated.

3.4 Noise considerations

Both when computing and applying the weights, noise considerations play an important role. Quite naturally, it does not make sense to apply hadronic weights to a cell dominated by noise. There are also good reasons to take care not to use noisy cells for derivation of the compensation factors. The Monte Carlo samples used to determine the weights have simulated noise included in the reconstructed (data-like) energy. This is necessary to get a clustering of the cells as similar to the one in data as possible. However, when the weights are computed as the mean of the ratio between the energy truly deposited and the energy reconstructed on the electromagnetic level, $w_{cell} = \langle E_{cell}^{truth} / E_{cell}^{0} \rangle$, inclusion of noisy cells will give a lowering of the weights, which comes from the cells with a signal just above the noise cut threshold. Let us consider a cell with a small electromagnetic energy deposition slightly above the noise cut. The ideal weight of this cell would be $w_{cell} = 1$, but due to the Gaussian smearing of the signal, E_{cell}^{0} can be both slightly larger and slightly smaller than E_{cell}^{truth}. However, since the signal is just above the noise threshold, the occasions when $E_{cell}^{truth} > E_{cell}^{0}$ will be removed, leaving a bias towards high E_{cell}^{0}

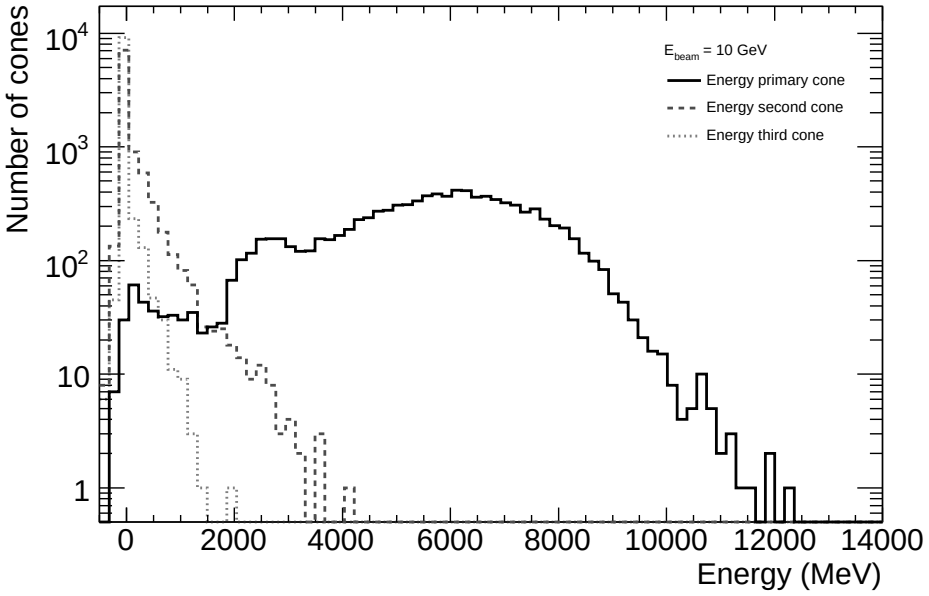

Figure 11: Cone energy distribution in a 10 GeV beam. The energy distributions of the first three cones are displayed.

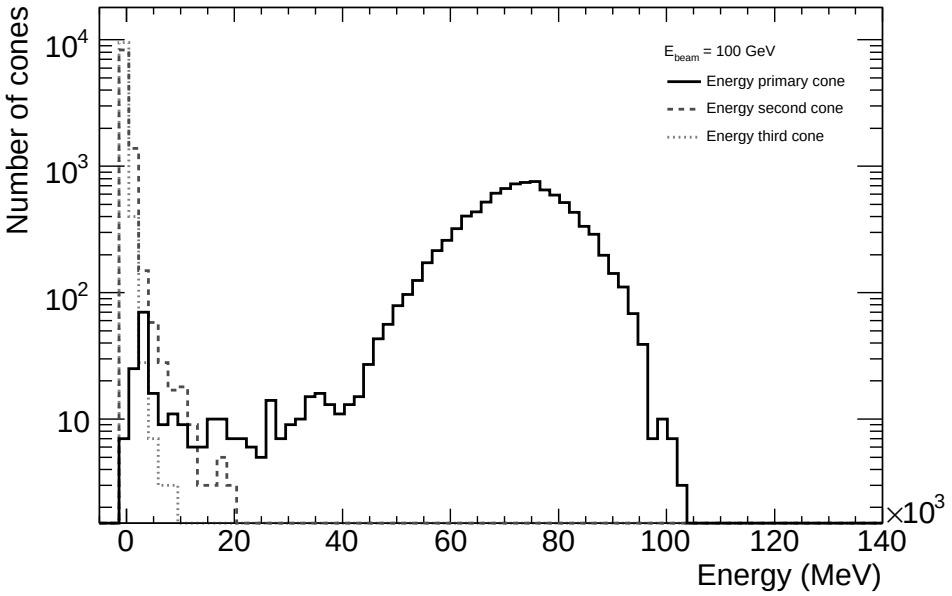

Figure 12: Cone energy distribution in a 100 GeV beam. The energy distributions of the first three cones are displayed.

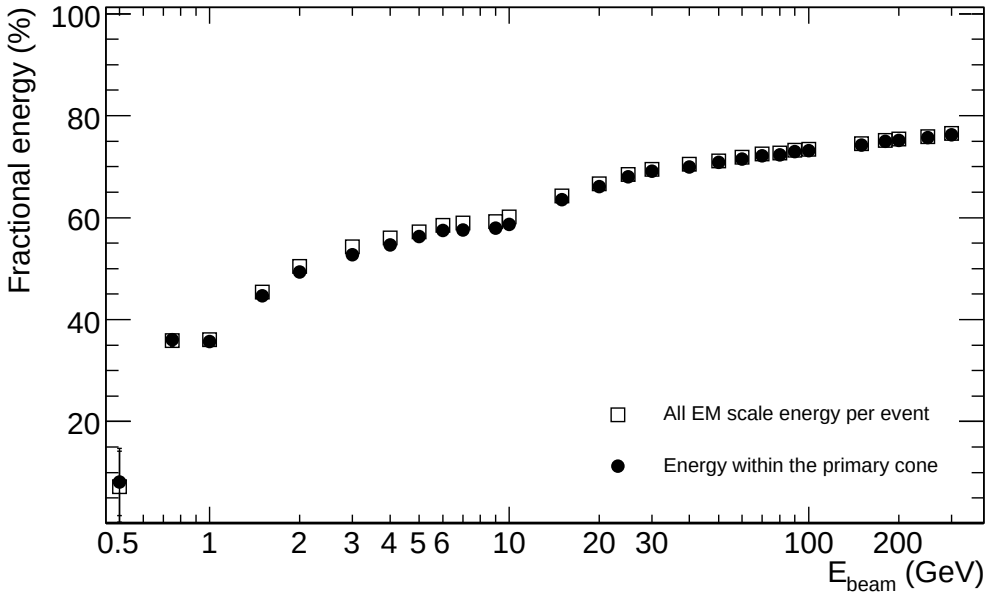

Figure 13: Fractional energy of the primary (most energetic) cone, E_{cone}/E_{beam}, as a function of beam energy. The fraction of all energy per event, as reconstructed on the electromagnetic scale, E_0/E_{beam}, is shown for comparison.

values. This gives a general lowering of the ratio $E^{truth}_{cell}/E^{0}_{cell}$. This happens even when the noise cuts are symmetric, since the cut is applied to the sum of noise and signal.

In this section, two ways of removing noisy cells will be considered: A cut on the energy density, and a restriction on the range of the energy ratios filled in the weight tables.

Whenever the energy signal is negative, we know for sure that it is dominated by noise. By looking at the negative part of an energy density distribution, we can get an estimation of the noise level. In Figures 14 and 15 the energy density distributions for a 10 GeV pion beam in the various LAr and Tile layers are given, together with the Gaussian fits to the negative part of the distributions. When looking at each sampling layer separately, the Gaussian correctly reproduces the shape of the distribution, but when considering the energy density distribution of all cells in all LAr layers or all Tile layers, the distributions are clearly not Gaussian. This indicates that the noise can be estimated from the energy density, if we consider each sampling layer separately. The noise estimations found this way are in agreement with other methods for handling the noise, see Section 4.3.

In Figures 16-17, the estimated energy density noise level for the various sampling layers of LAr and Tile are given for a selection of beam energies. The noise levels are independent of beam energy to the first order, as demonstrated in the figures.

For the remainder of the note, unless something else is explicitly stated, only cells that fulfil $|\rho_E| > \rho_{E,noise}$ have been weighted. The energy density noise estimates are given in Table 1.

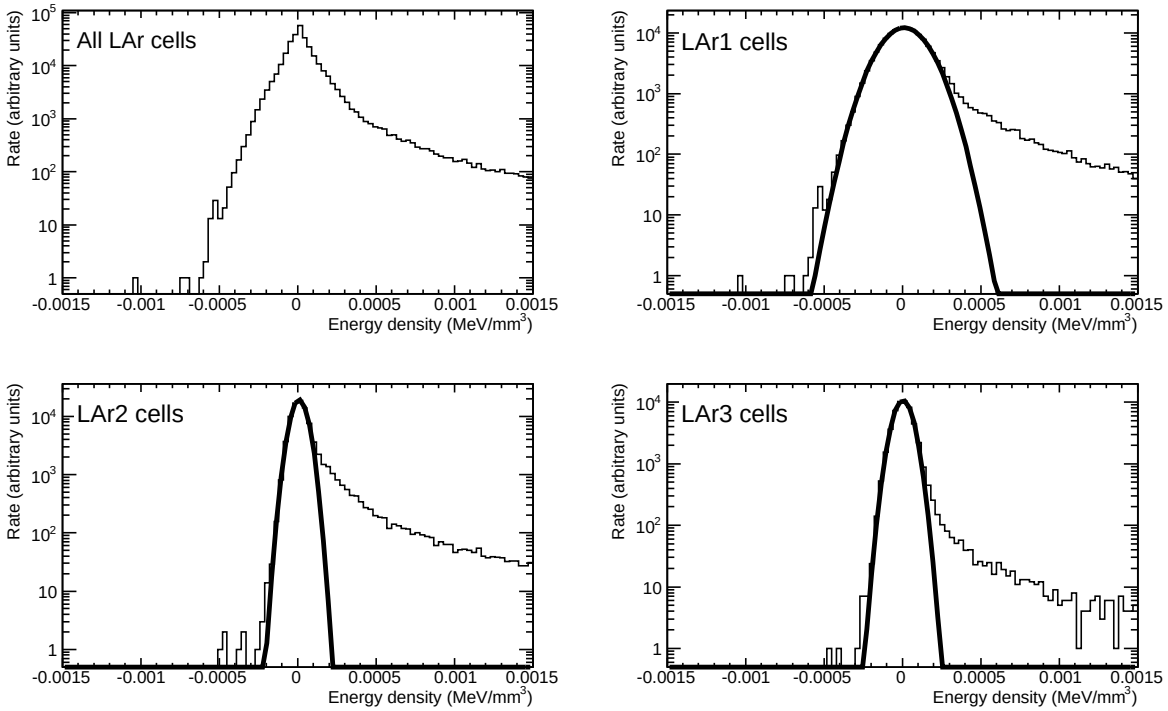

Figure 14: Cell energy density in LAr cells, expanded around 0 and fitted with Gaussians. The beam energy is 10 GeV. The Gaussians have been fitted to the negative part of the histogram and plotted for the full range. The top left plot shows the energy density in all LAr cells, and the other plots show the cell energy density for the various sampling layers. It should be noted that the pre-sampler (LAr0) has cell volume 0 in the simulation, so no energy densities can be computed.

Sampling layer	$\rho_{E,noise}$ (MeV/mm^3)
LAr1	$(3.9495 \pm 0.0034) \cdot 10^{-4}$
LAr2	$(1.4244 \pm 0.0015) \cdot 10^{-4}$
LAr3	$(1.6490 \pm 0.0021) \cdot 10^{-4}$
Tile A-cells	$(4.1623 \pm 0.0013) \cdot 10^{-6}$
Tile BC-cells	$(1.0483 \pm 0.0023) \cdot 10^{-6}$
Tile D-cells	$(5.7918 \pm 0.0017) \cdot 10^{-6}$

Table 1: Energy density noise estimates. The values and the uncertainties are given by the Gaussian fits to the energy density distributions.

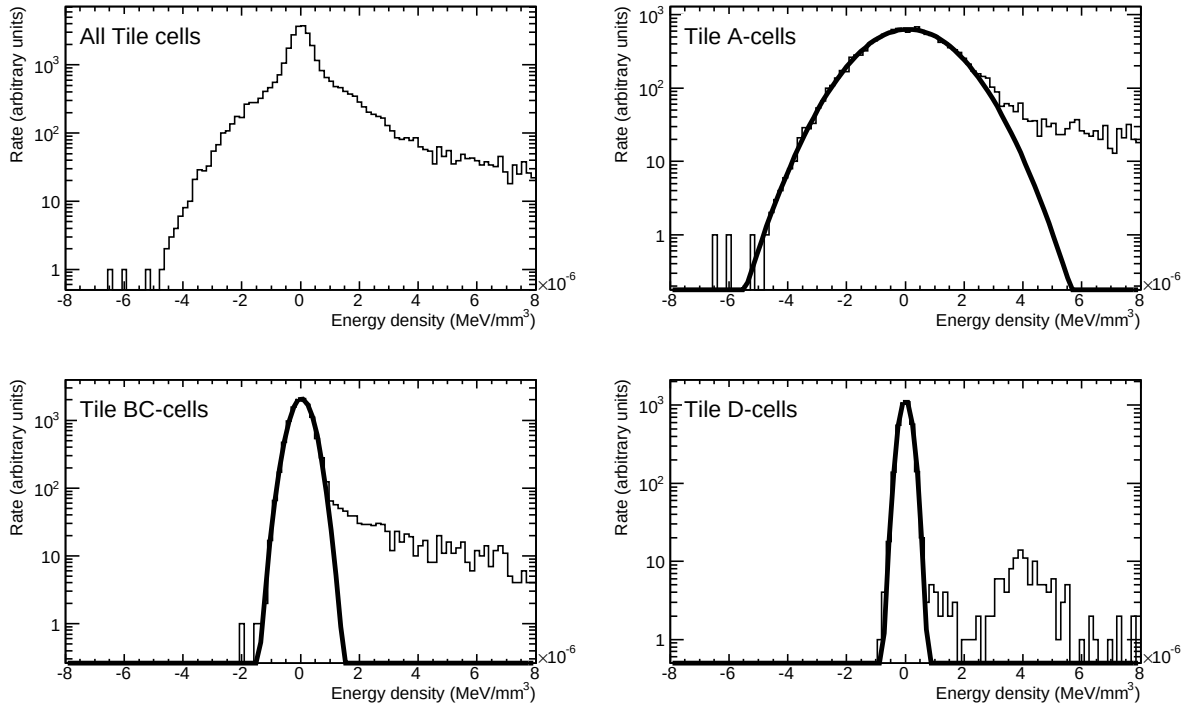

Figure 15: Cell energy density in Tile cells, expanded around 0 and fitted with Gaussians. The beam energy is 10 GeV. The Gaussians have been fitted to the negative part of the histogram and plotted for the full range. The top left plot shows the energy density in all Tile cells, and the other plots show the cell energy density for the various sampling layers.

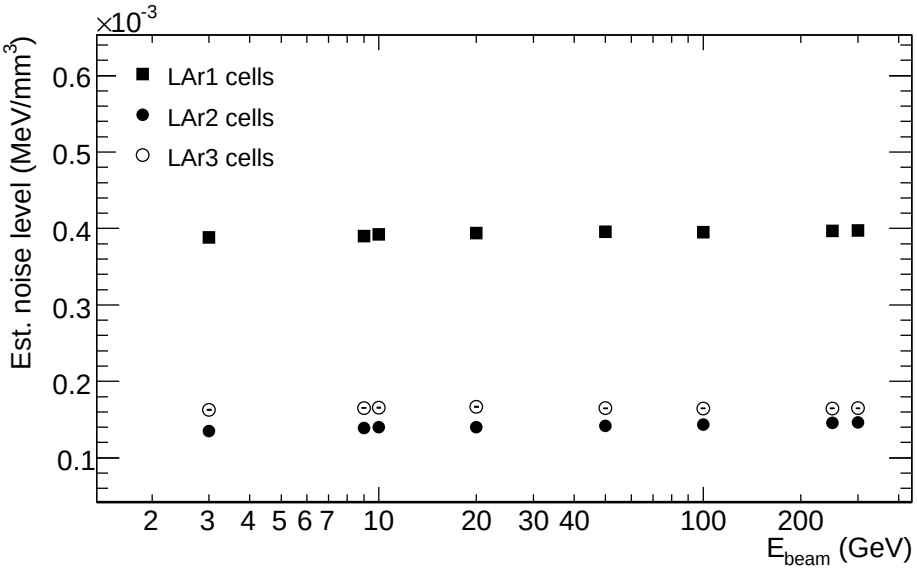

Figure 16: Estimate of the cell noise level in the various LAr layers, for a selection of beam energies. The estimated noise level has been computed from $3 \cdot \sigma$ of a Gaussian fit to the negative part of the energy density distribution (compare Figure 14).

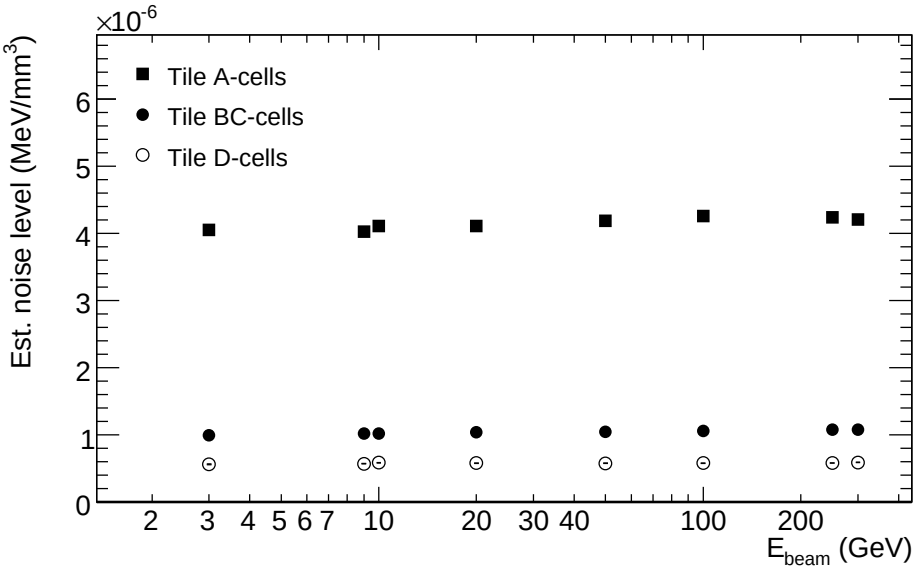

Figure 17: Estimate of the cell noise level in the various Tile layers, for a selection of beam energies. The estimated noise level has been computed from $3 \cdot \sigma$ of a Gaussian fit to the negative part of the energy density distribution.

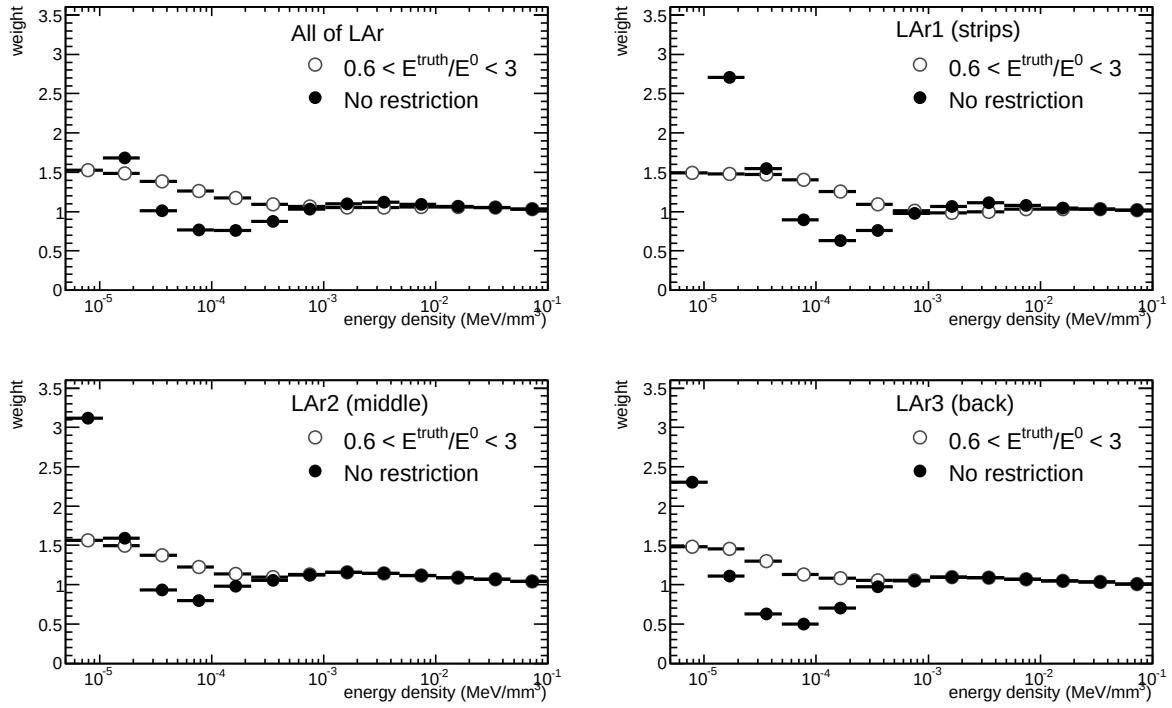

Figure 18: Weights for the LAr cells as a function of energy density, with and without the energy ratio restriction cut, $0.6 < E^{truth}_{cell}/E^{0}_{cell} < 3$. The weights have been averaged over all cone energies. The top left plot show the mean weights in all LAr cells, and the other show the weights in the various sampling layers. The approximate energy density noise level in LAr is $2 \cdot 10^{-4}$ MeV/mm^3 (see Table 1 for more precise values).

Another way to reduce noise when making the weight is to implement a restriction on the energy ratios filled in the weight tables. As described earlier, the noise cuts in the topo cluster formation will give a weight that is too low. When correcting for invisible hadronic energy, there is in theory never need for a weight lower than 1. However, just cutting out all energy ratios below 1 would give a bias towards higher weights, due to the Gaussian smearing of the reconstructed E^{0}_{cell} values. For the computation of the weights in the test beam environment in this note, we have applied the restriction $0.6 < E^{truth}_{cell}/E^{0}_{cell} < 3$ on the energy ratios filled in the weight tables [22]. The lower limit is intended to remove the low-weight bias from noise, as described above. The upper limit removes weights from cells with a very low reconstructed signal compared to the true energy deposition [23]. The effects of the weight restriction in the LAr and Tile calorimeters are shown in Figures 18 and 19.

In both the calorimeters, the energy ratio restriction cut clearly has the greatest impact about and below the energy density noise cut, which is approximately $2 \cdot 10^{-4}$ MeV/mm^3 for LAr cells and 10^{-6} MeV/mm^3 for Tile cells, (see Table 1), while the cut has very little effect on weights for cells with high energy density. After the weight restriction cut, the weights in LAr show the expected behaviour: at low energy densities, the weight are high, but they shrink as the energy density increases, stabilising at 1 for high densities. In Tile, the weights without the restriction cut are very high at low energy densities, and after the restriction, the weights show an overall

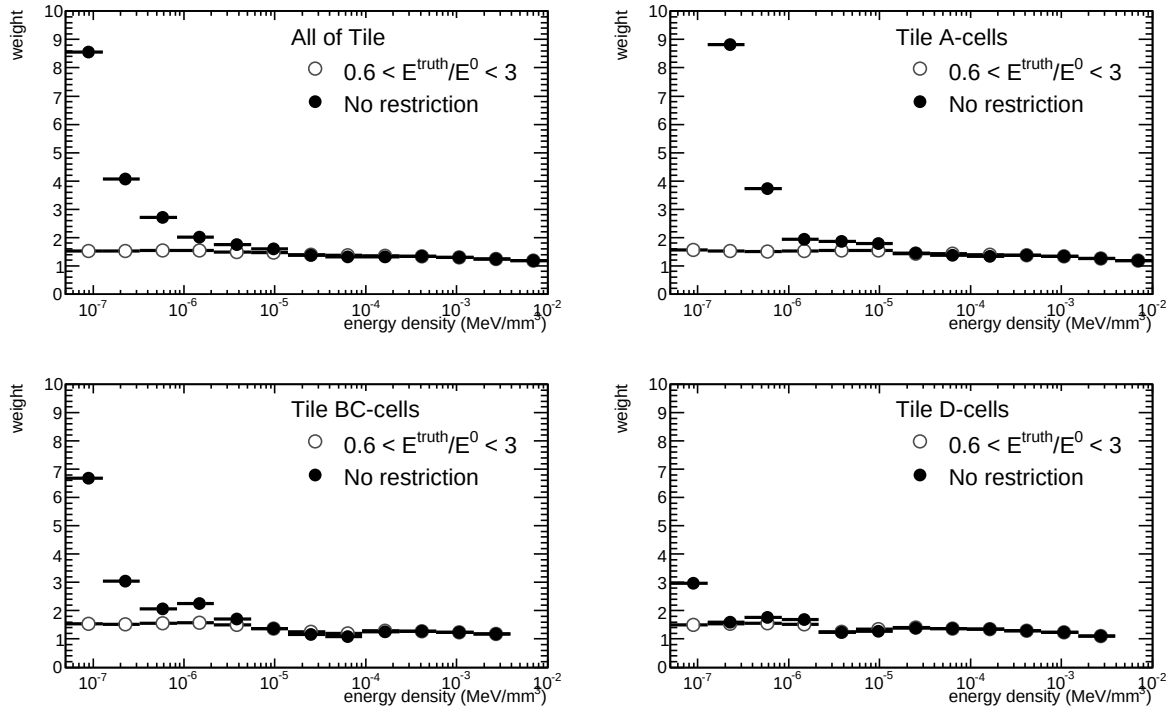

Figure 19: Weights for the Tile cells as a function of energy density, with and without the energy ratio restriction cut, $0.6 < E^{truth}_{cell}/E^{0}_{cell} < 3$. The weights have been averaged over all cone energies. The top left plot show the mean weights in all Tile cells, and the other show the weights in the various sampling layers. The approximate energy density noise level in Tile is 10^{-6} MeV/mm^3 (see Table 1 for more precise values).

decreasing behaviour as the energy density increases, from $w_{cell} \approx 1.5$ at the very lowest energy densities, to $w_{cell} \approx 1.2$ at the highest energy densities.

Figures 21-22 in Section 3.6, show the effects of the combination of the energy density and weight restriction cuts on the linearity and resolution of weighted energy. A restriction on the energy ratios filled in the weight tables is necessary to eliminate noise effects, that are not removed by the noise cut on the energy density, such as the general lowering of the weight values when the signal is close to the noise cut. As demonstrated in Figure 21, especially the linearity is sensitive to the noise bias in the weights, and the noise cut on energy density alone is not enough to reduce the noise-induced lowering of the weights. However, there are problems in implementing a restriction on the energy ratios themselves, since a cut on the ratio is a cut on simulation level, which is irreproducible on reconstruction level, where we do not have access to the true value of the deposited energy.

The systematic effects from the choice of restriction limits on the performance of the weights have not been studied. Lowering any of the weight limits will lead to a lowering of the weights, and raising any of the limits will lead to a similar raise in the weights. In that sense, the cut values are chosen somewhat arbitrarily, and for the local calibration weight tables implemented in ATHENA, the values are slightly different (see Section 6). The currently used schemes for

local hadronic calibration employ a restriction on the weights themselves, but for future applications, it is necessary to investigate other cuts for reducing noise-induced weight biases, based on variables accessible at the reconstruction level, since weight restriction might lead to a bias in the hadronic scale energy.

3.5 The weights

The weights are computed from simulated single pions in the combined test beam set-up, using $10,000$ events from each of the 53 different logarithmically equidistant beam energies in the range $0.5 - 316.23$ GeV, as described in Section 2.4. The variables mentioned above, the cell energy density and the energy cone, are used to parametrise the weights. The weights are computed as

$$w_{cell} = \langle E_{cell}^{truth} / E_{cell}^{0} \rangle \tag{3}$$

where E_{cell}^{truth} is the true energy of the cell as given in the simulation, and E_{cell}^{0} is the cell energy reconstructed on the electromagnetic scale, i.e. the data-like uncalibrated energy. The weights are filled into two-dimensional tables, according to cell energy density and the energy of the cone in which the cell falls. One weight table for each sampling layer of the calorimeters is made, giving 3 weight tables for the LAr calorimeter and 3 for the Tile calorimeter. The LAr pre-sampler cells cannot be calibrated using the method described here, because the passive material belonging to the pre-sampler cells (essentially the inner detector and the dead material in front of the pre-sampler) is heterogeneous and cannot be characterised by a single volume value. The pre-sampler energy is by default calibrated for electrons, and must be re-calibrated to the different properties of pions [24]. This is done together with the dead material corrections, see Section 4.4.

All beam energies are used to fill each weight table, making the weights as unbiased by the initial beam energy as possible. When applying the weights, the only information used to extract the corresponding weight for a cell in a given sampling layer is the energy of the cone in which the cell falls and the energy density of the cell.

Weights are computed from all cells in all topo clusters of the most energetic cone of each event. When filling the weight tables, only ratios that fulfill $0.6 < E_{cell}^{truth} / E_{cell}^{0} < 3$ are entered into the tables. The weight used is the mean value of the weights filled into the bin in question[5)]. When applying the weights, all cells within any topo cluster that have energy density above the estimated noise level, as given in Table 1, are weighted.

The numerical values of the weights can be found in Appendix A. In the next section, the performance of the weights when applied to an independent Monte Carlo sample is shown.

[5)] The technical solution we have used is to fill the weights from each cell into the ROOT histogram type `TProfile2D`, where the averaging over each bin is done automatically [25].

3.6 Linearity and resolution of weighted energy

In order to study the performance of the weights, they have been applied to the energy of independently simulated pions at different energies in the range 0.5 - 300 GeV. In Figure 20, the energy distributions of the unweighted topo cluster energy on the electromagnetic scale is compared with the energy after weighting and the simulation truth energy.

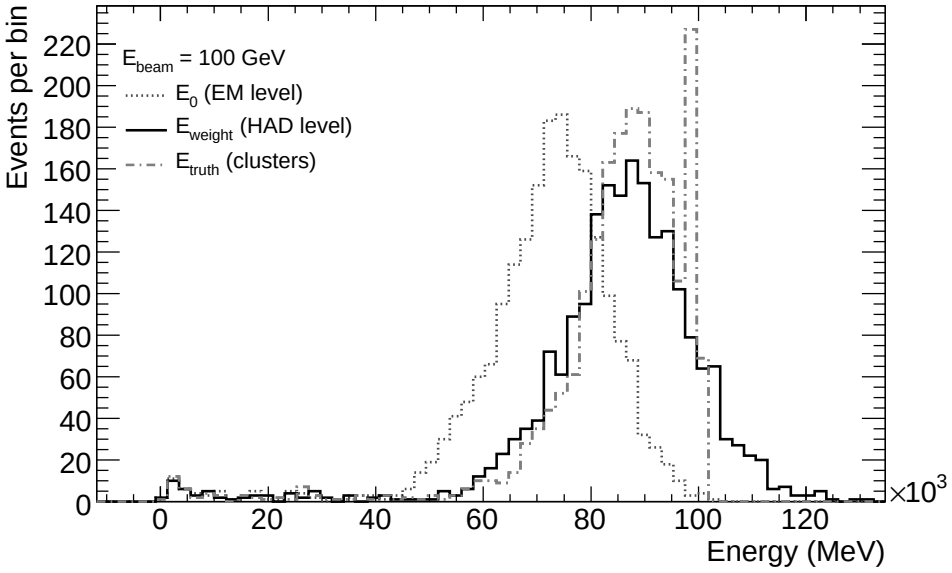

Figure 20: Unweighted (E_0), weighted ($E_{weighted}$) and Monte Carlo truth energy (E_{truth}) distributions for a 100 GeV pion beam. All energies considered are the energies within topo clusters.

Two things should be noted in Figure 20: the Monte Carlo truth energy does not peak (solely) at the beam energy, and the distribution is not Gaussian. Both these observations can be explained with losses in "dead" material (see also Section 4.4). Some of the pions start to shower in LAr, and lose part of their energy in the cryostat between LAr and Tile. These events form the broad peak at 90 GeV. Some pions do not shower until they reach Tile, where they lose the majority of their energy. These events form the narrow peak at the beam energy. The width of the 90 GeV peak of the E_{truth} distribution is an effect of the energy losses in the cryostat.

Ideally, the weighting procedure will reproduce the Monte Carlo truth distribution, which means that we do not expect the distribution of the weighted energy to be Gaussian.

When comparing results of weighting schemes, normally a Gaussian is fitted to the energy distribution, and the quantities E_{mean}/E_{beam} as a function of the energy (the *linearity*) and σ/E_{mean} (the *resolution*) are computed. However, when the weighted energy distribution is not expected to be Gaussian, these quantities do not make sense. Instead we are interested in the weighted energy in relation to the Monte Carlo truth, rather than the beam energy. The ratio

$$\frac{E}{E_{truth}}, \tag{4}$$

where E is the weighted or unweighted energy and E_{truth} is the Monte Carlo truth energy deposited within the topo clusters can be used to measure the performance of the weighting. The distribution of this ratio is expected to be Gaussian with a mean value close to 1, and parameters of a Gaussian fit[6)] can be used to estimate the resolution as

$$r = \frac{\sigma}{mean}. \tag{5}$$

The linearity is taken to be $mean - 1$ of the E/E_{truth} distribution.

In Figure 21, the linearity of the energy on the electromagnetic scale is shown, as well as the linearity of the weighted energy, with and without noise restriction on the energy ratios filled into the weight tables, as described in the previous section.

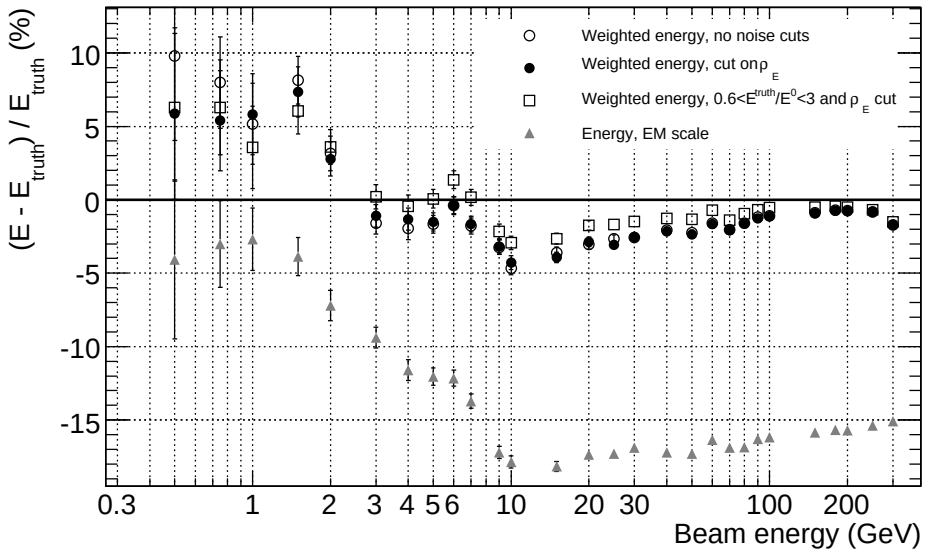

Figure 21: Linearity of weighted and unweighted energy, from Monte Carlo simulations. Comparison between the unweighted energy on the electromagnetic scale, (grey triangles), energy which has been weighted with weight tables with energy density noise cuts (filled circles), weight tables with energy density noise cuts and ratio restriction (squares) and without noise reduction (open circles). All errors are statistical errors from the Gaussian fits.

As shown in Figure 21, the weighting improves the linearity for all energies above 2 GeV. If the weight tables that are filled with the restriction $0.6 < E_{cell}^{truth}/E_{cell}^{0} < 3$ are used in combination with the energy density cut, which gives the best performance, the linearity is within 3% of the expected value for all energies above 2.5 GeV.

The unexpected rise in linearity at beam energies lower than 10 GeV is an effect of the noise in the calorimeters, which is discussed further in Section 5.5. The drop in linearity for the weighted energy at the highest beam energies is discussed in Section 5.4.

[6)] In order to make the fit as stable and independent of non-Gaussian tails as possible, the fit is first made to the full distribution, and then redone in the region $mean \pm 2\sigma$. Unless something else is explicitly stated, this is how all Gaussian fits throughout this note are made.

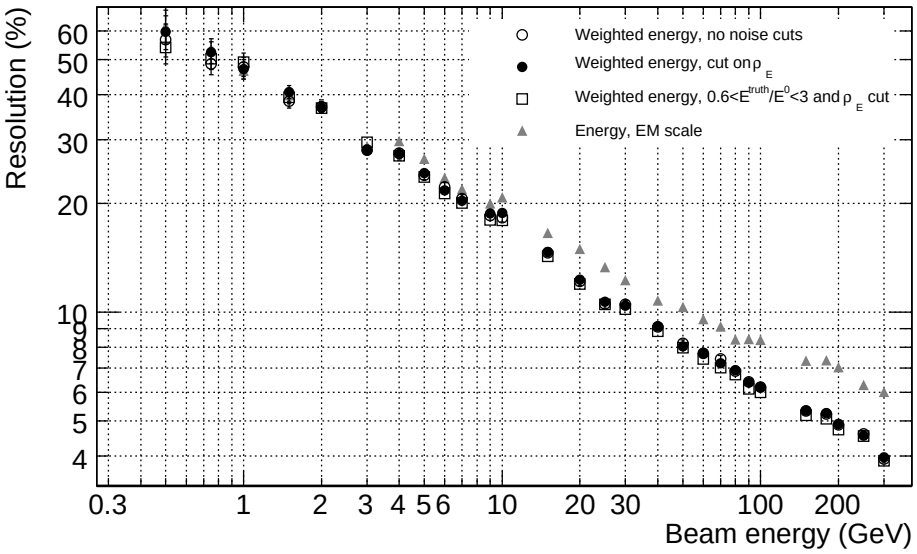

Figure 22: Resolution of weighted and unweighted energy from Monte Carlo as a function of beam energy. Comparison between the unweighted energy on the electromagnetic scale, (grey triangles), energy which has been weighted with weight tables with energy density noise cuts (filled circles), weight tables with energy density noise cuts and ratio restriction (squares) and without noise reduction (open circles). All errors are statistical errors from the Gaussian fits.

In Figure 22, the resolution, as defined in Equation 5, of the weighted and unweighted energy is shown as a function of beam energy, and in Figure 23 the difference of resolutions, $r_0 - r_{weight}$ is given.

As shown in Figures 22 - 23, the weighting procedure improves the resolution of the energy, compared to the unweighted electromagnetic scale energy, for all beam energies above 3 GeV. The impact of the noise cuts is not as visible in the resolution as in the linearity, but it seems like the combination of energy density cuts and weight restriction gives a systematically slightly better resolution, although the fluctuations are within the statistical errors for most beam energies.

It should be noted that although the beam energies 1.5, 3, 15, 150 and 300 GeV were not used to fill the weight tables, the properties of the weighted energy from these beam energies are as expected from the behaviour of the neighbouring beam energies.

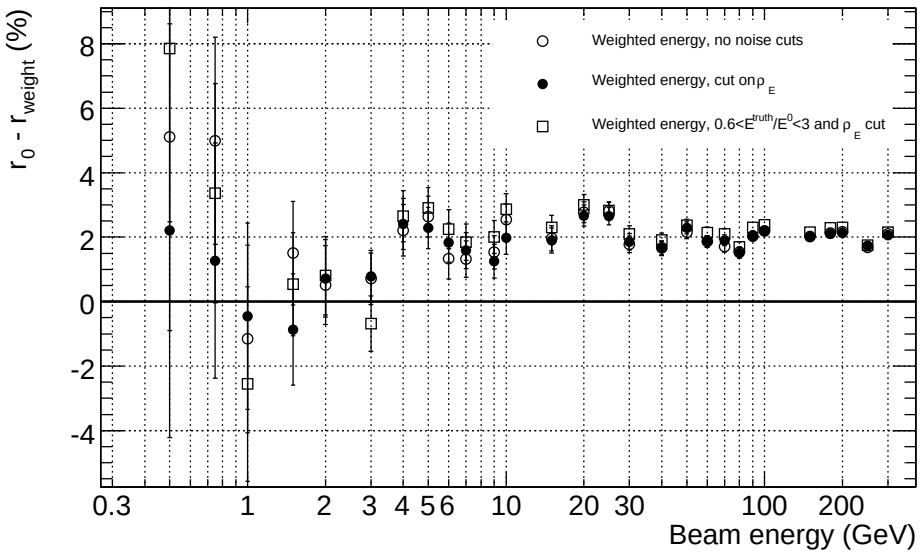

Figure 23: Difference of resolutions, $r_0 - r_{weighted}$ as a function of beam energy. A positive value in this plot means that the weighting procedure improved the resolution. Comparison between the unweighted energy on the electromagnetic scale, (grey triangles), energy which has been weighted with weight tables with energy density noise cuts (filled circles), weight tables with energy density noise cuts and ratio restriction (squares) and without noise reduction (open circles). All errors are statistical errors from the Gaussian fits.

4 Application on data from the combined testbeam of 2004

In the previous section, the performance of the weighting factors on an independent Monte Carlo sample was studied. However, the performance of the weights on real data is of greater interest. For studies of the weighting scheme, seven runs of real data from the combined test beam of 2004 have been used. In this section, the conditions of the data runs are described, as well as the cuts needed to get a pure pion sample. A comparison between data and simulation of certain variables is shown, and finally the weights are applied to the real data.

4.1 Runs used

Of the seven real data runs used, two are high-energetic negative pion runs, 2101257 and 2101335 (beam energies 180 and 250 GeV), three are positive pion runs, 2102347, 2102355 and 2102396 (beam energies 50, 100 and 20 GeV), one is a positron run at 180 GeV, run 2102182, and one is a low-energetic negative run at 9 GeV, run 2102095. This latter run is nominally an "electron" run, but for very low energies, the particles in the beam are always a mixture of pions, muons and electrons. The 180 GeV e^+ run is only used for comparing the cuts and is not included in the linearity or resolution plots shown in Section 4.5.

In all beams, regardless of label, a contamination of muons, electrons and pions is present. See Table 2 for a list of the runs used [26].

run	*type*	E (GeV)	E_{true} (GeV)	η
2101257	π^-	180	180.92 ± 0.52	0.450
2101335	π^-	250	251.22 ± 0.51	0.440
2102095	e^-	9	9.009 ± 0.090	0.45
2102182	e^+	180	179.68 ± 0.52	0.45
2102347	π^+	50	–	0.45
2102355	π^+	100	100.45 ± 0.56	0.45
2102396	π^+	20	–	0.45

Table 2: A list of the data runs used in the analysis [26]. E_{true} refers to the real energy of the particles in the beam, determined from the currents of the selection magnets. From each of the runs, $10,000$ events have been reconstructed.

The run energies given in the logbook are not the exact energies of the particles on impact, only an approximation. A more accurate value can be obtained using information from the currents of the selection magnets [27, 28]. For some reconstructions, the true beam energy, as computed from the selection magnets, is given in the reconstructed data files [7)] .

From each of the seven runs, $10,000$ events have been reconstructed using ATHENA11.0.41.

[7)] For example, the official reconstruction with version 12.0.5 contains a variable "Energy", which is the true beam energy [24]. The files can be found at
`/castor/cern.ch/grid/atlas/datafiles/ctb/realdata/12.0.5.v2/`.

4.2 Cuts on data

The particle types listed in Table 2 only give an indication of which particle was most abundant in the beam, since the conditions of beam production always give a contamination of pions, electrons and muons. The contamination rate varies greatly from run to run, from a few percent to more than half the events. For the positive pion beams, we also have a contamination of protons, which consist about half the particles in the beam [29]. The weights were developed from and tested on pion beams, so we want the real data runs to be purely pions as far as possible. To achieve this, we have implemented certain cuts on data, which are summarised in Table 3. In that table, the number of events surviving the various cuts is also given. The cuts follow the standard procedure for cleaning data [24], with the exception of the electron cut and the "energy OK" cut. The protons, however, cannot be removed with any cut. The effect of the proton contamination will be discussed later in this section.

E_{beam} (GeV)	Trigger= 1	Energy OK	sADC_S1	$N_{cluster} > 0$	No μ	No e	Clock	All cuts
250	9620	9798	8885	9962	9907	9850	7307	6119
180	9177	9610	8847	9816	4420	9357	7330	2418
100	9304	9709	9028	9898	8430	9649	10000	7187
50	9263	9684	9050	9869	9409	9619	10000	8048
20	9718	10000	9502	9856	9632	6158	10000	5406
9	9628	9944	9238	9732	9998	5837	10000	5271
180, electrons	9595	9903	9143	9918	6103	7985	10000	3810

Cut	Code	Meaning of cut
Trigger	Trigger= 1	only physics events chosen
"Energy OK"	$\lvert E^0_{event}\rvert < E_{beam} + 100$ GeV	Remove abnormally high energies
sADC_S1	$150 <$ sADC_S1 < 1400	Beam line scintillator cut
$N_{cluster}$	$N_{cluster} > 0$	At least one cluster formed in the event (noise reduction)
No μ	sADC_muTag< 450	removes muons by cutting on muon scintillator signal
No e	$E_{Tile} > 0.01 \cdot E_{beam}$	removes electrons by requiring a signal in Tile
Clock	Clock > 18 ns	Compensate for timing problem (180 and 250 π^- runs only)

Table 3: Cuts on data, and the number of events surviving the various cuts. The top table shows the number of events surviving the various cuts. For all runs, 10000 events were reconstructed. The rightmost column gives the number of events passing all the cuts. It should be noted that some cuts are overlapping, and that the Clock cut was only applied to the high-energetic π^- runs, 180 and 250 GeV. The bottom table gives a summary of the cuts used and their meanings, which are elaborated in the text.

The number of events out of the original $10,000$ surviving the cuts varies greatly, from more than 8000 events for the 50 GeV π^+ run to only about 2400 for the 180 GeV π^- run.

For a few of the events, the energy is abnormally high in Tile, giving a total reconstructed energy of about 400 GeV. This is most likely caused by a mis-reconstruction in Tile [30]. Since these energies are clearly wrong, the events are removed with the $|E_0| < E_{beam} + 100$ GeV cut. After this cut, a very small tail between 250 and 350 GeV remains in the 250 GeV run. The origin of these few high-energy events is unknown. However, since the tail only contains one

event in a thousand, the effect is negligible.

The sADC_S1 cut is a cut on a beam-line scintillator, placed upstream of the ATLAS detector parts in the test beam set-up [18, 24]. The $N_{cluster} > 0$ cut requires that at least one topo cluster was formed per event used. This cut is a built-in feature of how we define our signal: only energy depositions within topo clusters are considered as signal. Muons are removed from the runs with a cut on the sADC_muTag scintillator, which is placed downstream of the muon chambers, behind the beam dump [18]. The Clock cut was only applied to the high-energetic π^- runs, 180 and 250 GeV, due to timing problems in these runs [20, 26]. The cut Trigger=1 picks out the "physics" events, which means that events with at least one particle in the beam line were chosen.

The most significant cut for the low-energetic runs and the electron run is the electron removal cut. In Figure 24, the effect of the muon cut when applied to the 100 GeV positive pion

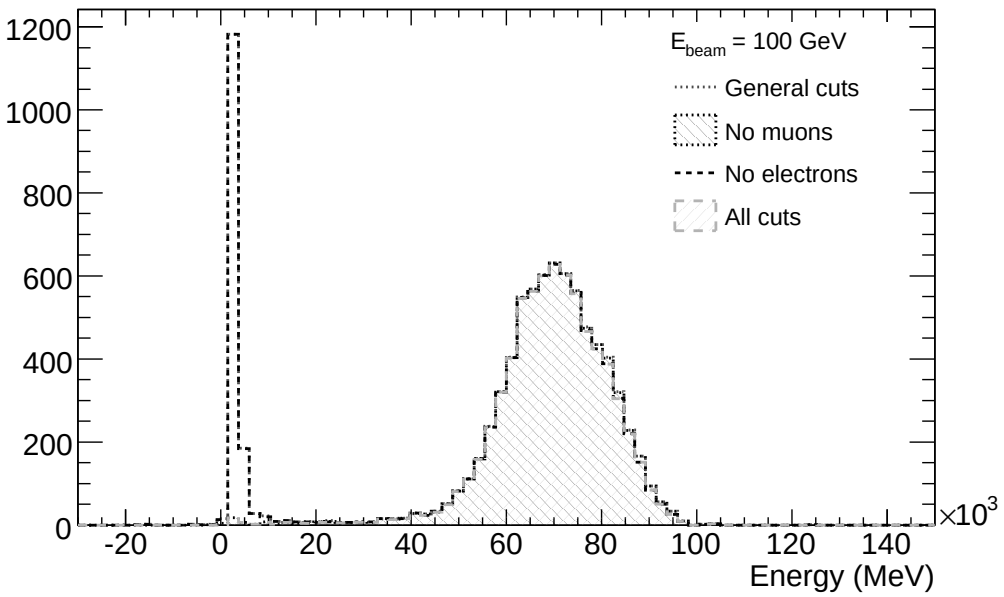

Figure 24: Effect of the cuts on the positive 100 GeV pion beam. "General cuts" summarises the "energy OK" cut, the $N_{cluster} > 0$ cut, the Trigger cut and the sADC_S1 cut. The effect of the muon and electron cuts is shown. Especially the significance of the muon cut is visible in this run, since the muon peak at ≈ 2 GeV almost completely vanishes with that cut. The electron cut can be seen as a small decrease of the distribution at the highest energies.

beam is clearly visible, since the muon peak at ≈ 2 GeV almost completely vanishes after that cut. The effects of the electron cut on a positron beam at 180 GeV are shown in Figure 25, where the positron peak at beam energy is much affected by the cut.

The standard procedure for removing electrons is to look at information from the inner detector. However, for some of the runs used, the inner detector read-out was unstable, making cuts on inner detector variables impossible. Since it is important to treat all runs as equally as

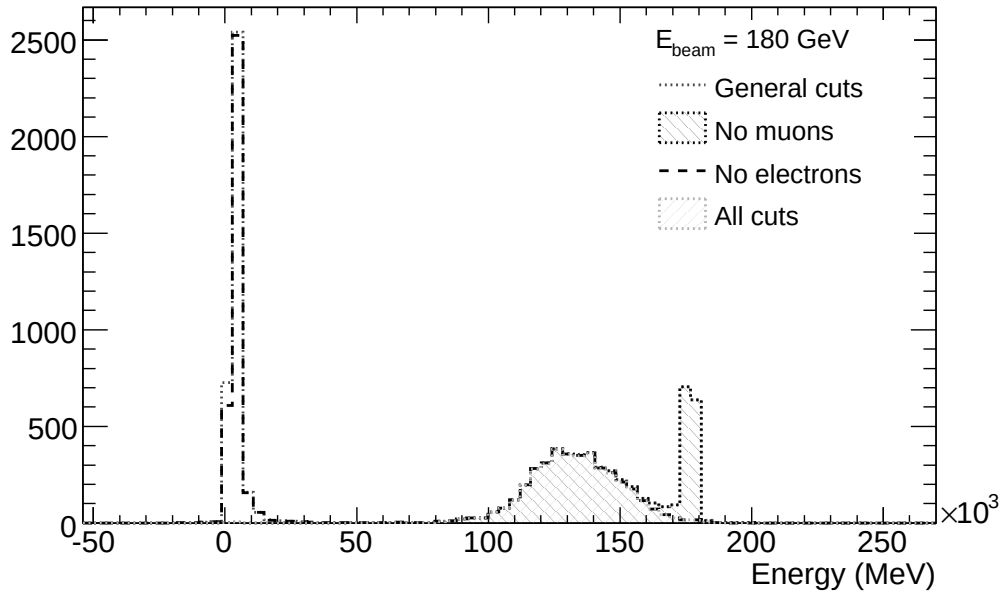

Figure 25: Effect of the cuts on the 180 GeV positron beam. "General cuts" summarises the "energy OK" cut, the $N_{cluster} > 0$ cut, the `Trigger` cut and the `sADC_S1` cut. The effect of the muon and electron cuts is shown. Both cuts are significant for this run. The muon peak at 2 GeV almost completely vanishes with the muon cut. The positron peak at beam energy is much affected by the electron cut.

possible, the properties of electron showers have been used instead. By requiring that at least 1% of the beam energy is reconstructed in the Tile calorimeter, particles that are fully contained in LAr are discarded. This action removes the vast majority of the electrons.

However, the electron cut will affect the pions as well, especially at low energies, when not all pions necessarily reach the Tile calorimeter. In Figures 26-27, linearity and resolution of the simulated pions, with and without the electron cut have been plotted. As shown in these figures, the linearity and resolution are little affected by the electron cut for beam energies above ≈ 20 GeV. At very low beam energies, some odd effects can be observed: the linearity is much larger than expected, with a peak at 2 GeV. The resolution is improved in an unexpected way for beam energies below ≈ 5 GeV, most likely as a result of the increased linearity. This low-energy effect could be caused by the electron cut selecting events with unusually high energy in Tile, in an energy region where most pions are fully contained in LAr. However, the effects of the electron cut are only interesting for beam energies where we have data runs, which is 9 GeV and higher. The small effects from the electron cut will be considered as systematic uncertainties. Details of the computation of the systematic effects are given in Appendix B.

Whenever data and simulated distributions are compared, the electron cut have been applied to the simulated sample, as well as the $N_{cluster} > 0$ cut. The other cuts cannot be applied to the simulated samples, since the necessary scintillators and clocks were not simulated.

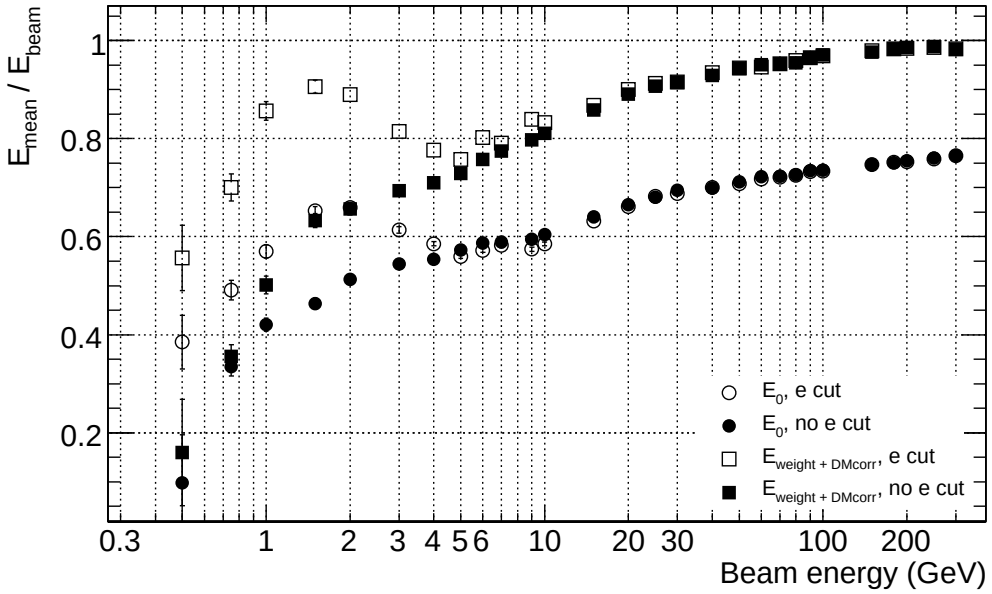

Figure 26: Effect of the electron cut on the linearity. Conclusions in text.

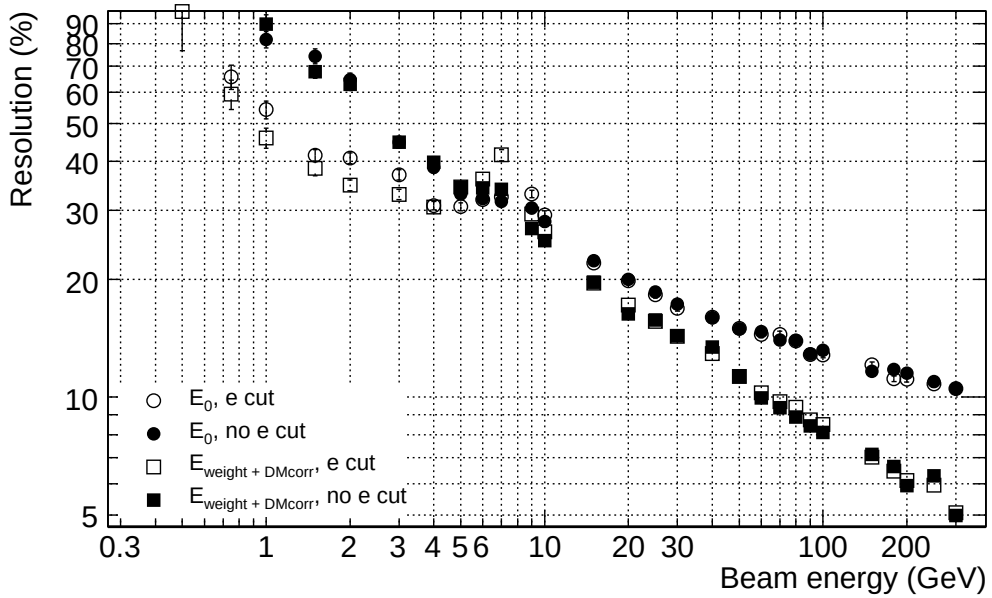

Figure 27: Effect of the electron cut on the resolution. Conclusions in text.

4.3 Comparison between data and Monte Carlo simulations

Simulated samples are used to compute the weights we use for hadronic weighting of the energy. Thus it is of great importance that the simulation correctly reproduces the data, since the results otherwise will contain errors inherited from the simulations.

In this section we take a closer look at the parameters of the weights, namely the cell energy density distributions (Figures 28 - 31) and the cone energy distributions (Figures 33 and 32). In addition, the shower development description is studied in Figures 34 and 35.

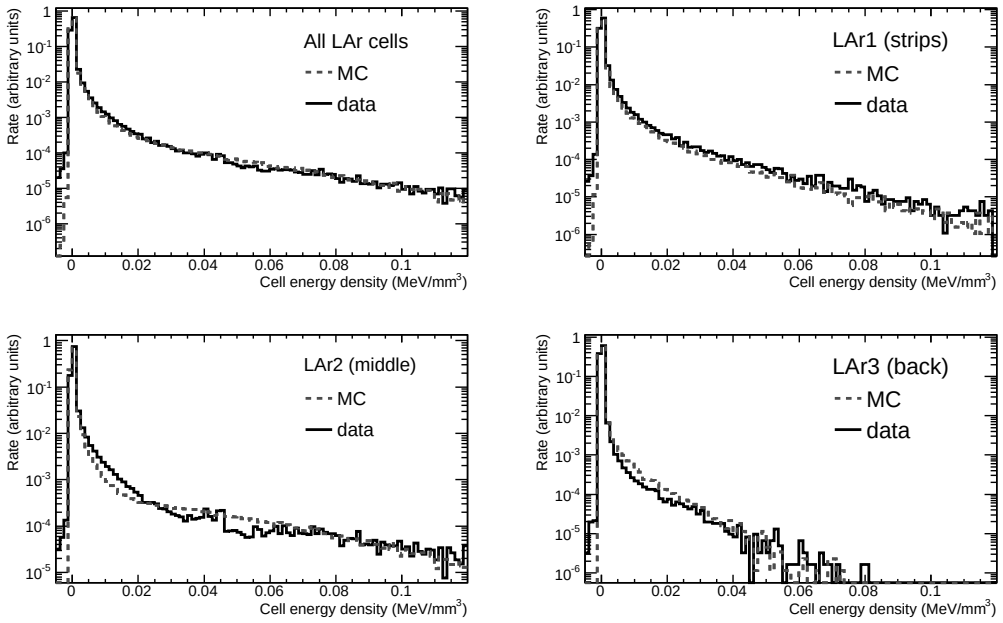

Figure 28: Cell energy density distribution in the various LAr sampling layers, for a 250 GeV beam. Comparison between data (negative pions) and a simulated pion sample (MC). The histograms have been normalised to 1.

In the distributions of the LAr cell energy densities, Figure 28, the data distributions have larger negative tails than the corresponding simulated distributions. This is an effect of non-Gaussian tails in the data distributions. If the negative part of the data distributions are fitted with Gaussians, as in Section 3.4, the values agree within 10% with those obtained from the simulated distributions, see Table 4.

The package `CaloNoiseTool`, available in ATHENA, can be used to extract the estimated noise for each cell. The expected energy density of the noise, as obtained from this package, is also given in Table 4. These values are of the same order as the estimations obtained using the energy density.

All positive data beams used contain a large proton contamination of as much as 50% [29]. Proton showers contain fewer neutral pions than a pion shower of the same nominal energy [17], due to conservation of the baryon number, which leads to a lower electromagnetic fraction in

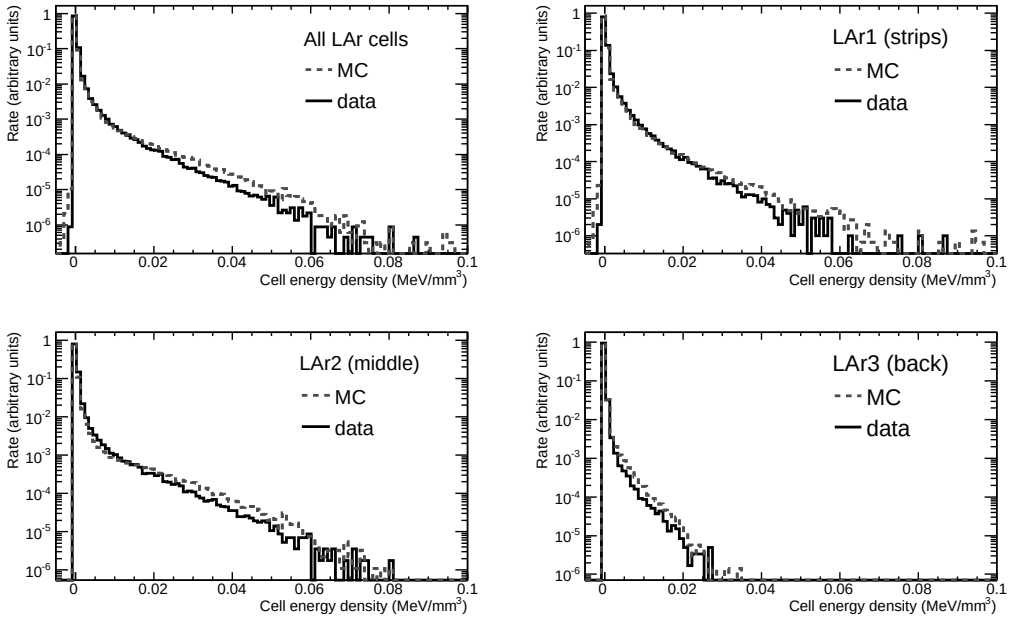

Figure 29: Cell energy density distribution in the various LAr sampling layers, for a 100 GeV beam. Comparison between data (positive pions) and a simulated pion sample (MC). The histograms have been normalised to 1.

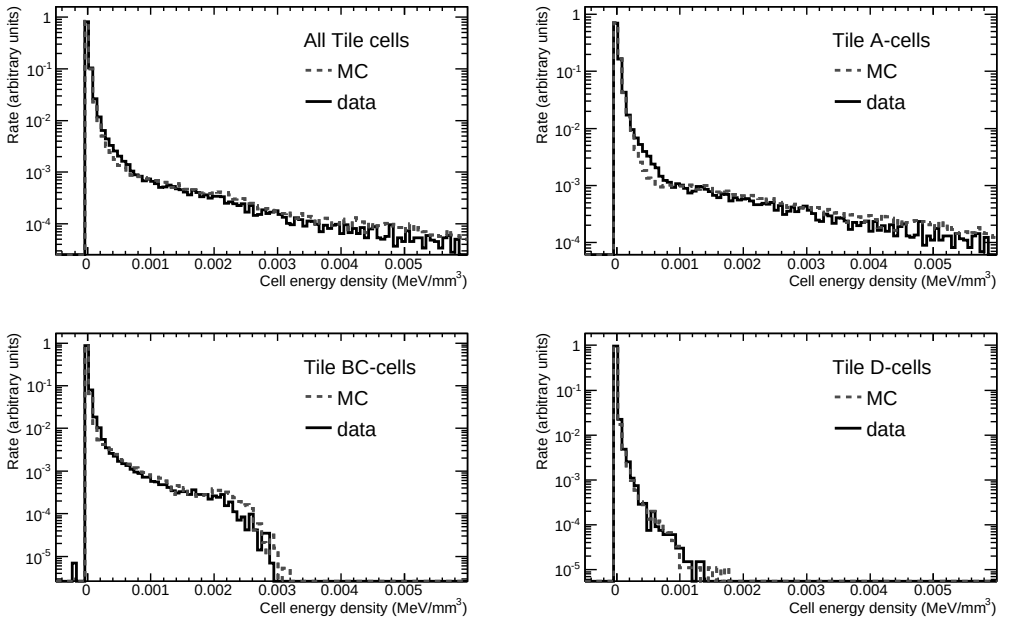

Figure 30: Cell energy density distribution in the various Tile sampling layers, for a 250 GeV beam. Comparison between data (negative pions) and a simulated pion sample (MC). The histograms have been normalised to 1.

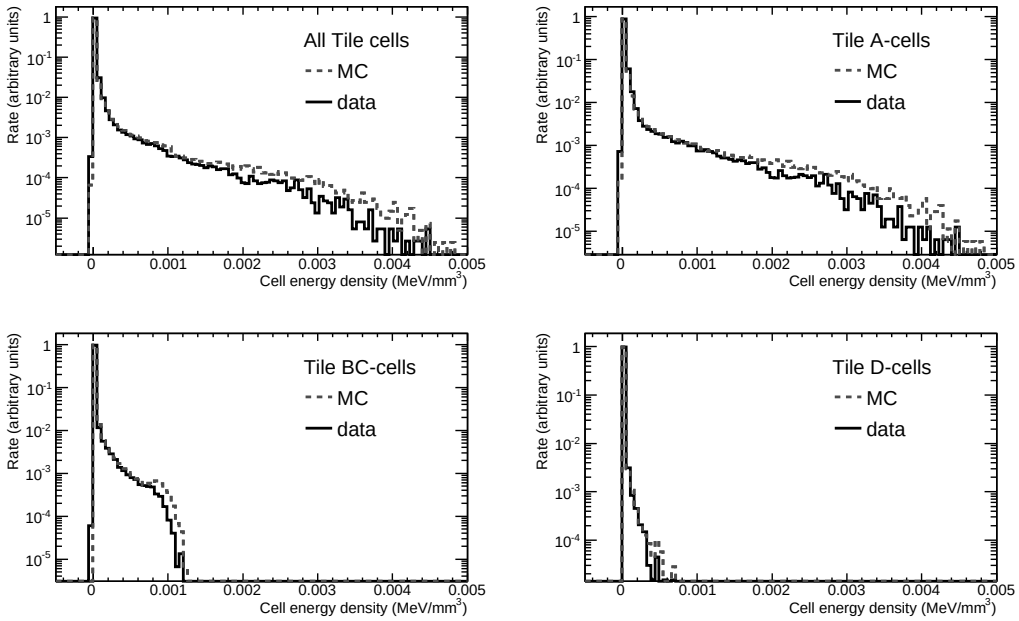

Figure 31: Cell energy density distribution in the various Tile sampling layers, for a 100 GeV beam. Comparison between data (positive pions) and a simulated pion sample (MC). The histograms have been normalised to 1.

	Data		***Simulation***
Sampling layer	`CaloNoiseTool` (MeV/mm^3)	$\rho_{E,noise}$ (MeV/mm^3)	$\rho_{E,noise}$ (MeV/mm^3)
LAr1	$(4.574 \pm 0.071) \cdot 10^{-4}$	$(4.0343 \pm 0.0021) \cdot 10^{-4}$	$(3.9495 \pm 0.0034) \cdot 10^{-4}$
LAr2	$(1.593 \pm 0.046) \cdot 10^{-4}$	$(1.4932 \pm 0.0011) \cdot 10^{-4}$	$(1.4244 \pm 0.0015) \cdot 10^{-4}$
LAr3	$(2.00 \pm 0.15) \cdot 10^{-4}$	$(1.6329 \pm 0.0010) \cdot 10^{-4}$	$(1.6490 \pm 0.0021) \cdot 10^{-4}$
Tile A-cells	$(4.01 \pm 0.13) \cdot 10^{-6}$	$(4.6112 \pm 0.0072) \cdot 10^{-6}$	$(4.1623 \pm 0.0013) \cdot 10^{-6}$
Tile BC-cells	$(9.8 \pm 1.3) \cdot 10^{-7}$	$(1.1431 \pm 0.0012) \cdot 10^{-6}$	$(1.0483 \pm 0.0023) \cdot 10^{-6}$
Tile D-cells	$(5.57 \pm 0.38) \cdot 10^{-7}$	$(6.1731 \pm 0.0082) \cdot 10^{-7}$	$(5.7918 \pm 0.0017) \cdot 10^{-6}$

Table 4: Energy density noise estimates for data and simulated samples. The values and the uncertainties of $\rho_{E,noise}$ are given by the Gaussian fits to the energy density distributions (compare with Table 1). The `CaloNoiseTool` values are the estimated noise energy density, obtained from the package `CaloNoiseTool`.

proton-induced showers than in pion showers and thus a lower reconstructed energy. The resolution of the energy in the pure proton beams is better, because the event-by-event fluctuations in the production of neutral pions is lower. Proton showers tend to be broader than pion-induced ones, while the latter generally reach deeper into the calorimeter [31], because of the higher total cross section of a proton-nucleus reaction than such a reaction involving a pion [32].

The effect of the proton contamination on the energy level is seen in the distribution of the cone energy of the positive 100 GeV beam (Figure 33), where the energy distribution from real data seems shifted towards lower values compared to the simulated energy distribution. In the energy density distributions for the positive beam (Figures 29 and 31), the proton contamination can be seen as a generally lower level of energy density in data than in the simulation. These effects are not seen in the energy density distributions of the negative 250 GeV beam (Figures 28 and 30), nor in the distribution of the 250 GeV π^- cone energy distribution in Figure 32.

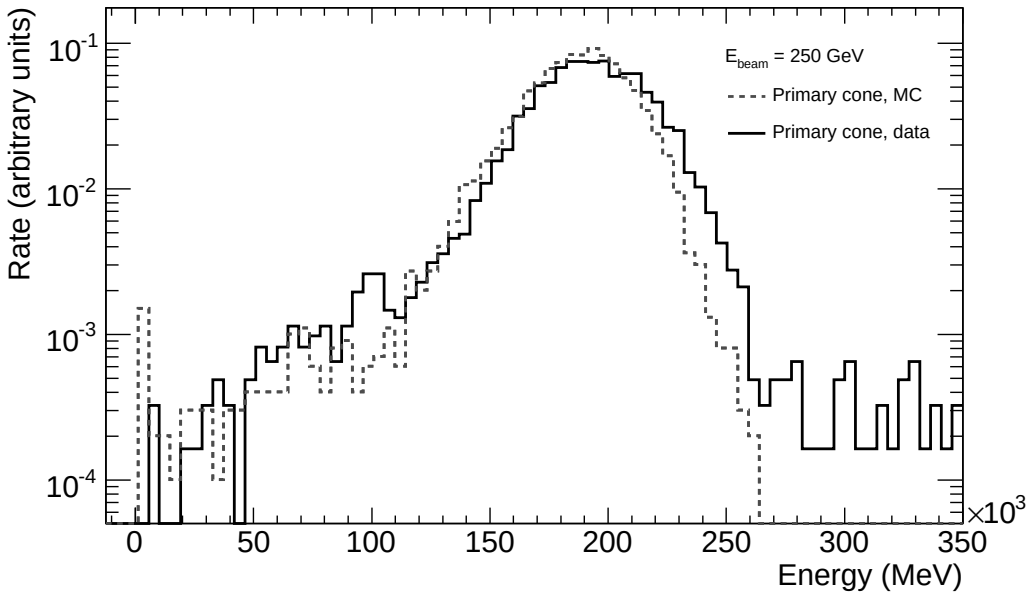

Figure 32: Cone energy distribution for a 250 GeV beam. Comparison between data (negative pions) and Monte Carlo simulation (MC).

The effects of proton contamination on the linearity are straight-forward: the lower response to the proton energy will lead to a general worsening of the linearity, at least for the electromagnetic scale energy. Since the weights have been developed for pions, and the physics of proton shower development is different to the development of a pion shower, the worsening in linearity might persist after weighting too, due to differences in the visible energy content and the longitudinal spread of the shower. The expected effects of the proton contamination on the resolution are difficult to predict, since the resolution of pure proton energy is better than the pion energy resolution. The energy distribution from the combination of pions and protons is two Gaussian distributions on top of each other, with slightly different mean values. Under such circumstances it is reasonable to expect a worsening in the resolution. Unfortunately, we have

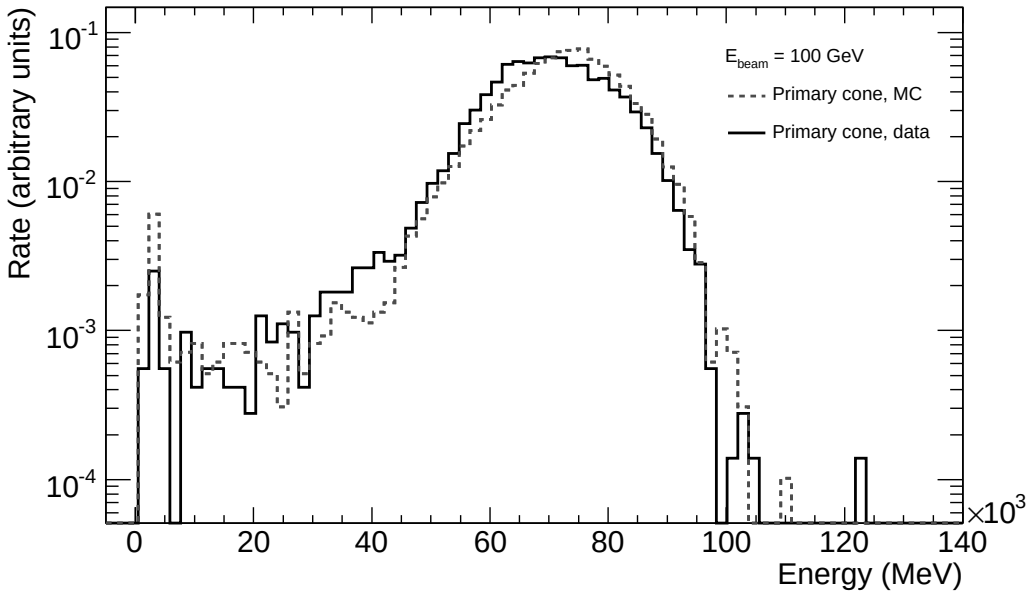

Figure 33: Cone energy distribution for a 100 GeV beam. Comparison between data (positive pions) and Monte Carlo simulation (MC). The proton contamination in real data can be seen as a shift towards lower values, compared to the distribution on the simulated energy.

not been able to make a comparison of the resolutions of π^- and π^+/p data beams of the same energy.

When comparing the energy density and the cone energy distributions, the agreement between data and simulations seems adequate. However, the simulation does not correctly describe the shower development in data, but underestimates the energy deposition in Tile and overestimates the deposition in LAr. In Figures 34 and 35, the energy distribution in LAr and Tile, for simulations and data, is given for the beam energies 100 and 250 GeV. The shower development mis-description in the simulation will affect the weights and the energy after weighting to a high degree, which is demonstrated in Section 4.5.

4.4 Correction for losses in dead material

In ATLAS, some regions are referred to as "dead", since energy lost in these regions is not recorded in any calorimeter system. In this sense, the inner detector is also "dead" from a calorimetry point of view. Another more significant dead region is the cryostat between the LAr and the Tile calorimeters. The energy lost in these dead regions must be accounted for in some way, in order to reconstruct the true energy of a particle. The methods for dead material corrections used in this note are, with a few exceptions, based on the schemes described in reference [33].

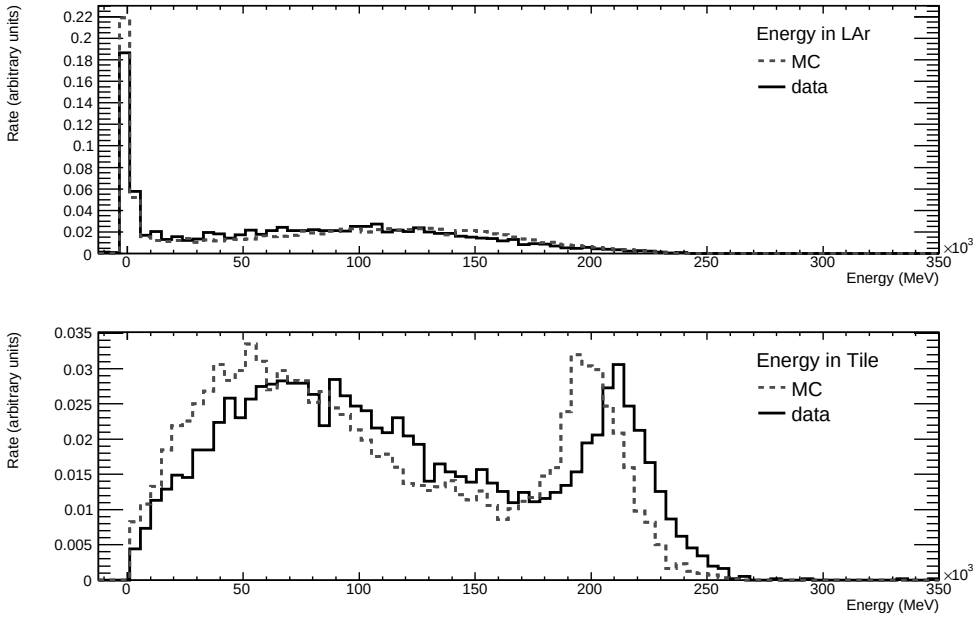

Figure 34: The energy distributions in the LAr and Tile calorimeters for 250 GeV beams. Comparison between Monte Carlo simulation (MC) and test beam data of a negative pion beam.

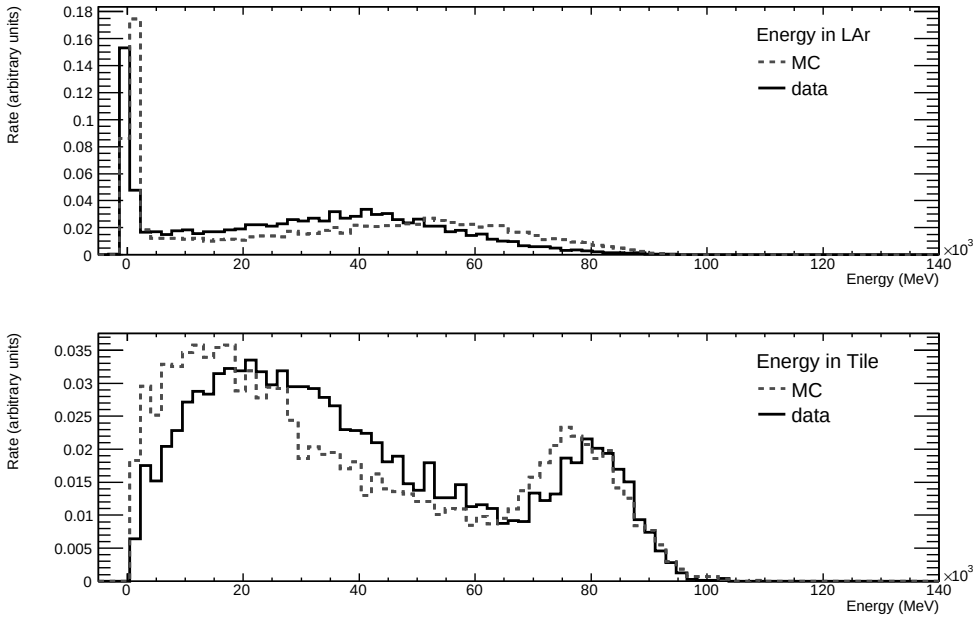

Figure 35: The energy distributions in the LAr and Tile calorimeters for 100 GeV beams. Comparison between Monte Carlo simulation (MC) and test beam data of a positive pion beam.

For the barrel region, there are four major dead regions to consider: the upstream region of material before the LAr pre-sampler, the material between the pre-sampler and the first LAr barrel sampling layer, the region between LAr and Tile, and any energy lost due to leakage beyond Tile, to either side of the calorimeters or in any other internal dead regions. The correction is made using information on the energy deposited in the calorimeter layers close to the dead region, or in some cases all of the deposited energy in the calorimeters. The correction constants are determined using the Monte Carlo truth information from the simulated pions. A schematic view of the dead regions is given in Figure 36. The sample used to derive the weight is also used to compute the dead material correction constants.

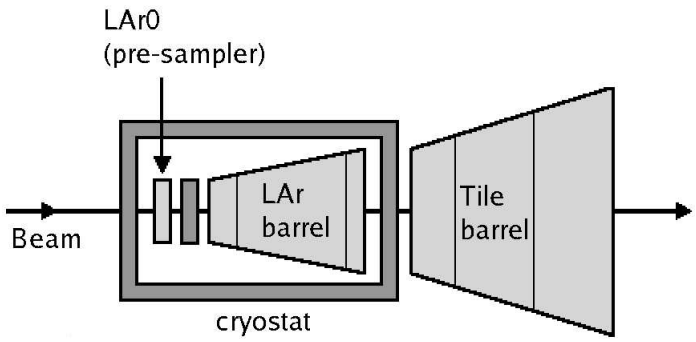

Figure 36: Schematic view of the dead regions in the test beam barrel set-up. The dead regions are drawn in dark grey, the active regions in a brighter shade. The upstream region consists of the cryostat before the pre-sampler. The dead material between the pre-sampler and the first layer of the LAr barrel is indicated as a bar. The largest energy losses occur in the part of the cryostat that is placed between the LAr barrel and the first Tile layer. The fourth category of dead material losses is leakages beyond Tile and laterally (not indicated in the figure).

The dead region correction constants are computed by plotting the true energy lost in the dead region of interest as a function of the uncalibrated energy in relevant parts of the calorimeter. A straight line though the origin is then fitted to the distribution. The slope of the fitted line, multiplied with the uncalibrated energy returns the energy in the dead region, if the correlation between the energy lost in the dead region and the energy deposited in the calorimeter layers in question was sufficiently strong. In Figure 37, examples of fits to energy lost in dead regions for simuated 100 GeV pions are given.

The upstream correction also calibrates the pre-sampler energy, which cannot be calibrated using the hadronic weighting scheme described in this note, as described in Section 3.5. The correction is given by the slope of a line fitted to the sum of the energy lost in the cryostat before the LAr pre-sampler ($E^{truth}_{upstream}$) and the true energy deposited in the pre-sampler, as given from the simulation ($E^{truth}_{presamp}$), as a function of the data-like uncalibrated reconstructed energy in the pre-sampler ($E^{0}_{presamp}$). The constant obtained, $C_{upstream}$, is used to estimate the energy lost before the pre-sampler ($E^{est.}_{upstream}$), and to calibrate the pre-sampler energy ($E^{est.}_{presamp}$), as

$$E^{est.}_{upstream} + E^{est.}_{presamp} = C_{upstream} \cdot E^{0}_{presamp} \tag{6}$$

The correction constant for the region between the pre-sampler and the first layer of the LAr

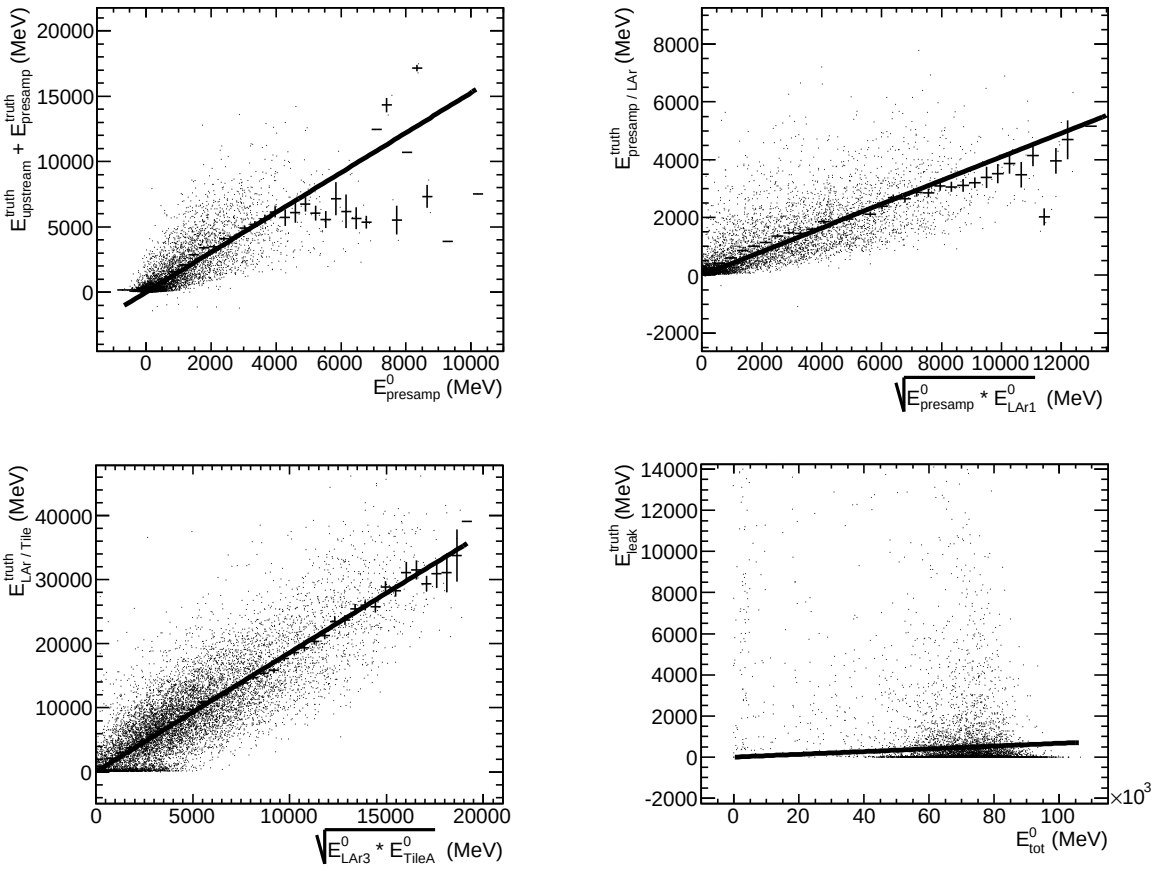

Figure 37: Example of energy depositions in dead region as a function of deposited energy in calorimeter layers. The labels and the choice of fits are described in the text.

barrel is given by the linear fit to the true energy deposited in the cryostat before the LAr barrel ($E^{truth}_{presamp/LAr}$) as a function of the geometric mean of the data-like energy in the pre-sampler ($E^{0}_{presamp}$) and the first sampling layer of the LAr barrel, LAr1 (E^{0}_{LAr1}). The estimated energy lost in the cryostat before LAr barrel, $E^{est.}_{presamp/LAr}$, is given as

$$E^{est.}_{presamp/LAr} = C_{presamp/LAr} \cdot \sqrt{E^{0}_{presamp} \cdot E^{0}_{LAr1}} \tag{7}$$

where $C_{presamp/LAr}$ is the slope of the fitted line.

The largest energy depositions in dead regions occur in the cryostat between LAr and Tile. The correction constant for this region, $C_{LAr/Tile}$, is obtained in the same fashion as for the region between the pre-sampler and the LAr barrel, and the energy used is the energy deposited in the last LAr sampling layer, LAr3 (E^{0}_{LAr3}) and the first Tile sampling layer, TileA (E^{0}_{TileA}). The estimated energy lost in the cryostat between LAr and Tile, $E^{est.}_{LAr/Tile}$, is thus given as

$$E^{est.}_{LAr/Tile} = C_{LAr/Tile} \cdot \sqrt{E^{0}_{LAr3} \cdot E^{0}_{TileA}} \tag{8}$$

For leakage beyond Tile, no correlation between energy deposited in any calorimeter layer can be seen. However, on average the leakage is dependent on the beam energy. As a first approximation, the estimated leakage, $E^{est.}_{leak}$, can be computed as a constant, C_{leak}, multiplied with the total reconstructed unweighted energy of all calorimeter layers (E^{0}_{tot}),

$$E^{est.}_{leak} = C_{leak} \cdot E^{0}_{tot} \tag{9}$$

The corrections for dead material are made on event basis and, except in the case of the pre-sampler energy, independent of the hadronic calibration. The total energy of an event after weighting and correction for losses in dead material, is computed as

$$E_{DMcorr} = E_{weighted} + (E^{est.}_{upstream} + E^{est.}_{presamp}) + E^{est.}_{presamp/LAr} + E^{est.}_{LAr/Tile} E^{est.}_{leak} - E^{0}_{presamp} \tag{10}$$

The reconstructed unweighted pre-sampler energy is subtracted, in order not to count the pre-sampler energy twice.

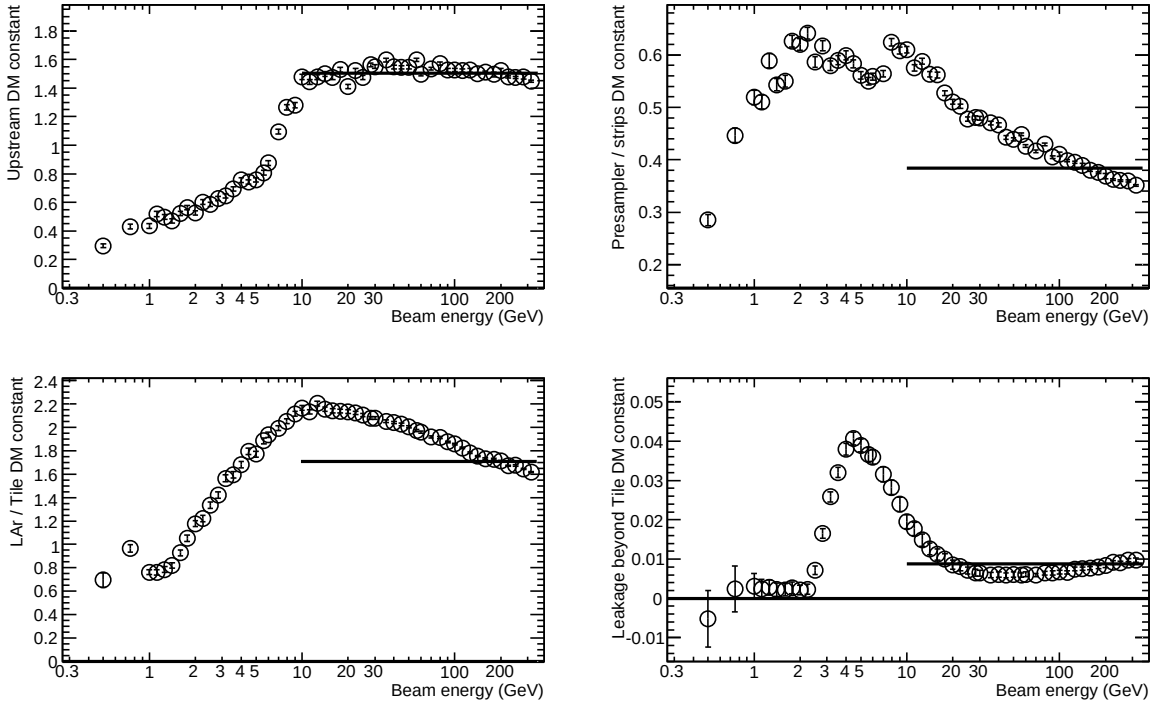

Figure 38: Dead material correction constants as a function of beam energy. The top left plot shows the correction constants for the upstream energy losses, before the LAr pre-sampler. The top right plot show the correction constants for the region between the pre-sampler and the LAr barrel. The bottom left plot show the dead material correction constants for the region between LAr and Tile, and the bottom right plot show the correction constants for leakage. The horizontal lines indicate the constant value when computed for all beam energies above and including 10 GeV. The values are given in Table 5. Conclusions on the behaviour of the correction constants as a function of beam energy are given in the text.

Dead material constants for the various regions as a function of beam energy are given in Figure 38. As shown in this figure, the correction constants for dead material are not constant

with respect to the beam energies. All corrections behave strangely for beam energies below ≈ 10 GeV, reflecting the fact that correction for dead material energy losses is hard at low energies. The peak in the distribution of correction constants for the leakage beyond Tile (bottom right plot in Figure 38) seems unexpected at first, but when considering that this constant must be multiplied with the total uncalibrated energy of the event to retrieve the leakage, the peak translates into an approximately constant leakage of about 100 MeV for beam energies between 4 and 30 GeV. For high beam energies, the leakage correction factors are roughly linear, as are the upstream corrections. The corrections obtained when using all beam energies above and including 10 GeV are indicated with horizontal lines in the plots.

For the corrections of losses in the regions before and after LAr barrel, the values do not flatten at energies above 10 GeV, but rather show a decreasing linear behaviour. This is most likely a manifestation of the increasing energy fraction of the true pion energy recorded by the calorimeters. The dead material compensation energy is in some sense calibrated on the hadronic scale, while the energies $\sqrt{E^0_{presamp} \cdot E^0_{LAr1}}$ and $\sqrt{E^0_{LAr3} \cdot E^0_{TileA}}$ are not. When multiplying the correction constants with the unweighted energy, the correction constants must decrease to follow the increase in visible energy in the calorimeters.

Constant	value (dimensionless)
$C_{upstream}$	1.5023 ± 0.0022
$C_{presamp/LAr}$	0.38399 ± 0.00049
$C_{LAr/Tile}$	1.7014 ± 0.0011
C_{leak}	$(8.729 \pm 0.085) \cdot 10^{-3}$

Table 5: Values of the dead material correction constants, for the four different regions considered.

The dead material losses correction constants not being constant over the beam energies will affect the value of the corrected energy. Ideally, a correction based on the beam energy would be used. In test beam data, the beam energy is well-known. However, this is not the case for pions or jets in ATLAS during real data taking, which is the reason for using one correction constant per dead region, rather than making the recourse to beam energy dependent corrections. In Figure 39, the linearity of the weighted energy with dead material correction is shown, both with and without the beam energy dependence in the correction constants. In Figure 40, the difference of the linearities in dead material corrected energy ins shown, and in Figure 41, the difference in resolution is given.

As demonstrated in Figure 40, the beam energy independent dead material corrections will give a systematically too low reconstructed weighted energy for most of the beam energies considered. The worst underestimations of the energy will occur for beam energies around 10 GeV, where the shift is as much as 4%. The resolution, on the other hand, is not affected in a significant way when the dead material corrections constants are beam energy independent, as shown in Figure 41.

For the remainder of this note, whenever an energy is said to have been corrected for dead material losses, the correction of Equation 10 have been applied, using one correction constant for each dead region, same constant for all beam energies. Unless something else is stated, the

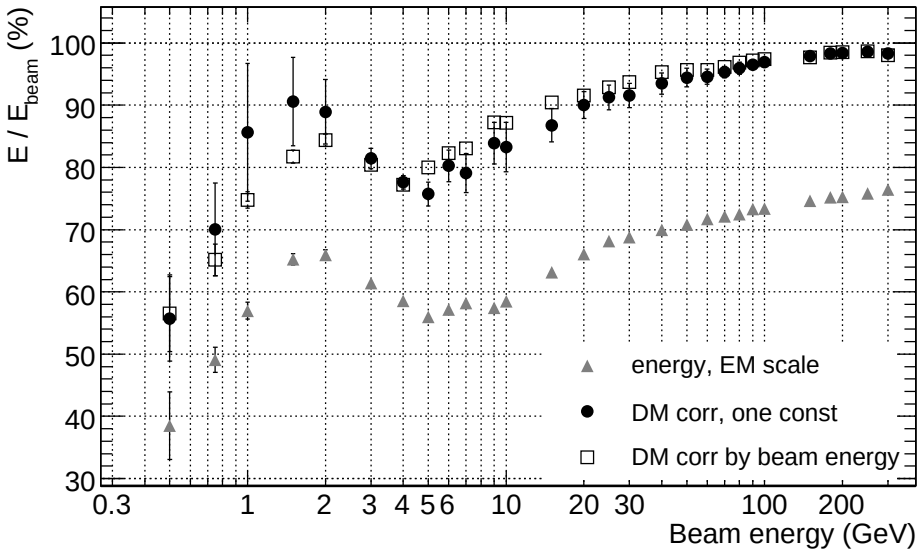

Figure 39: E_{mean}/E_{beam}, where E_{mean} comes from a Gaussian fit to the energy distribution, as a function of the beam energy. The unweighted energy on the electromagnetic scale is marked by grey triangles. The black circles mark the weighted and dead material corrected energy using one constant per region, same for all beam energies. The squares mark weighted and dead material corrected energy using beam energy dependent DM correction constants. The error bars at the black circles are computed from the errors of the Gaussian fit and the distance to the beam energy corrected points (systematic uncertainties). The error bars on the other markers are from Gaussian fits only.

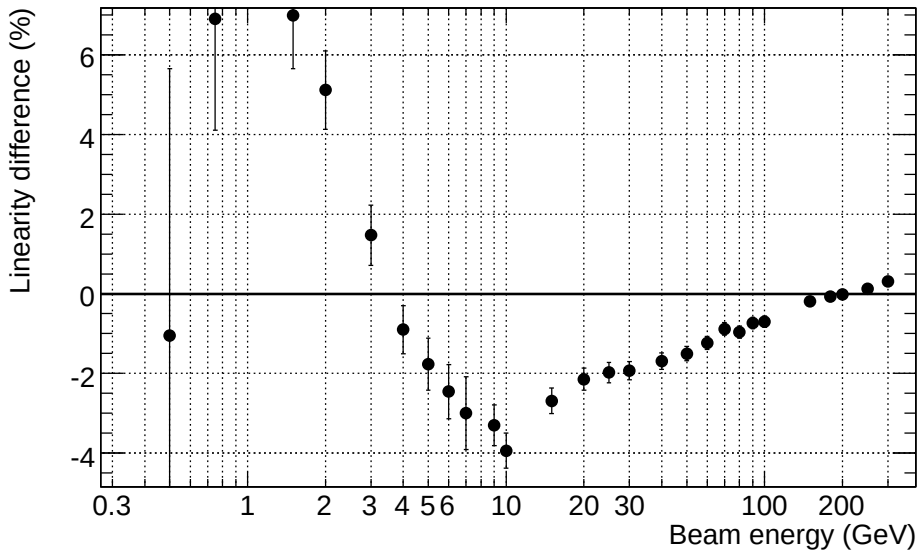

Figure 40: Difference of linearities, linearity from one correction constant per region minus linearity using beam energy dependent corrections. The uncertainties indicated are the errors from the Gaussian fit of the linearity from the dead material correction with one constant per dead region.

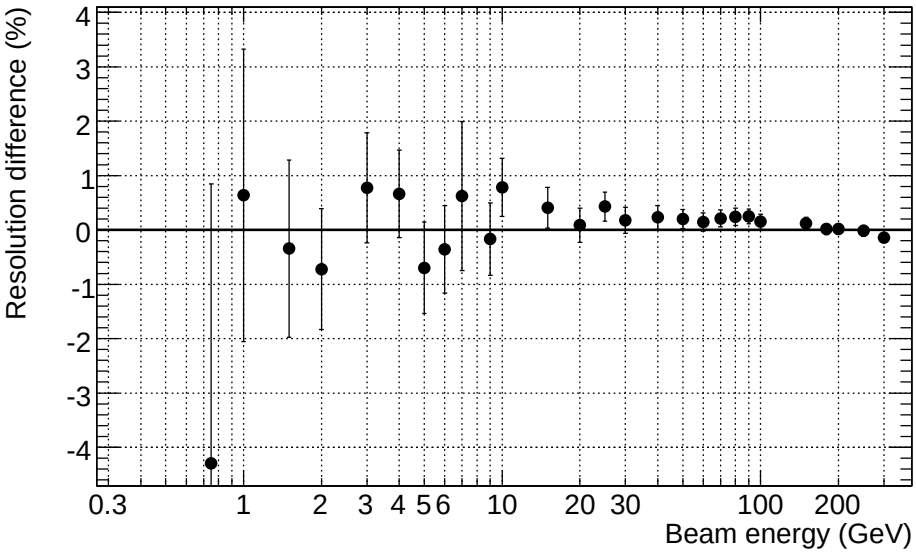

Figure 41: Difference of resolutions, resolution from one correction constant per region minus resolution using beam energy dependent corrections. The error bars indicate the errors of the resolution from the dead material correction with one constant per dead region.

constants have been obtained from all beam energies above and including 10 GeV, as described in this section. The values of the corrections are given in Table 5. The deviations from the values obtained using the beam energy dependent corrections are treated as systematic uncertainties. The values are given in Appendix B.

The dead material correction constants computed here are valid only for pseudorapidities close to $\eta = 0.45$, since the dead regions are different at other η, and only in the test beam set-up, because the cryostat in the full ATLAS set-up is slightly different. Moreover, these constants are only valid for pions, since the shower development of electrons in the calorimeters is different from the shower development of pions. For instance, the energy leakage of electrons is smaller and electrons seldom reach the Tile calorimeter.

4.5 Linearity and resolution of pions from real data and simulations

In Section 3.6, the weighted energy was compared to the Monte Carlo truth energy obtained from the simulation. For the test beam data, the only "truth" we have is the beam energy. Moreover, after correction for energy losses in dead material, we expect the energy distribution to be Gaussian. Hence we can make a sensible Gaussian fit to the distribution, use the ratio E_{mean}/E_{beam} for the linearity, and compute the resolution as σ/E_{mean}. In Figure 42 a comparison of the data and Monte Carlo linearity of weighted and unweighted energy is shown.

The most striking feature of the linearity in Figure 42, is that even after weighting it is a bit

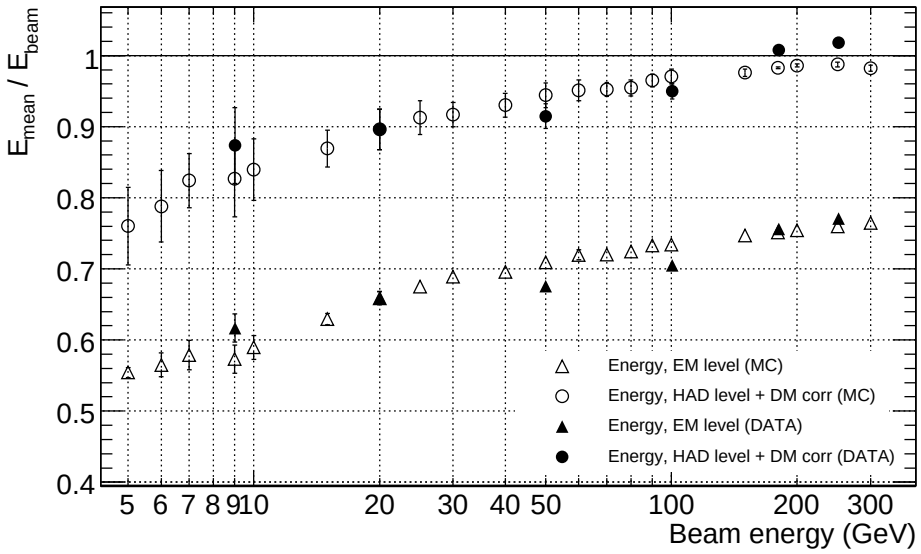

Figure 42: Linearity, E_{mean}/E_{beam}, of weighted and unweighted energy (Monte Carlo simulation, MC, and data) as a function of beam energy. Comparison between the unweighted energy on the electromagnetic scale (triangles), and weighted and dead material corrected energy (circles). Data points are marked with filled symbols, simulation with open symbols. It should be noted that data runs of beam energy 250, 180 and 9 GeV are negative runs, while beam energies 100, 50 and 20 GeV are positive runs with proton contamination.

short of unity for most of the beam energies, especially the lower ones. This is partly an effect of energy falling outside the topo clusters [8,34,35], but in the test beam case, lateral leakage in the ϕ direction can also occur, which does not happen in the full ATLAS set-up. Corrections for the out-of-cluster energy should be done to retrieve the full energy of an event. This is not done for singe pions within this note, but only for jets in the full ATLAS environment, as described in Section 6. Since the treatment of the energy lost due to clustering differs between the test beam and the full ATLAS set-ups, and we only strive to make a study of the hadronic weighting scheme when applied to test beam data, which can be done after weighting and subsequent corrections for losses in dead material, the corrections for energy depositions outside the clusters are omitted.

The overestimation of data energy in the highest energy points can be explained by the shower development mis-description in the simulation, which was shown in Section 4.3. The imbalance between the energy depositions in LAr and Tile will lead to an imbalance in the weights. Since the simulation underestimates the energy depositions in Tile, the Tile weights will be higher than they should be. In the same way, the LAr weights will be lower. Since the LAr weights are closer to unity than the Tile ones, the raising effect of the Tile weights can be expected to dominate. When the weights are applied to data, the overestimation observed for the negative pion beams is the result.

When the above mentioned effects are accounted for, the data and simulation linearities in Figure 42 are in acceptable agreement.

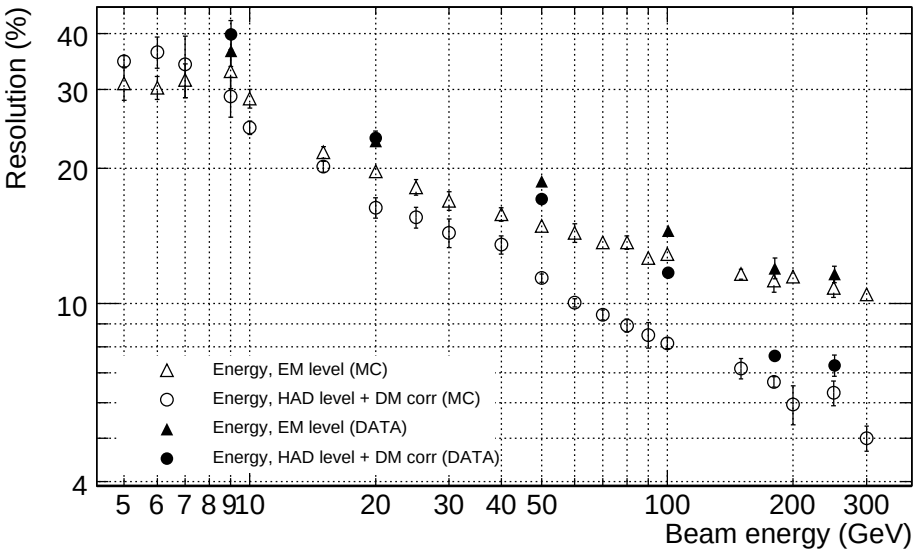

Figure 43: Resolution of weighted energy (simulation and data) as a function of beam energy. Comparison between the unweighted energy on the electromagnetic scale (triangles), and weighted and dead material corrected energy (circles). Data points are marked with filled symbols, Monte Carlo simulation with open symbols. It should be noted that data runs of beam energy 250, 180 and 9 GeV are negative runs, while beam energies 100, 50 and 20 GeV are positive runs with proton contamination.

In Figure 43, the resolution of the weighted and unweighted energy is given as a function of the beam energy, and in Figure 44, the difference of the resolution is shown.

For the resolution, there are quite large differences between data and simulation. For all beam energies, the resolution of data energy is worse than the resolution of the simulated energy signal, which most likely reflects the generally more difficult conditions in real data taking, such as noise unaccounted for and scattering in the beam line. Since the general worsening in resolution in data compared to the simulation is present in the electromagnetic scale energy, this is not an effect of the weighting scheme. For comparison, it is interesting to compute the difference between the resolution of the unweighted energy and the resolution after weighting, which is shown in Figure 44. Even though the resolution of data energy is much worse than for the simulated energy signal, the weighting and dead material correction improve the resolution for energies above 20 GeV. For the simulated energy signal, the resolution improvement is achieved for beam energies above 8 GeV.

In Figure 45 the resolution is plotted as a function of $1/\sqrt{E_{beam}}$, and the simulated energy resolution has been fitted with the function $r = a/\sqrt{E_{beam}} \oplus b$. The values of the parameters are given in Table 6. No fit is made to the data energy resolution, because of the possible disturbances of the resolution as a result of the proton contamination in the positive runs.

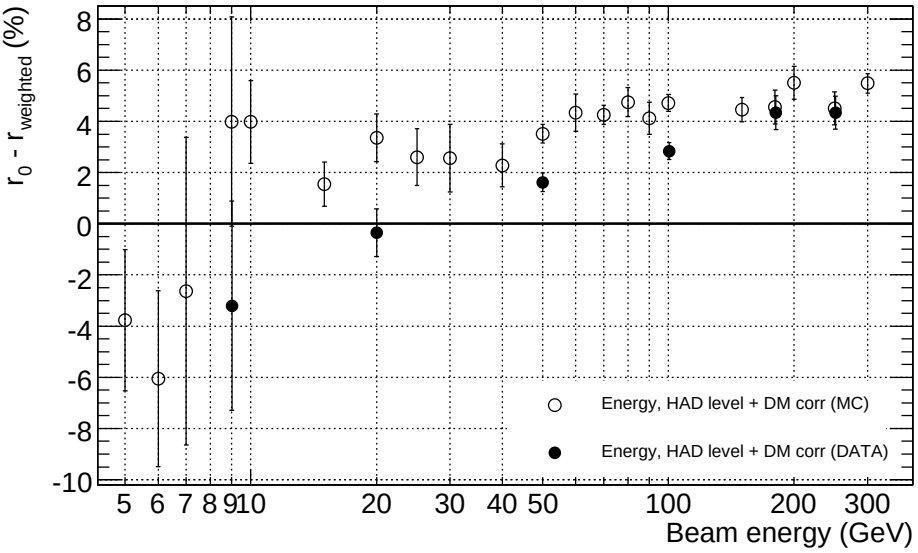

Figure 44: Difference of resolutions, $r_0 - r_{weighted+dead\ material\ corrected}$ as a function of beam energy. A positive value in this plot means that the weighting and dead material correction procedure improves the resolution. Comparison between Monte Carlo simulation (open circles) and data (filled circles). It should be noted that data runs of beam energy 250, 180 and 9 GeV are negative runs, while beam energies 100, 50 and 20 GeV are positive runs with proton contamination.

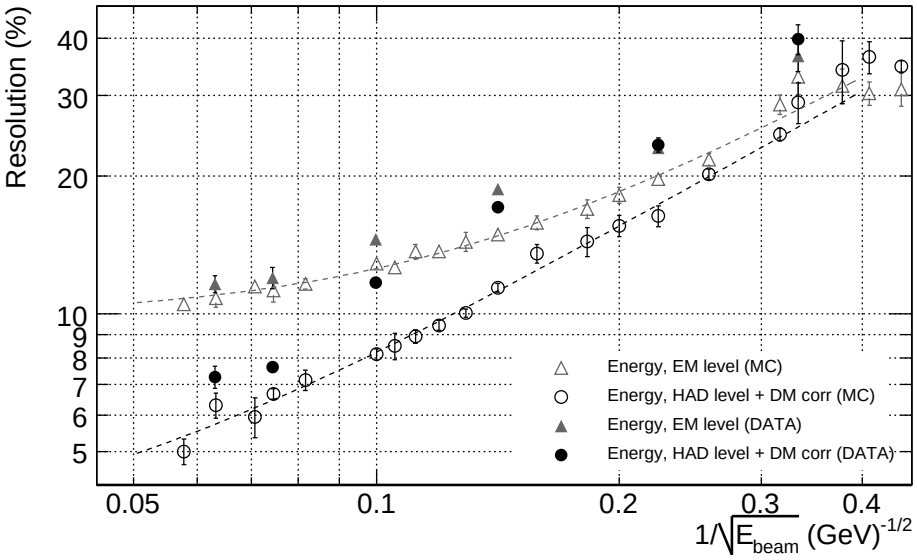

Figure 45: Resolutions of weighted and unweighted energy (Monte Carlo simulation and data) as a function of $1/\sqrt{E_{beam}}$, with fits to the function $r = a/\sqrt{E_{beam}} \oplus b$. The values of the parameters are given in Table 6. It should be noted that data runs of beam energy 250, 180 and 9 GeV are negative runs, while beam energies 100, 50 and 20 GeV are positive runs, with proton contamination.

Unweighted energy			Weighted + DM corr energy		
$a(\% \cdot GeV^{1/2})$	$b(\%)$	χ^2/NDF	$a(\% \cdot GeV^{1/2})$	$b(\%)$	χ^2/NDF
78.4 ± 1.4	9.80 ± 0.16	$15.00/17$	76.2 ± 1.1	3.12 ± 0.32	$15.59/17$

Table 6: Parameters of fit to the resolution of the simulated energy signal, $r = a/\sqrt{E_{beam}} \oplus b$, as drawn in Figure 45.

5 Stability checks and comparisons with other methods

In the previous sections of this note, the weighting scheme has been described and the performance of the weighting when applied to simulations and real data from the combined test beam has been demonstrated. In this section, we show the performance of the weighting scheme under slightly different conditions, such as various changes in the global energy scale.

5.1 Energy of a single cluster as the global energy

The default local calibration method for jets currently in use in the ATHENA framework does not use the energy of a cone of topo clusters as the global energy scale, but rather the energy of a single topo cluster (the "cluster" method) [8]. For the understanding of the method and the underlying mechanisms of local hadronic calibration, it is important to investigate both these schemes, to see if they perform differently.

In this section, the performance of the cluster method when applied to simulations and data is compared to the results from our standard approach (the "cone" method), as presented in Section 4.5.

The weighting factors for the cluster method is derived in the same way as the cone method weights (see Section 3), with the same weight restrictions. The only difference is that when the cone method only uses the most energetic cone of each event for the weight computation, the cluster method uses all topo clusters of each event to fill the weight tables. The cluster method weights are parametrised with the cell energy density and the topo cluster energy, and one weight table for each sampling layer is made. When applying the weights, only cells with an absolute energy density larger than the estimated noise level are weighted, as described in Section 3.4.

In Figure 46, the linearity of the energy after weighting and correction for dead material losses is shown, for both methods. The linearity is computed as the mean of a Gaussian fitted to the energy distribution divide by the beam energy, E_{mean}/E_{beam}, and plotted as a function of the beam energy. In Figure 47, the difference between the resolution of the unweighted energy and the energy after weighting and dead material correction is shown. The absolute values of the resolution of the energy after weighting with the cone method is shown in Figure 43 in Section 4.5.

The performances of the cone and cluster methods are very similar, as shown in Figures 46-

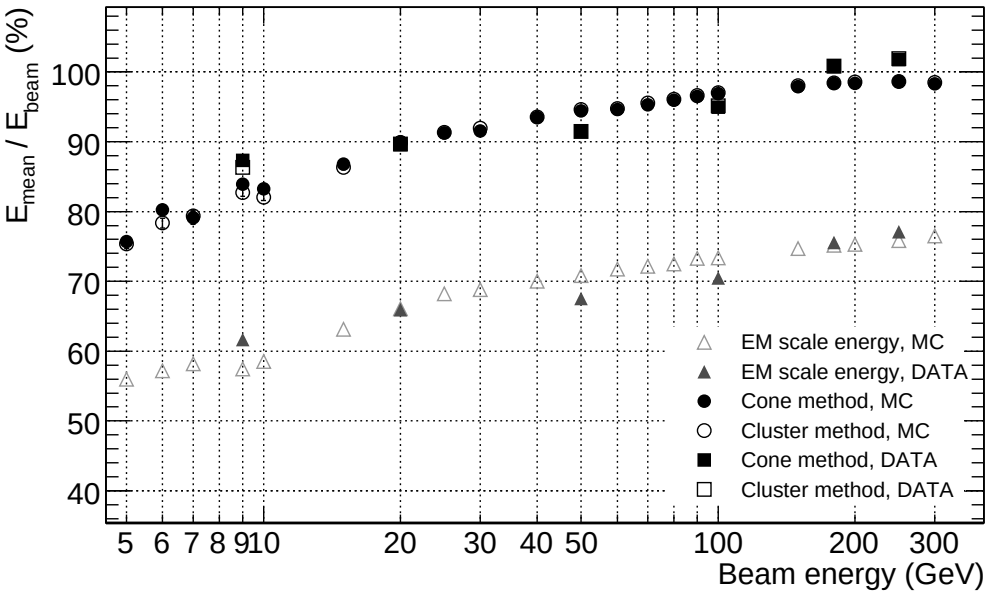

Figure 46: Linearity of weighted and dead material corrected energy (Monte Carlo and data) as a function of beam energy. Comparison between our standard approach (the cone method) and the cluster method, as described in the text. The uncertainties given are the statistical uncertainties from the Gaussian fits.

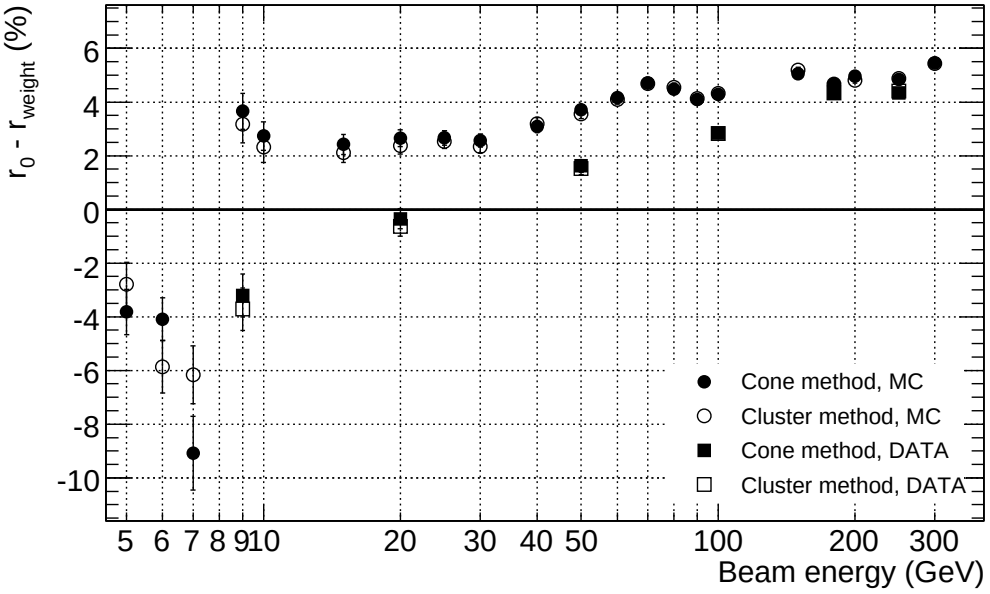

Figure 47: Difference between the resolution of the unweighted energy on the electromagnetic scale, r_0, and the weighted and dead material corrected energy r_{weight} as a function of beam energy. Comparison between our standard approach (the cone method) and the cluster method, as described in the text. The uncertainties given are the statistical uncertainties from the Gaussian fits.

47, both when applied to data and Monte Carlo simulations. A very small systematic shift towards slightly higher linearity for the cone method in the beam energy region between 5 and 20 GeV might be seen, but this shift is within the statistical errors.

The similarity between the methods indicate that weighting procedures like these are stable and not sensitive to minor changes in the global energy scale or cluster size. In the rest of this section, the stability of the method is shown in other ways.

5.2 Distortion of the cone energy

The test-beam environment is very "clean" compared to what we can expect from data taking in ATLAS. In the high-energy proton-proton collisions, we will face problems with pile-up noise, underlying event and low-energy debris from the collisions in the detector. In the previous section, we showed that the weighting scheme works well when the global energy scale is the energy of a single cluster. However, for the cluster method, the weights were derived specially, with the intention of using them in combination with the cluster energy as the global energy. If the underlying event distorts the cone energy by introducing additional energy preferentially in the inner calorimeter cells, then the weighting of the outer cells might be affected.

In order to make a very simple check of the performance under slightly more complicated conditions, we have deliberately distorted the cone when choosing the weights. The weight tables used are the same as before, but when picking the weights, we use the weights belonging to a cone of 10% higher energy. This way, a first-order test assessing whether the underlying event distortion to the cone would disturb the outer cells can be made.

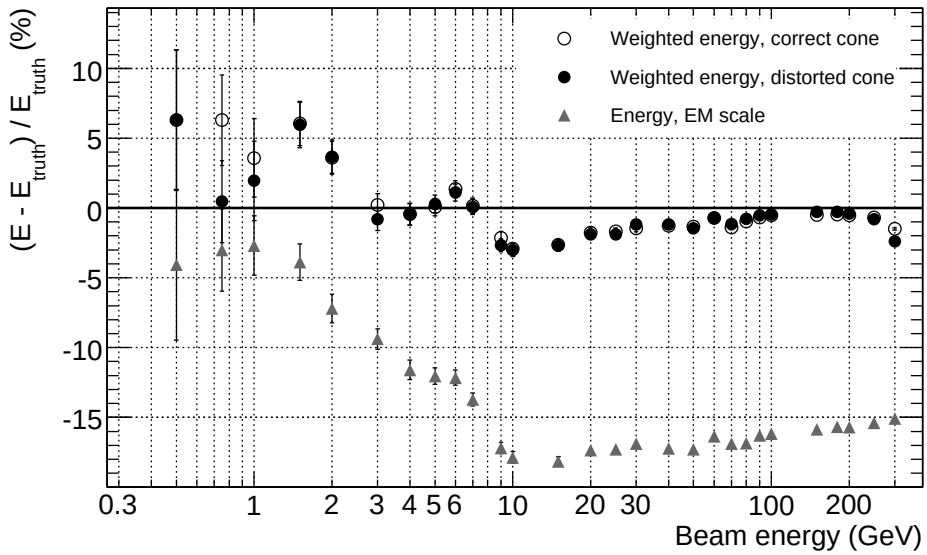

Figure 48: Linearity of weighted energy (simulation) using a deliberately distorted cone.

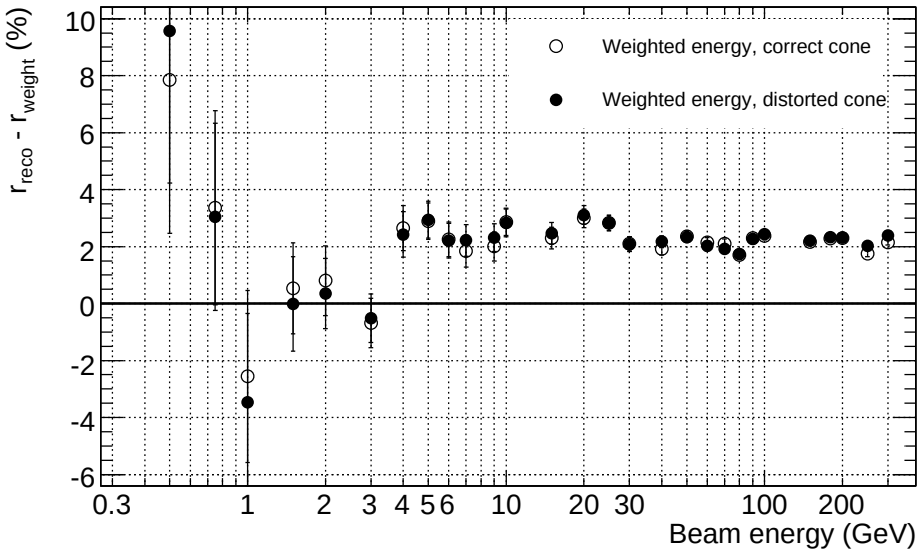

Figure 49: Difference of resolutions of weighted and unweighted energy (Monte Carlo) using a deliberately distorted cone.

In Figure 48, mean values of Gaussians fitted to the distribution $(E - E_{truth})/E_{truth}$ for the weighted energy is shown, both when using the correct cone energy, and in comparison to the distorted cone energy. As before, E is the weighted or unweighted energy and E_{truth} is the truly deposited energy as given from the Monte Carlo simulation. In Figure 49, the difference between the resolution of the unweighted energy and the weighted energy is plotted as a function of the beam energy. The resolution is estimated as $\sigma/mean$ of a Gaussian fitted to the distribution E/E_{truth}.

As shown in Figures 48-49, the cone method is stable against small changes in the cone energy scale. The only point where the cone distortion has a significant effect is for beam energy 300 GeV, where the linearity is worsened after the cone distortion. This is most likely a weight table border effect, see Section 5.4. For the future, a full systematic study of the impact of the underlying event on the performance of the hadronic calibration is needed.

5.3 Variation of the cone size

In all previous applications of the cone-based weighting in this note, the cone opening angle has been 11°, which is the cone opening angle used when this method was applied in the H1 experiment [6]. Changes of the cone opening angle might affect the performance of the weighting, and should be studied.

In order to study the properties of the weighted energy when the cone opening angle is changed, a set of new weight tables were produced, using the energy from cones with the

opening angles 2, 8, 14, 20 and 26° as the global energy. These weight tables were applied to simulated energy signals, similar to the procedure described in Section 3. From a Gaussian fitted to the weighted and dead material corrected energy distribution, the linearity can be computed as E_{mean}/E_{beam} and the resolution as σ/E_{mean}. In Figure 50, the difference between the linearity obtained for the normal weighting procedure (opening angle 11°) and the linearity after applying weights from other cone sizes are shown. In Figure 51, the differences in resolution is shown. These plots should be compared with Figures 42-43 in Section 4.5, where the absolute values of the linearity and the resolution is shown.

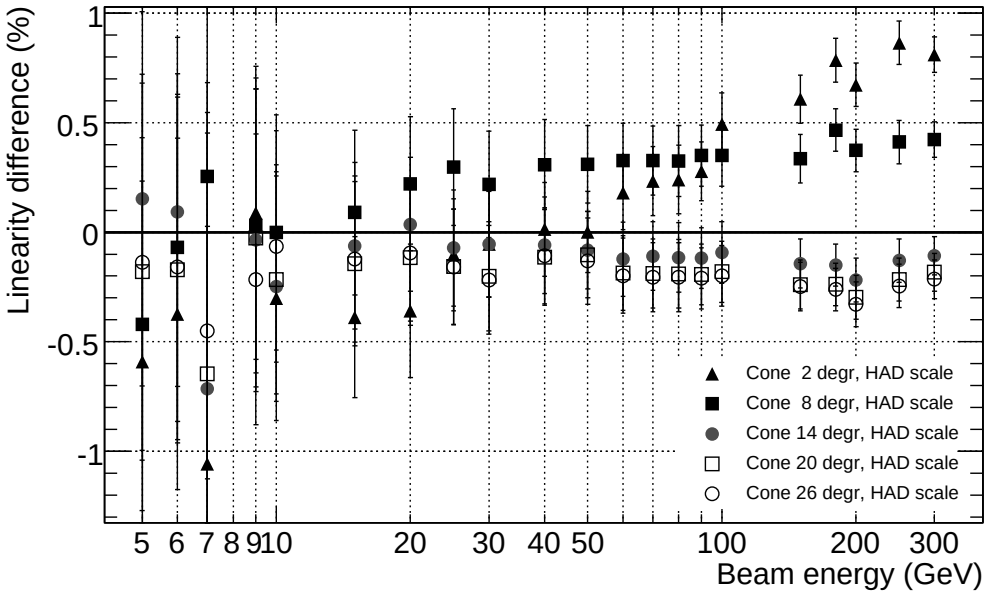

Figure 50: Difference between E_{mean}/E_{beam} of the weighted energy when using weight tables for a cone with opening angle 11° and other opening angles. The uncertainties indicated come from the statistical uncertainties of the Gaussian fits.

The changes in linearity when varying the cone size are very small, as shown in Figure 50, but a clear pattern can be seen in the grouping of the linearity. A smaller cone opening angle (2 or 8°) leads to a lower E_{mean}/E_{beam} ratio than in the 11° case, whereas a larger opening angle (14, 20 or 26°) leads to a larger E_{mean}/E_{beam} ratio. The shifts are within the statistical errors for beam energies lower than about 100 GeV, and for the higher beam energies the effect is less than 0.9%. The resolution is not affected by the cone size changes in any systematic way, as shown in Figure 51.

5.4 Discussion on the validity of the weights

In Section 3.6, an unexpected drop in the linearity at the highest beam energies investigated was observed. A similar but more pronounced effect was also seen when the cone energy was

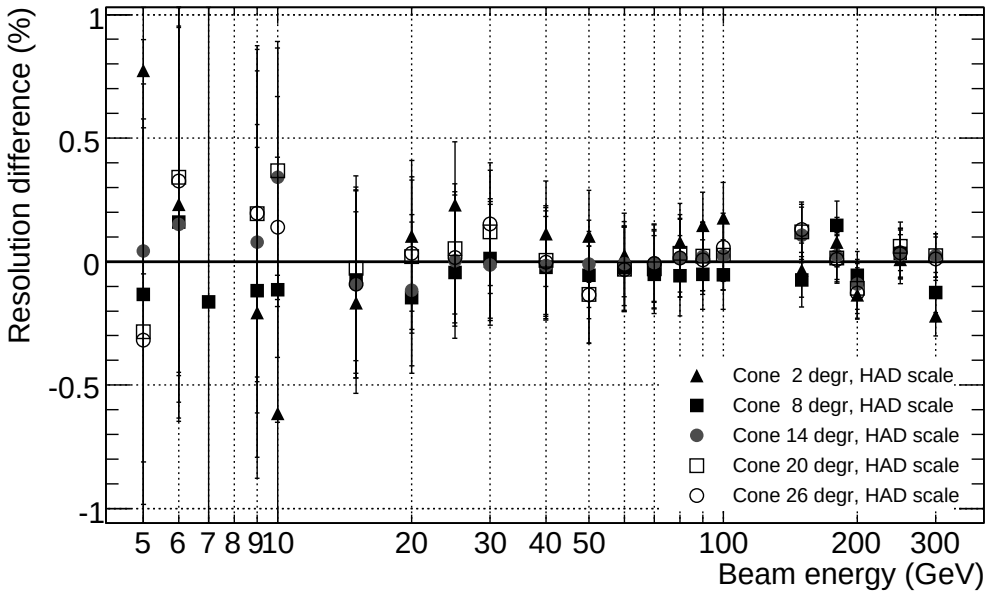

Figure 51: Difference between σ/E_{mean} of the weighted energy when using weight tables for a cone with opening angle 11° and other opening angles. The uncertainties indicated come from the statistical uncertainties of the Gaussian fits.

deliberately distorted in Section 5.2. The drop in linearity is an effect of some of the cone energies being close to the border of the weight table, which can be demonstrated with a shortened weight table, where only simulated samples of beam energies up to 200 GeV have been used to compute the weights. In Figure 52, the mean value of the distribution $(E - E_{truth})/E_{truth}$ is plotted as a function of the beam energy, where E is either the energy after weighting with our usual weight tables, or with the weight tables derived for beam energies up to 200 GeV only.

The effect on the linearity when using the shortened weight tables, as shown in Figure 52, clearly demonstrates the border effect: when applying weights to cells from an event with a beam energy close to the maximal beam energy used to compute the weights, the linearity drops, and this drop does not only affect the largest beam energy used for making the weights, but beams at lower energies too. In the example shown here, with weights computed from beam energies up to 200 GeV, the unexpected drop in linearity begins at beam energies around 150 GeV.

From this demonstration, a very important feature of the weighting can be seen: when applying the weights, it is important to make sure that a variety of beam energies, both larger and smaller than the energy of the sample which is to be weighted, were used in the computation of the weights.

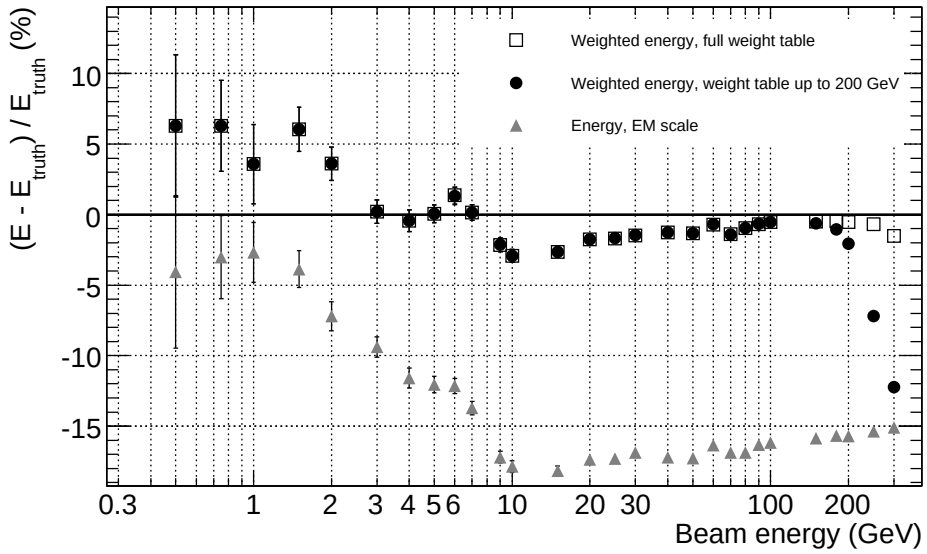

Figure 52: Linearity of weighted simulated energy using a shortened weight table (where the weights have been computed using beam energies up to 200 GeV only), and the linearity of the energy which has been weighted with the default weight tables (beam energies up to 316 GeV).

5.5 Properties of the electromagnetic scale energy

In all comparisons between weighted or unweighted energy and the true energy depositions as given from the simulation, an unexpected rise in the $(E - E_{truth})/E_{truth}$ ratio has been observed for beam energies lower than about 10 GeV. In Figure 53, properties of the electromagnetic scale energy are investigated. By looking at the electromagnetic scale energy within topo clusters, $E_{0,\ clusters}$ in relation to the electromagnetic scale energy in all calorimeter cells, $E_{0,\ all\ calo\ cells}$, and in relation to the visible energy truly deposited in the calorimeter cells, $E_{visible}$, we can disentangle the effects of noise in cells (which is not present in $E_{visible}$) and the topo clustering (which is only used in $E_{0,\ clusters}$). In Figure 53, it is clearly demonstrated that the unexpected rise in the $(E - E_{truth})/E_{truth}$ ratio at low beam energies is an effect of the overlaid noise in the cells, since this effects disappears when we consider the visible energy only.

It should be noted that the unexpected rise in linearity only is visible when comparing energy event-by-event with the Monte Carlo truth energy. If the electromagnetic scale energy is compared to the beam energy, as in Figure 13 in Section 3.3, the linearity behaves as expected.

6 Application to jets in ATLAS set-up

The previous part of this note demonstrated that a method of local hadronic calibration using a weighting algorithm could be successfully developed and applied within the framework of

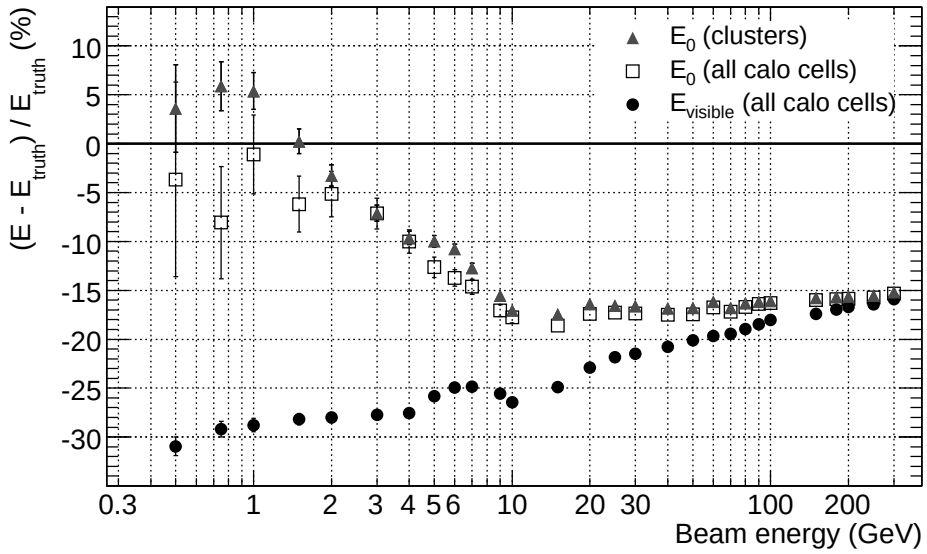

Figure 53: Properties of the electromagnetic scale energy in relation to the Monte Carlo truth energy. The ratio $(E - E_{truth})/E_{truth}$ plotted as a function of beam energy, where E is the electromagnetic scale energy within topo clusters, the electromagnetic scale energy within all calorimeter cells, or the true visible energy deposited in the cells, $E_{visible}$, as given from the simulation.

the reduced ATLAS detector, as was used during test beam running. In this section the local hadronic calibration scheme is studied under the conditions expected during luminosity running. The complete ATLAS detector is considered and, in place of single test beam particles, the performance of the calibration method is assessed using a simulated sample of dijet events.

This section is organised as follows. First a description is given of how the weights were extracted and applied, followed by an explanation of further calibration corrections (e.g. dead material corrections). The simulated data samples and the jet algorithms which were used in the performance tests are then outlined. Finally, the linearity and resolution of jet energy reconstruction for the different variations of local hadronic calibration are studied and compared with results from a global calibration approach with the emphasis lying on the comparison between the local hadronic calibration methods.

6.1 Weight extraction and implementation of cone method in the full ATLAS setup

The local hadron cone calibration method has now been fully implemented within the ATHENA package [36] and weights have been extracted for the full ATLAS set-up. To obtain the weights simulated data-sets of single pion events, uniformly distributed in η and ϕ, were used. Each simulated file contained 4522 events for a specific pion energy. The energy range spanned 1-1000 GeV, with the energy intervals logarithmically equidistant. These single pion files were

generated and simulated with ATHENA 12.0.31.

The weight derivation method follows the approach used in the test beam analysis, which is outlined in Section 3. The weights were derived using only the leading cone with an opening angle of 11 degrees, using the cone energy and the energy density of each cell as parameters. Weight tables were made separately for each sampling layer of each calorimeter system. Tables were computed for $|\eta|$ values in the range 0.0 to 5.0 in intervals of 0.2 [8)].

The weighting in the full ATLAS setup is implemented in several steps: clustering, classification, weighting and corrections for energy depositions outside the clusters and in dead regions.

First, the cluster algorithm is applied. The clusters are then classified as hadronic or electromagnetic, taking into account their energy density and their shower depth and the global probability for an electromagnetic or hadronic cluster to fall into a bin with the respective values of energy density and shower depth. The probability values were derived from the generated charged single pions which were compared to a sample of neutral pions. At the moment about 15% of the hadronic clusters are misclassified as electromagnetic, whereas only about 5% of the electromagnetic clusters are misclassified as hadronic [37]. These mis-classifications contribute about 3% to the non-linearity still seen for the local hadronic calibration methods [37].

After the classification, hadronic compensation weights are applied to cells within the hadronic clusters only.

A further correction step accounts for energy depositions from pions which are in the calorimeters but outside the selected clusters. These out-of-cluster weights are applied only to hadronic clusters, again using two-dimensional lookup tables, which are parametrised as function of cluster energy and cluster depth. The tables give an estimate of how much energy propagates outside a totally isolated cluster. But as clusters can have neighbouring clusters, into which their out-of-cluster energy can propagate, this primary out-of-cluster weight needs to be weighted by the degree of isolation of the cluster. The finally applied out-of-cluster correction is the product of the out-of-cluster corrections determined on isolated clusters, i.e. without taking into account any neighbouring clusters, and the degree of isolation of the cluster. The later is determined by the layer weighted energy ratio of the number of all neighbouring 2D cells *not* included in any other cluster to the number of all neighbouring 2D cells. For example, if a cluster is totally isolated, this means all its neighbouring cells are *not* in any other cluster and this ratio becomes 1 and as a consequence the full out-of-cluster weight is applied. On the other hand, if a cluster is completely surrounded by other clusters, all its neighbouring cells are inside the other clusters, so that the out-of-cluster weight becomes 0. The final out-of-cluster weight is applied multiplicatively as $w_{\mathrm{ooc}} = 1 + w_{\mathrm{ooc}}^{\mathrm{isol}} \times \mathrm{isolation}$ [37].

An additional correction step is the application of dead material corrections, which are correcting for unseen energy depositions in other parts of the detector, including the pre-sampler

[8)] In order to suppress noise, a restriction on the ratio $E^{\mathrm{reco}}/E^{\mathrm{true}}$ was implemented when deriving the weights, as described in Section 3.4. The ranges were $0.5 < E^{\mathrm{reco}}/E^{\mathrm{true}} < 3$ for the electromagnetic calorimeters and the forward calorimeter and $0.5 < E^{\mathrm{reco}}/E^{\mathrm{true}} < 5$ for the hadronic endcaps and to $0.5 < E^{\mathrm{reco}}/E^{\mathrm{true}} < 10$ for the hadronic Tile calorimeter [37, 38].

and the gap between the barrel and the extended barrel in the Tile calorimeter [37].

The local hadron calibration method calibrates to the true energy deposited in the clusters. Any jet reconstruction algorithm which runs over these calibrated clusters will not sum all the energies which belong to a "true" jet, and clusters will be missed. In order to reconstruct the "true" jets on particle level, further physics-dependent out-of-jet corrections are needed. Such corrections are meant to ensure that the reconstructed energy of a jet represents the true particle jet energy and thus the energy of the parton (see Section 6.2). As the out-of-jet corrections are not yet determined, they contribute to a systematic underestimation of the jet energy, when using the local calibration approach.

These missing out-of-jet corrections include corrections for the reconstruction efficiency, which account for the fact that a low energetic pion might not reach the calorimeter and does not form a cluster. This effect was estimated to amount to about 3% for jets with transverse momentum (p_T) between 140 and 280 GeV. The underlying assumption is that the leading particle takes around 25% of the total jet energy and that the remaining 30-40 jet particles have an energy spectrum of $\sim 1/E$. If none of the particles with a p_T below 500 MeV reaches the calorimeter and the reconstruction efficiency as determined for single pions is taken into account, then the reconstruction and low p_T losses can be estimated to be around 3% [39]. Other out-of-jet corrections correct losses due to magnetic bending, which bends low energy particles out of a jet. This effect is estimated to be around 2% [37]. Adding further 3% missing corrections due to the misclassification of clusters, the missing corrections in the energy range of $140 < p_T < 280$ GeV add up to around 8%, which is in agreement with the findings in that particular kinematic region presented later.

However, an underestimation of the true jet energy of 8% is only true for this energy region. Corrections for out-of-jet losses are in fact energy dependent, as high energy jets are more narrow due to the initial boost on the fragmenting initial parton. Thus, high energy jets have a larger fraction of their energy contained in a (sub-)cone of a fixed size around their axis [40]. Consequently, low energy jets will in general have more energy leaking out of the jet cone as compared to high energy jets. These energy losses are a source of underestimation of the true jet energy, when comparing reconstructed jets without jet corrections to true particle jets. Therefore it is expected that without these out-of-jets corrections, the reconstructed jet energy will still underestimate the true particle jet energy, and also that this underestimation is in fact depending on the true particle jet energy. Jets reconstructed in a compensated calorimeter will have to be subject to further physics-dependent corrections, that will be developed to be used on top of the local hadron calibration method.

6.2 Jet algorithms and jet samples

In a Quantum Chromodynamics (QCD) picture of proton collisions at the LHC, the partons of the proton may take part in a hard scattering, described by perturbative QCD (pQCD), which leads to a partonic final state comprising the outgoing partons from hard-subprocess plus additional initial and final state QCD radiation. Due to colour confinement, the partons can never be observed freely but fragment into hadrons, a process also called hadronisation, which, owing

to the inapplicability of perturbative QCD at long distances, needs to be modelled by phenomenological approaches [41]. The fragmentation of an outgoing high-momentum parton is manifest as a collimated hadronic jet. The vectorial sum of the energy-momentum of the particles within the jet corresponds to the energy of the outgoing parton at the beginning of the hadronisation chain. Jet measurements are therefore an important tool in probing the underlying physics mechanism. There are, however, limitations in the accuracy with which jet properties can reproduce the kinematics of the outgoing partons which gave rise to the jet. For example, detector-related effects such as the non-compensation of the calorimeter and the soft particles which fail to reach the calorimeter, and physics-related effects such as final and initial state radiation which are not included in the jet. Furthermore, an appropriate choice of jet algorithm which is suitable both for experimental and theoretical quantities must also be made [42, 43].

Two algorithms used extensively at ATLAS are the cone and k_T algorithms, with the former employed in this work. The cone algorithm proceeds in the following steps. Each calorimeter energy deposition greater than 2 GeV is considered as a seed. Taking a cone of size $\Delta R = \sqrt{(\eta_i - \eta_{seed})^2 - (\phi_i - \phi_{seed})^2} = 0.7$, a proto-jet is then defined around the seed by summing the energy depositions. Should the jet direction fail to coincide with the seed cell, then a reiteration takes place with the seed cell replaced by the current jet direction until a stable system of jets is obtained. For momentum addition, the so-called E- or 4-vector recombination scheme is used in which 4-vector quantities are used instead of scalar ones. To remove overlap between jets, the proto-jets are either merged or split in the last step, with the merging occurring if two jets share more than 50% of the energy of the jet with the lowest energy. Only jets with a minimum energy of 10 GeV are kept.

For this work, a sample of about 1 million dijet events, simulated using the PYTHIA [44] event generator was used. The events correspond to 2-to-2 leading order QCD processes in which all quark flavours but top were considered. The minimum and maximum values of matrix element transverse momentum cut-off used by PYTHIA are shown in Table 7, respectively. When reconstructing physics objects from these samples, jets were formed by using the cone algorithm on the uncalibrated clusters to obtain the electromagnetic scale jets. The locally calibrated jets were reconstructed by using the cone algorithm with the locally calibrated clusters as input. For the global calibration, jets were formed on uncalibrated towers, then global calibration factor were applied. This was done using ATHENA 12.0.6. The cone algorithm was used both with $\Delta R = 0.7$ and 0.4 respectively, as the size cut-off parameter. The results were found to be very similar, so that in the following only the cone algorithm with $\Delta R = 0.7$ is shown and discussed.

6.3 Global calibration

Unlike the modular approach contained within the local hadronic calibration of this work, the global hadronic calibration aims to calibrate jets of hadronic objects from the calorimeters directly to their "true" jet energy. To this end, reconstructed jets are supposed to be weighted such that their energies reflect directly the true jet energy, as obtained by applying the jet algorithm to the system of stable particles given by PYTHIA following the hadronisation step. In this ap-

Data sample	**Number of events**	p_T^{min} [GeV]	p_T^{max} [GeV]
trig1_misal1_csc11.005009.J0_pythia_jetjet.v12000604	40000	10	17
trig1_misal1_csc11_V1.005011.J2_pythia_jetjet.v12000604	25000	35	70
trig1_misal1_csc11.005012.J3_pythia_jetjet.v12000604	60000	70	140
trig1_misal1_csc11.005013.J4_pythia_jetjet.v12000605	112000	140	280
trig1_misal1_csc11_V1.005014.J5_pythia_jetjet.v12000604	390000	280	560
trig1_misal1_csc11_V2.005015.J6_pythia_jetjet.v12000604	250000	560	1120
trig1_misal1_csc11.005016.J7_pythia_jetjet.v12000604	175000	1120	2280

Table 7: Simulated jet samples used for testing the weights – they are free of any known problems concerning generation and simulation, apart from problems in the forward calorimeters, which will be explained later. The samples were generated with a minimum value on the p_T associated with the matrix element, also given in the table. The events in the samples were added, using a weight of 1 for each event. Due to instabilities during data access, the number of files processed for cluster and cone method differ by a factor of about two, however the statistics are large enough to get valid results for each of the methods and compare them.

proach, the detector and physics are thus inherently intertwined and their systematics cannot be unfolded. While there are advantages and disadvantages to each approach it is important to note that both methods will be a necessary complement to each other when collision data are taken at the LHC. Furthermore, it should be emphasised that the relative performance of each method on simulated data in the pre-LHC era is not necessarily a guide to the accuracy with which each method will perform in the luminosity era in which imperfections in the detection simulation may affect the two methods to different degrees.

In order to obtain the global weights, first the energy sum E_{sum} of all the calorimeter cells in bins of energy density is calculated for each sampling layer[9)]. A global polynomial fit of the form $w_i = a + bE_{sum} + cE_{sum}^2$ is then performed with minimising the χ^2 function,

$$\chi^2 = \Sigma_i \left(\left(\frac{w_i E_{\text{reco}}^{\text{i,jet}}}{E_{\text{true}}^{\text{i,jet}}} \right) - 1 \right)^2 \tag{11}$$

where the index i runs over all cells and the association between the reconstructed and the corresponding true jet is made using their spatial distance $\Delta R = \sqrt{\Delta\phi^2 + \Delta\eta^2}$. The weights are restricted to the range $1 < w < 2$. In addition, the jets are required to have $E_T > 20$ GeV [45,46].

6.4 Estimation of performance: linearity and resolution of jet samples

The performance of the two hadronic calibration methods can be compared by studying the linearity and the resolution of the jet energy scale.

Linearity refers to the requirement that the energy attributed to a reconstructed jet should

[9)] In order to reduce the number of weighting bins and to simplify the weighting procedure, some of the sampling layers are combined and treated as one.

always equal the incident energy of the "true" jet within a few percent, whilst being independent of energy or impact position. A reliable calibration method should give an accurate estimate of the jet energy over the whole energy and η range. To measure the linearity, the ratio of the reconstructed jet energy to the "true" jet energy is determined in intervals of the energy and η of the truth jet. The linearity is then estimated using the mean μ of the distributions $E^{\text{jet}}_{\text{reco}}/E^{\text{jet}}_{\text{truth}}$ as determined by a Gaussian fit, which is constrained within 2 σ of the fit parameters of a first Gaussian fit to the full distribution in each bin. The resolution is taken to be σ/μ, of the same distribution, again determined using the Gaussian fit constrained to 2 σ of the distribution in order to sample only the core of the events and not to be dominated by tails. In addition, only η and energy ranges were considered with more than 50 matched jets, so that the linearity and resolution could be determined on a solid statistical basis. Example distributions in the low, mid and high energy range for low, mid and high values of η are shown in Figures 54 and 55. Numerical values are summarised in Table 8. They prove that using Gaussian fits it a reasonable assumption, even though there are some tails visible. The errors on the Gaussian fits will be used later to determine the uncertainty of the linearities and resolutions derived.

The resolution has an energy dependence that can be expressed as

$$\frac{\sigma(E)}{E} = \sqrt{\frac{a^2}{E} + b^2} = \frac{a}{\sqrt{E}} \oplus b \tag{12}$$

The individual terms can be attributed to sampling and statistical fluctuations (a^2/E), which are dominating over most of the useful range of calorimeters and effects coming from calibration errors, non-uniformities and non-linearities (b), e.g. inherent sampling fluctuations depending on the impact point of the incident particle [17]. The latter limits the performance at very high energies. At ATLAS, the ultimate goal is to achieve a flat linearity with a deviation of at most 2% up to an energy of 4 TeV. For the resolution, the aim is to achieve a resolution of $\frac{\sigma(E)}{E} = \frac{50\%}{\sqrt{E}} \oplus 3\%$ for $|\eta| < 3$ [1].

The linearity and resolution of the methods were compared under the following conditions. The reconstructed jets were matched to the truth jets, by requiring their spatial distance to be less than $\Delta R = \sqrt{\Delta\phi^2 + \Delta\eta^2} < 0.2$. The calibration performance was studied in intervals of $|\eta|$ defined by the limits 0.0, 0.2, 0.4, 0.5, 0.7, 0.9, 1.1, 1.3, 1.5, 1.7,1.9, 2.1, 2.3, 2.45, 2.55, 2.8, 3.0, 3.2, 3.5, 3.95, 4.05. The energy bins cover 25, 31, 39, 48, 59, 72, 88, 107, 130, 158, 191, 231, 279, 336, 405, 488, 587, 706, 849, 1020, 1226, 1473, 1769, 2124, 2550, 3062 GeV, which corresponds to a spacing in energy of two σ in the energy resolution, where the form of the initial resolution is assumed to have a sampling term of 32% and a constant term of 0.1. There was a minimum E_T cut applied on the reconstructed jets of 10 GeV as well as on the truth jets of 20 GeV. In case this cut was dropped, there was an overestimation observed for lower energies for higher values of η, especially for the globally calibrated jets. As the calibration weights for the global method were obtained on a sample with minimal E_T of 20 GeV, reconstructed jets that originate from truth jets with a transverse energy lower than 20 GeV are assumed to have fluctuated very low down in energy and receive therefore a very high jet calibration weight. This results in the observed overestimation of the reconstructed jet energies at low energies. Cuts on the reconstructed jet energy will have to be studied in order to find out the range of validity for the global calibration before data taking, in order to ensure that this overestimation will not lead

Calibration	Energy range of E^{jet}_{true} (GeV)	Number of jets	mean μ	sigma σ	χ^2/NDF
$0.4 < \eta < 0.5$					
EM scale jets	$59 < E < 72$	614	0.637 ± 0.004	0.087 ± 0.005	8.81 / 7
	$279 < E < 336$	579	0.727 ± 0.003	0.054 ± 0.003	9.13 / 4
	$1020 < E < 1226$	288	0.782 ± 0.003	0.042 ± 0.002	0.37 / 3
Global method	$59 < E < 72$	618	0.982 ± 0.005	0.100 ± 0.005	10.34 / 9
	$279 < E < 336$	582	0.997 ± 0.003	0.053 ± 0.002	1.16 / 4
	$1020 < E < 1226$	288	0.992 ± 0.002	0.032 ± 0.002	0.03 / 1
Local method	$59 < E < 72$	2526	0.860 ± 0.003	0.108 ± 0.003	29.08 / 10
(cluster)	$279 < E < 336$	1898	0.936 ± 0.001	0.058 ± 0.001	14.82 / 5
	$1020 < E < 1226$	2766	0.967 ± 0.001	0.042 ± 0.001	8.61 / 2
Local method	$59 < E < 72$	611	0.877 ± 0.004	0.091 ± 0.004	17.91 / 9
(cone)	$279 < E < 336$	575	0.951 ± 0.003	0.057 ± 0.003	9.85 / 4
	$1020 < E < 1226$	289	0.992 ± 0.002	0.028 ± 0.002	0.30 / 1
$2.45 < \eta < 2.55$					
EM scale jets	$279 < E < 336$	364	0.733 ± 0.005	0.078 ± 0.005	3.49 / 7
	$1020 < E < 1226$	266	0.790 ± 0.004	0.045 ± 0.004	1.13 / 2
Global method	$279 < E < 336$	380	1.002 ± 0.005	0.080 ± 0.005	11.49 / 7
	$1020 < E < 1226$	266	1.003 ± 0.003	0.039 ± 0.003	5.69 / 3
Local method	$279 < E < 336$	1659	0.944 ± 0.002	0.082 ± 0.002	19.22 / 8
(cluster)	$1020 < E < 1226$	456	0.950 ± 0.002	0.040 ± 0.002	5.52 / 2
Local method	$279 < E < 336$	371	0.979 ± 0.006	0.097 ± 0.007	5.63 / 8
(cone)	$1020 < E < 1226$	266	0.975 ± 0.002	0.032 ± 0.002	0.94 / 1
$3.95 < \eta < 4.05$					
EM scale jets	$1020 < E < 1226$	597	0.737 ± 0.003	0.056 ± 0.003	5.61 / 4
Global method	$1020 < E < 1226$	599	1.009 ± 0.003	0.054 ± 0.003	8.96 / 4
Local method (cluster)	$1020 < E < 1226$	2331	0.905 ± 0.002	0.072 ± 0.002	23.05 / 5
Local method (cone)	$1020 < E < 1226$	597	0.942 ± 0.003	0.053 ± 0.002	6.03 / 4

Table 8: Parameters of the Gaussian fits for globally and locally calibrated jets (cone method) each reconstructed with a cone parameter of $\Delta R = 0.7$ for various kinematic regions.

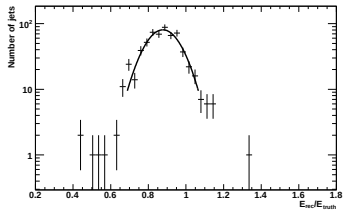

(a) $59 < E_{true}^{jet} < 72$ GeV
$0.4 < \eta < 0.5$

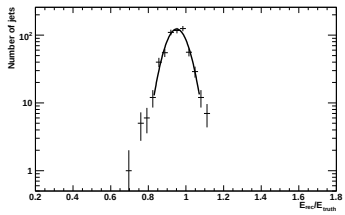

(b) $279 < E_{true}^{jet} < 336$ GeV
$0.4 < \eta < 0.5$

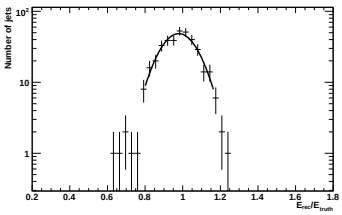

(c) $279 < E_{true}^{jet} < 336$ GeV
$2.45 < \eta < 2.55$

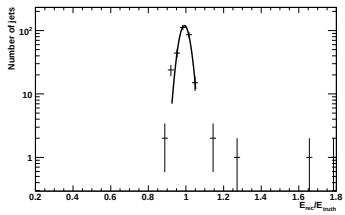

(d) $1020 < E_{true}^{jet} < 1226$ GeV
$0.4 < \eta < 0.5$

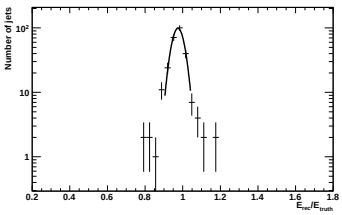

(e) $1020 < E_{true}^{jet} < 1226$ GeV
$2.45 < \eta < 2.55$

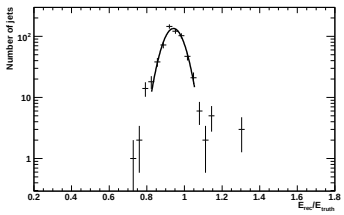

(f) $1020 < E_{true}^{jet} < 1226$ GeV
$3.5 < \eta < 3.95$

Figure 54: Distributions from which linearity and resolution are derived using Gaussian fits for locally calibrated jets (cone method) reconstructed with a cone parameter of $\Delta R = 0.7$. In order to avoid sensitivity to tails, the Gaussian was restricted to lie within 2σ of an initial Gaussian fit to the distribution.

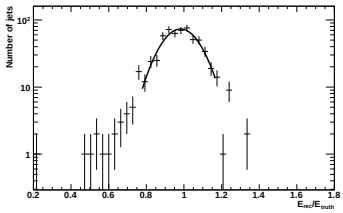

(a) $59 < E_{true}^{jet} < 72$ GeV
$0.4 < \eta < 0.5$

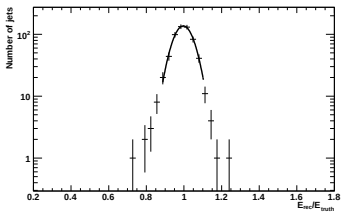

(b) $279 < E_{true}^{jet} < 336$ GeV
$0.4 < \eta < 0.5$

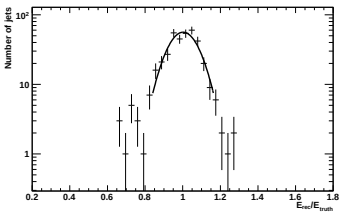

(c) $279 < E_{true}^{jet} < 336$ GeV
$2.45 < \eta < 2.55$

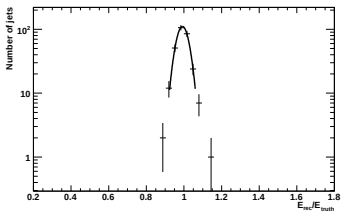

(d) $1020 < E_{true}^{jet} < 1226$ GeV
$0.4 < \eta < 0.5$

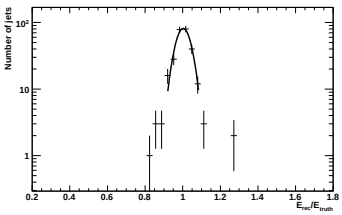

(e) $1020 < E_{true}^{jet} < 1226$ GeV
$2.45 < \eta < 2.55$

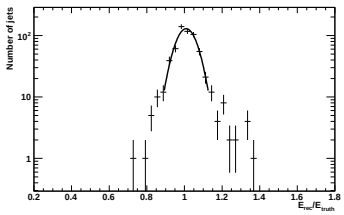

(f) $1020 < E_{true}^{jet} < 1226$ GeV
$3.5 < \eta < 3.95$

Figure 55: Distributions from which linearity and resolution are derived using Gaussian fits for globally calibrated jets reconstructed with a cone parameter of $\Delta R = 0.7$. In order to avoid sensitivity to tails, the Gaussian was restricted to lie within 2σ of an initial Gaussian fit to the distribution.

to any biases in early data taking.

6.4.1 Linearity

Figure 56 shows the behaviour of E_{rec}/E_{truth} as a function of the true jet energy for different intervals of η corresponding to different sub-detector regions: the central barrel region, $0.4 < \eta < 0.5$; the endcap region, $2.45 < \eta < 2.55$; the forward region, $3.5 < \eta < 3.95$. While jets of all energies end up in the barrel part of the detector, the minimum jet energy that can be observed increases with η. The linearity is shown for jets, which were obtained from uncalibrated clusters, i.e. the energy values still correspond to the electromagnetic scale. Also shown are spectra for which the jets were calibrated using the global calibration method as well as jets formed from cells calibrated with the local calibration approach using the cone as well as the cluster methods. Two variations of the cone method were employed: The first uses the angular distance in θ to form the cone (angle), the second uses the distance ΔR in ϕ-η space. While the first was used to obtain the weights and in the weighting procedure, the second was only used when applying the weights as a cross check, as input only the J6 samples was used and the results are only shown for the linearity plots in order to discuss the effect of the different cone making scheme. In Table 9, the mean values of the E_{rec}/E_{truth} ratios for the various η regions and calibration methods are given.

Calibration approach	const. fit $\pm \frac{\text{max}-\text{min}}{2}$	mean $\pm$ RMS
$0.4 < \eta < 0.5$		
EM scale jets	73.5 ± 11.7	70.4 ± 7.3
Global Method	99.3 ± 3.0	98.5 ± 1.7
Local method (cluster)	95.4 ± 8.4	90.9 ± 5.2
Local method (cone, angle)	96.3 ± 10.9	92.2 ± 6.2
Local method (cone, ΔR)	97.1 ± 8.2	91.4 ± 5.5
$2.45 < \eta < 2.55$		
EM scale jets	77.2 ± 5.3	76.4 ± 3.5
Global Method	100.2 ± 2.1	99.9 ± 1.0
Local method (cluster)	94.3 ± 1.1	94.2 ± 0.5
Local method (cone, angle)	97.0 ± 1.2	97.1 ± 0.8
Local method (cone, ΔR)	94.0 ± 1.7	94.1 ± 0.9
$3.95 < \eta < 4.05$		
EM scale jets	71.8 ± 5.0	72.0 ± 3.3
Global Method	100.2 ± 1.3	100.1 ± 0.8
Local method (cluster)	89.4 ± 2.2	89.0 ± 1.5
Local method (cone, angle)	92.8 ± 1.4	92.6 ± 0.8
Local method (cone, ΔR)	88.0 ± 1.3	87.9 ± 0.9

Table 9: Average linearities and their spreads for the different methods (applied to $\Delta R = 0.7$ jets), determined using a constant fit with the spread given as half of the difference between the maximum and the minimum values of E_{rec}/E_{truth}, i.e. $\pm\frac{\text{max}-\text{min}}{2}$. Alternatively the average linearity is given as the mean along the x-axis and the spread is taken to be the RMS along x.

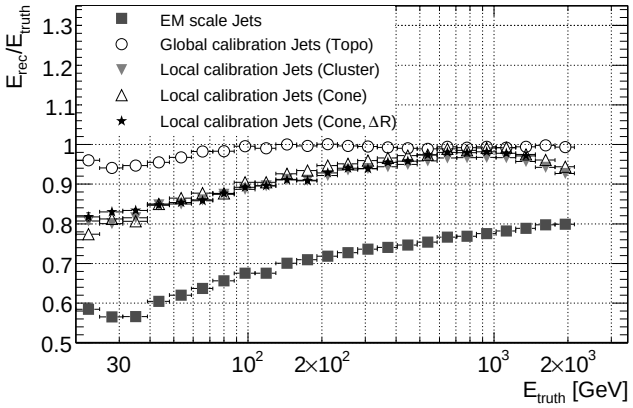

(a) $\frac{E_{rec}}{E_{truth}}$ as a function of true jets energy in the central barrel region, $0.4 < \eta < 0.5$

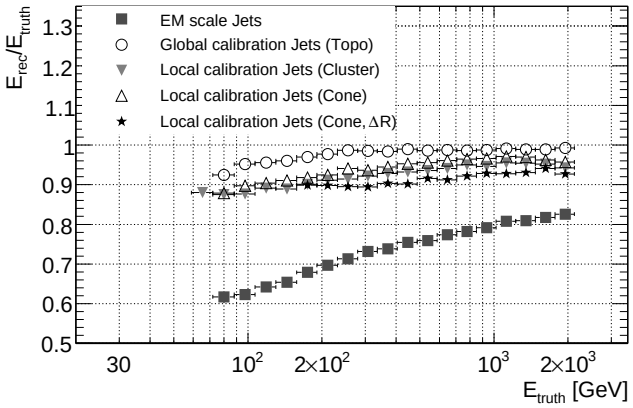

(b) $\frac{E_{rec}}{E_{truth}}$ as a function of true jets energy in the endcap region, $2.45 < \eta < 2.55$

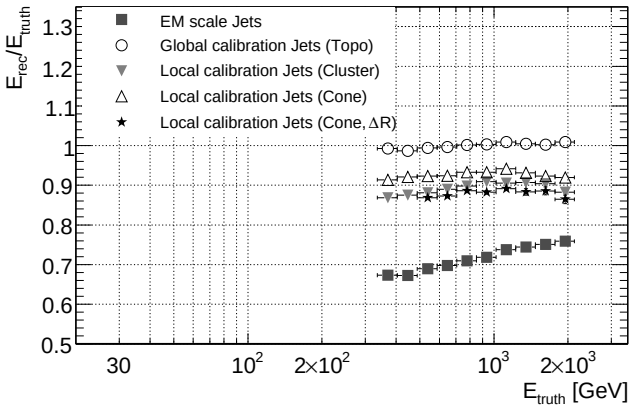

(c) $\frac{E_{rec}}{E_{truth}}$ as a function of true jets energy in the forward region, $3.5 < \eta < 3.95$

Figure 56: Linearity in different η-regions of the detector. Results are shown for jets calibrated on the electromagnetic scale, and for global and local (cone and cluster) calibration methods for cone jets with $\Delta R = 0.7$.

In the central region the electromagnetic scale jets possess values of E_{rec}/E_{truth} of around 55% for the very low energies, while this rises to just below 80% for the highest energies. The local hadronic calibration methods are very similar, and show the same feature as the electromagnetic scale jets concerning the linearity. However, the spread of values of E_{rec}/E_{truth} is not 25% as in the case of the electromagnetic scale jets, but only 20%. The large spread and still quite large deviation from 100% for the central region is due the missing out-of-jet corrections, which are estimated to be most severe for low energy jets, based on the momentum distributions of charged particles inside jets [40]. Furthermore, it is pertinent to note that values of E_{rec}/E_{truth} for the lower energies are around 80% and for the higher energies these are around 100%, showing that the full energy can be recovered at the highest energies, where out-of-jet corrections are smallest as the jets are highly collimated and only very little energy is leaking out of the jet-cone. The global method performs best and is flat over the whole energy range within a range of about $\pm 1\%$ when the lowest and highest energy bin are excluded. It should be noted that the local hadron calibration reaches a linearity of just above 90% for a true jet energy between 140 and 280 GeV, which is comparable with the estimates described in Section 6.1.

For the endcap region, again the global method performs the best. The linearity is restored within about $\pm 2\%$. The linearity of the local hadronic calibration methods is much flatter than in the central region, with a spread of about $\pm$2-4%. However, the linearity is restored only up to about 95%. The cone methods (angle scheme) seems to perform slightly better than the other two methods, but this is a very slight effect and strongly depends on the cuts used – it was not observed when using different cuts on the jet algorithms and on the minimum E_T of the jets. Again, the missing 5% until full linearity are believed to be due to missing jet energy corrections. The electromagnetic scale jets exhibit a value of E_{rec}/E_{truth} of just below 70%, which increases to 80% for the highest energies. The energy of the very forward jets is again well described by the global calibration method. While it restores the linearity fully, the local calibration method only restores the energy to 90%. The spread however is comparable for all methods and lies around $\pm$1-2%. For the very high energies predominant for jets in the forward region a much better performance would have been expected for the local methods, as the geniune jet corrections should be quite small in this region of phase space. However, there is a problem with the simulation of the FCAL, which leaves the electromagnetic scale being $\sim$12% too low [39, 47]. Thus, the jets local calibrated jets must be inherently worse in that region compared to other regions, because they start from a wrong scale. This effect will show up again in the next paragraph, when plotting the linearity versus η.

When looking at the linearity for different energy ranges, namely for low jet energies, $59 < E^{jet}_{true} < 72$ GeV, for mid jet energies, $279 < E^{jet}_{true} < 336$ GeV and for high jet energies, $1020 < E^{jet}_{true} < 1226$ GeV, the same features can be observed, as demonstrated in Figure 57. For the low energy jets, there are no jets observed in the more forward regions beyond $\eta_{truth} = 1.8$, which is due to the minimum E_T cut. The local methods reconstruct jet energies which are lower than the true jet energies, because of the missing out-of-jet corrections and reaches on average 85%. The electromagnetic scale jets display a linearity of only around 60%. As one goes higher up in energy, the performance of the local methods improves to a linearity of about 95% in the central region, the electromagnetic scale jets reach linearities of 70% to 80%. For all calibration algorithms, there is a slight dip in linearity around the crack regions at $\eta_{truth} = 1.5$ and at $\eta_{truth} = 3.2$ visible. Only for the electromagnetic scale jets and the locally

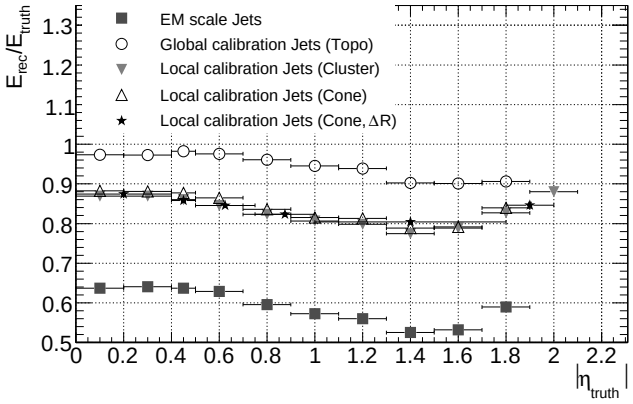

(a) E_{rec}/E_{truth} as a function of true jet η for low jet energies, $59 < E_{true}^{jet} < 72$ GeV

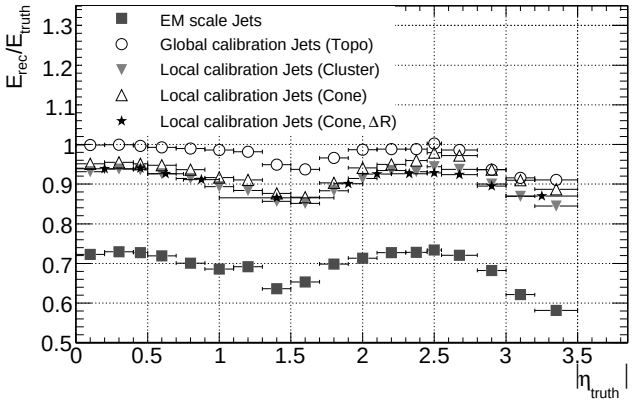

(b) E_{rec}/E_{truth} as a function of true jet η for mid jet energies, $279 < E_{true}^{jet} < 336$ GeV

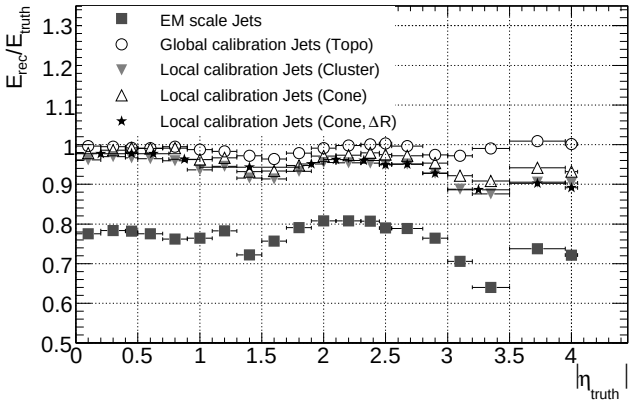

(c) E_{rec}/E_{truth} as a function of true jet η for high jet energies, $1020 < E_{true}^{jet} < 1226$ GeV

Figure 57: Linearity in different energy ranges. Results are shown for jets calibrated on the electromagnetic scale, and for global and local (cone and cluster) calibration methods for cone jets with $\Delta R = 0.7$. The η binning for the locally calibrated jets with the cone-ΔR method is slightly different, however where the binning is the same, the linearities agrees with the other local methods almost exactly.

calibrated jets, there is significant drop in linearity observable for the most forward η regions. This is connected to wrong values used in the simulation for the sampling fractions in the FCAL, which led to a wrongly calibrated electromagnetic scale, giving energies of the order of $\sim$12% too low [39, 47]. This is compatible with what we observe in the electromagnetic scale as well as in the locally calibrated jets. As the global method calibrates for detector effects and physics effects in one step, this behaviour could not be observed, as the calibration factors were derived such that they compensated for the wrong electromagnetic scale unnoticeably.

When comparing the two different methods of local hadronic calibration as well as the different schemes of making the cone, it becomes apparent, that these methods are very similar concerning their performance. Also, applying weights derived for angle-type cones to ΔR-type cones does not change the results dramatically, however slightly deteriorates the performance. It is worthwhile noting, that the difference between the two cone-making schemes grow with η and are largest for the very forward region. This is very much what is expected, as it reflects the increasing differences between angle-type cones and ΔR-type cones as η grows. This is due to the non-linear correlation between $\eta = -\ln\left(\tan\frac{\theta}{2}\right)$ and θ. The differences are still very small at large η, which again indicates the stability of the local hadronic calibration methods. Another positive feature is the ability to uncover flaws in the electromagnetic scale as shown in the FCAL. The application of genuine, energy dependent jet corrections on top of the calorimeter calibration should be able to recover the full energy and make the local calibration methods fully usable for jets.

6.4.2 Resolution

The jet energy resolution, for $\Delta R = 0.7$ jets, is shown in Figure 58 as a function of $1/\sqrt{E_{true}}$ for different intervals of pseudorapidity. As for the linearity study, results are shown for jets calibrated to the electromagnetic scale and jets calibrated with the global and local (cone and cluster) calibration methods. The energy dependence follows the form given in Equation 6.4 and fits to this equation are also shown.

As expected, the resolution is poorest for the EM-scale only calibration over most of the kinematic region studied; the two local methods give similar results. At the higher energy values in the central region the global calibration method clearly delivers the best performance although at low energies the local and global methods give a consistent performance within the statistical precision of this study.

Compared with the barrel region, the global and local calibration are closer at high energies although the global method still shows a tendency towards lower resolution. At higher energy the global method offers a lower resolution.

In the forward region the global method provides the best resolution in the high energy range. The local and EM-scale only methods give a consistent resolution in this region. When comparing the cluster method to the cone method the later seems to perform marginally better, however, the difference are very small and consistent with zero. Again, this indicates the stability of the local hadronic calibration approach in general.

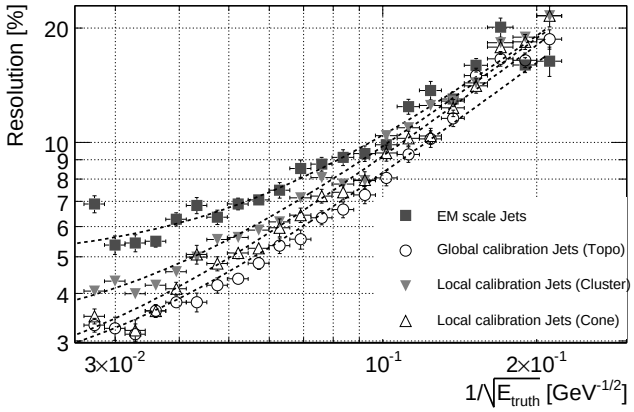

(a) Resolution as a function of $\frac{1}{\sqrt{E_{true}}}$ in the central barrel region, $0.4 < \eta < 0.5$

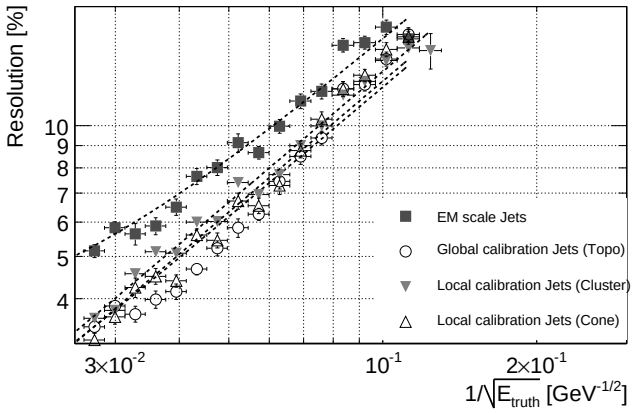

(b) Resolution as a function of $\frac{1}{\sqrt{E_{true}}}$ in the endcap region, $2.45 < \eta < 2.55$

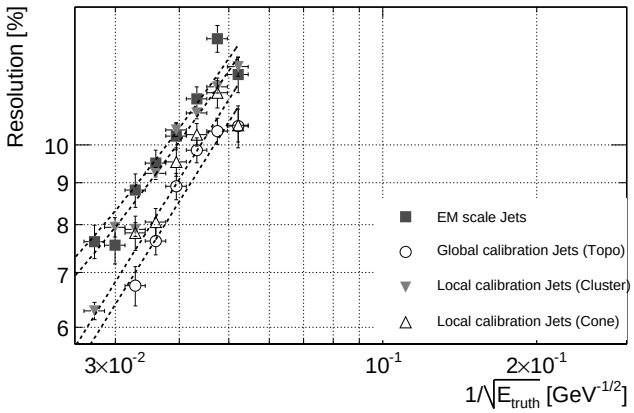

(c) Resolution as a function of $\frac{1}{\sqrt{E_{true}}}$ in the forward region, $3.5 < \eta < 3.95$

Figure 58: Jet resolution in different η-regions of the detector. Results are shown for jets calibrated on the electromagnetic scale, and for global and local (cone and cluster) calibration methods for cone jets with $\Delta R = 0.7$.

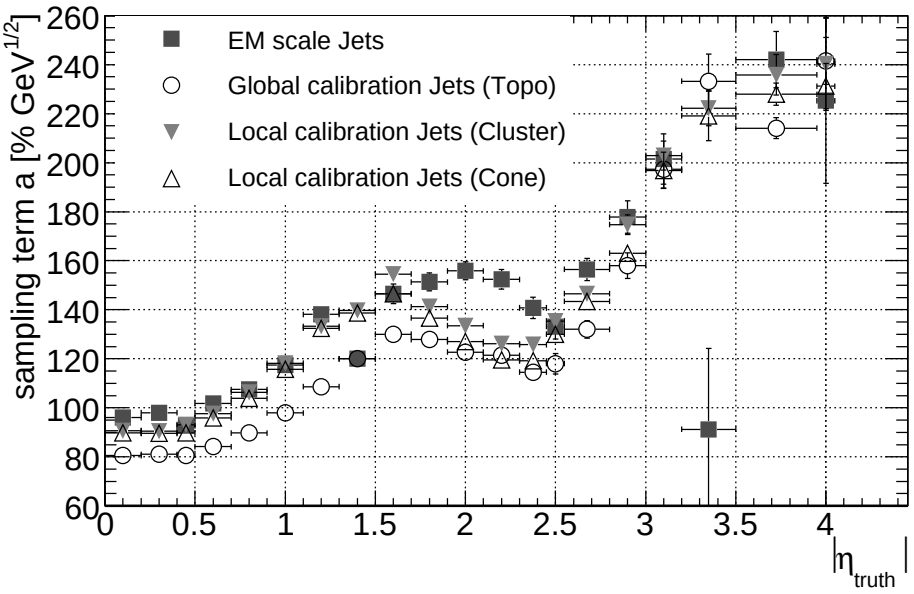

Figure 59: Sampling term a (% GeV$^{1/2}$) as a function of η, for fits to the resolutions of $\Delta R = 0.7$ jets.

The dependence of the sampling term a and the constant term b on jet pseudorapidity is shown in Figure 59 and Figure 60. The value of a grows with pseudorapidity for all calibration approaches, however the relative difference between them changes: In the central barrel region, the EM scale and the locally calibrated jets have approximately the same sampling term and the global method performs better. However, in the end-cap region the locally calibrated jets improve relative to the EM scale jets and have about the same sampling term as the globally calibrated jets. In the very forward region all approaches perform about the same within the errors, which are taken to be the fit errors on the parameters. The constant terms b as obtained from fits to the resolution of the locally and globally calibrated jets lie closer together and have smaller values than the ones obtained for EM scale jets. Going to higher values of η, the differences between local and global methods get smaller[10)]. Values of a and b for $\Delta R = 0.7$ jets in the three sample pseudorapidity intervals are summarised in Table 10 together with χ^2/NDF obtained from the fits.

[10)]The constant term b originates from inherent sampling fluctuations due to the geometry of the detector, therefore it can be reduced by applying calibration.

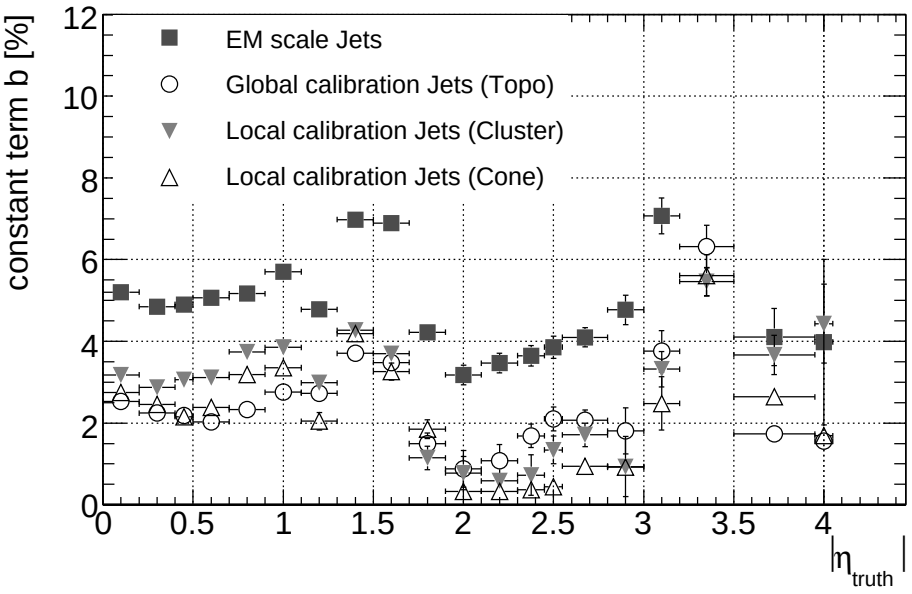

Figure 60: Constant term b (%) as a function of η, for fits to the resolutions of $\Delta R = 0.7$ jets.

Calibration approach	a (% GeV$^{1/2}$)	b (%)	χ^2 / NDF
$0.4 < \eta < 0.5$			
EM scale jets	92.4 ± 2.3	4.9 ± 0.1	48.2 / 22
Global Method	80.3 ± 1.7	2.2 ± 0.1	37.7 / 22
Local method (cluster)	92.8 ± 1.5	3.1 ± 0.1	69.3 / 23
Local method (cone, angle)	89.5 ± 1.9	2.2 ± 0.2	62.5 / 22
$2.45 < \eta < 2.55$			
EM scale jets	132.7 ± 5.1	3.9 ± 0.3	19.3 / 15
Global Method	117.6 ± 4.1	2.1 ± 0.3	23.5 / 15
Local method (cluster)	134.9 ± 3.1	1.3 ± 0.3	25.8 / 15
Local method (cone)	129.6 ± 2.7	0.0 ± 0.4	38.8 / 15
$3.5 < \eta < 3.95$			
EM scale jets	241.2 ± 11.5	4.1 ± 0.7	9.8 / 9
Global Method	213.4 ± 4.3	0.0 ± 1.7	14.1 / 9
Local method (cluster)	235.1 ± 8.2	3.7 ± 0.5	49.7 / 9
Local method (cone)	227.2 ± 4.6	0.0 ± 2.7	17.3 / 9

Table 10: Resolution as function of $1/\sqrt{E_{true}}$ with fits of the form $r = a/\sqrt{E_{true}} \oplus b$ for different regions of η. $\Delta R = 0.7$ jets.

7 Summary and Discussion

For the first time, the local hadronic calibration scheme has been applied to real data from a combined test beam. The performance of the scheme on simulated jets in full ATLAS set-up has also been demonstrated. In this note we have shown that calibration by applying tabulated weighting factors to individual calorimeter cell signals provide a stable method for calorimeter compensation, and that the two versions of the local calibration, the "cone" and the "cluster" methods, give very similar results. The local method achieves calorimeter compensation within 3% for beam energies above ~ 2 GeV, as demonstrated in Section 3.6. In addition, the linearity after weighting and corrections for energy losses in dead material is compatible for combined test beam data and simulation, as shown in Figure 42, Section 4.5. Hadronic scale linearity in the calorimeter within 3% is slightly larger than what is specified in the technical proposal [12], but as mentioned previously, the method has room for improvement, especially in the noise reduction.

Of the two noise reduction techniques described in Section 3.4, the weight restriction $0.6 < w_{cell} < 3$ implemented when filling the weight tables might lead to a bias in the hadronic scale energy, as the cut affects the weights on a level not reproducible on data. The weight restriction cut was shown to be necessary in order to eliminate noise effects, such as the lowering of the weights when the signal is close to the noise threshold. Clearly, a plain noise cut alone does not serve to fully reduce the problems overlaid noise cause. Ideally, we would like to find a set of variables on reconstruction level (i.e. values that are accessible in data) that would provide us with a possibility to perform an additional noise reducing cut. Such studies are important to perform to ensure a bias-free hadronic weighting.

In this note, the main focus has been the hadronic compensation of the calorimeters. However, to demonstrate the performance of the weighting on the combined test beam pion data, a set of cuts and corrections have been applied, as described in Sections 4.2 and 4.4, among them the electron removal cut and the corrections for losses in dead material. Future studies should optimise these corrections. Normally, the inner detector would be used to discriminate between electrons and pions. For jets in ATLAS, the electromagnetic clusters are excluded from weighting using cluster moments as described in Section 6.1 and Ref. [8]. The exclusion of electromagnetic clusters when applying the weights is necessary in order to let the hadronic calibration follow the event-by-event fluctuations in the electromagnetic fraction of the shower energy, and thus improve the resolution of the energy. The corrections of dead material energy losses is a vast subject under study (see for example Ref. [48]).

In Section 4.5, the differences between data and simulation seen in the weight performance was explained by the inability of the simulation to correctly describe the shower development of the data. As all hadronic compensation schemes rely on simulations, the example given here clearly demonstrates the need for a good understanding of the simulations in relation to data. A lot of work is being done in this area, see, for example, Ref. [49].

The application of the local hadron calibration on jet samples was studied and compared with the global calibration method, which calibrates to the level of particle truth jets. As the local method calibrates only to detector level, without applying final and genuine jet corrections,

it fails to reach the high level of linearity and resolution, the global calibration method is able to achieve over a large kinematic region. However, the strength of the local calibration method still become apparent. As it does not calibrate inclusively, but in a modular approach, it is able to reveal problems with the electromagnetic scale calibration in the forward calorimeter. Here, the global calibration proves to be insensitive. For a better and fairer comparison between the global and the local calibration approaches, jet corrections need to be developed for the local calibration methods.

The modular approach of the local calibration might prove to be an important aid when calibrating ATLAS with the first collision data, a period during which any imperfections in the simulation will be exposed. Since detector and physics effects are disentangled when performing the calibration, the local calibration method provides an easier way of finding possible problems in the simulation description of the detector. The systematic uncertainties of the jet energy scale are also easier to evaluate with a modular calibration. For the final calibration of ATLAS, two complementary methods, such as the local and the global methods, are necessary.

A Numerical values of the weight tables

A.1 Weight tables for first LAr sampling layer

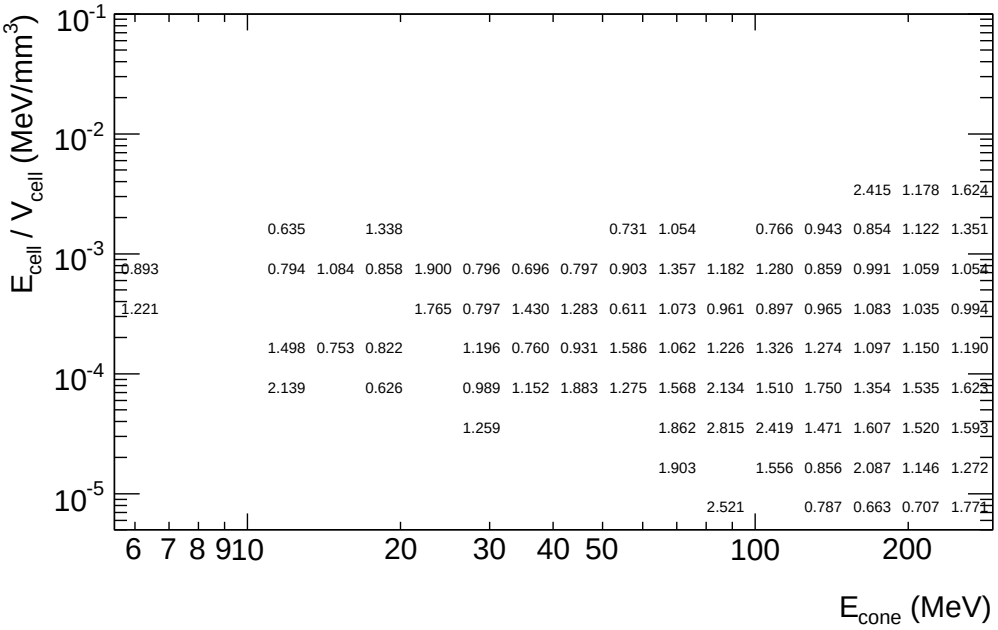

Figure 61: Weight table for LAr first sampling layer (the strips), low E_{cone} values.

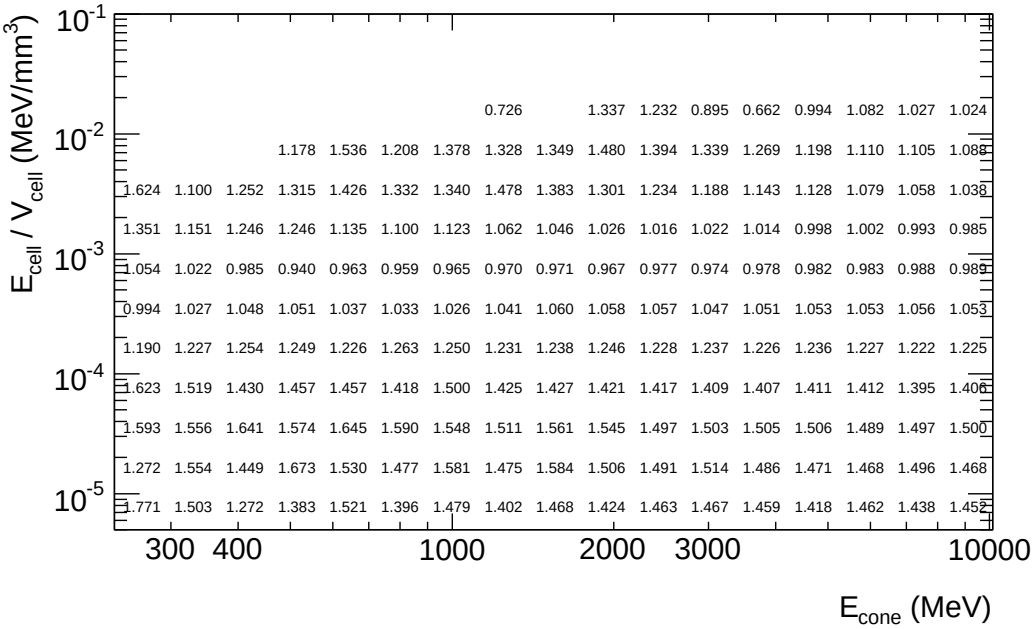

Figure 62: Weight table for LAr first sampling layer (the strips), medium E_{cone} values.

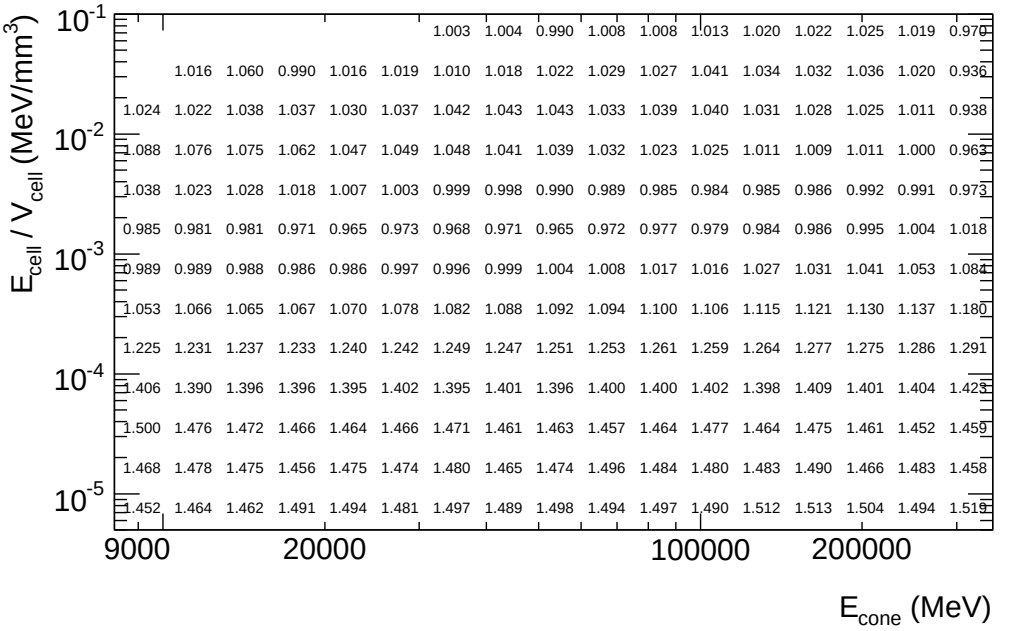

Figure 63: Weight table for LAr first sampling layer (the strips), high E_{cone} values.

A.2 Weight tables for second LAr sampling layer

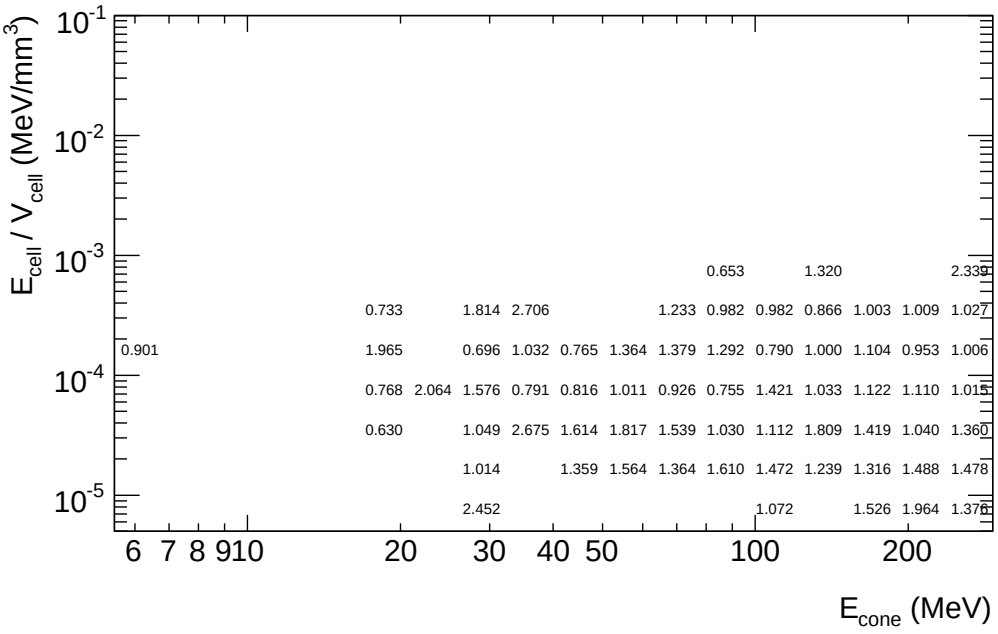

Figure 64: Weight table for LAr second sampling layer (middle), low E_{cone} values.

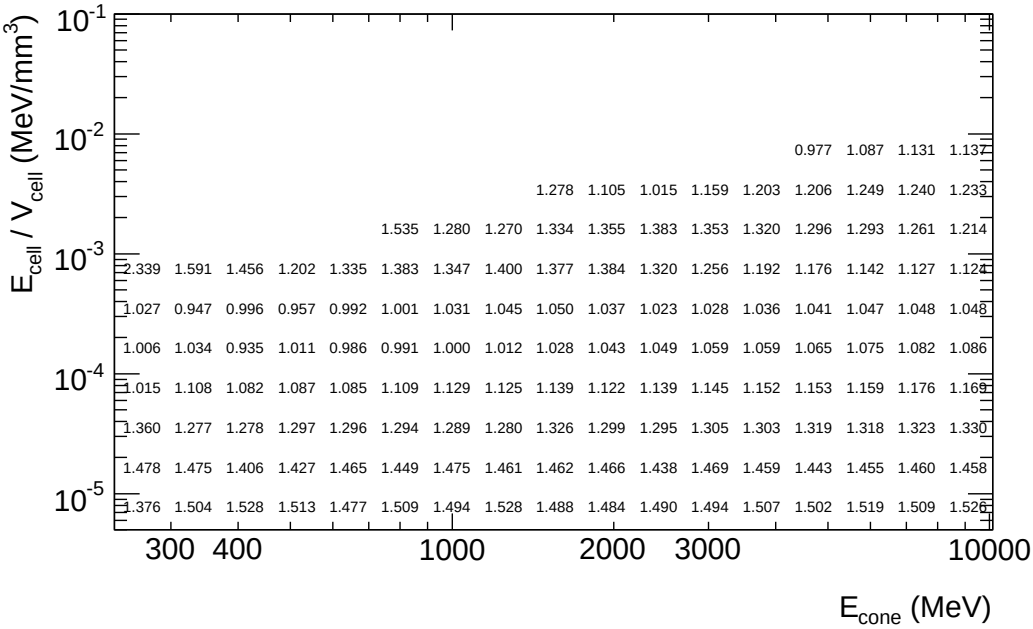

Figure 65: Weight table for LAr second sampling layer (middle), medium E_{cone} values.

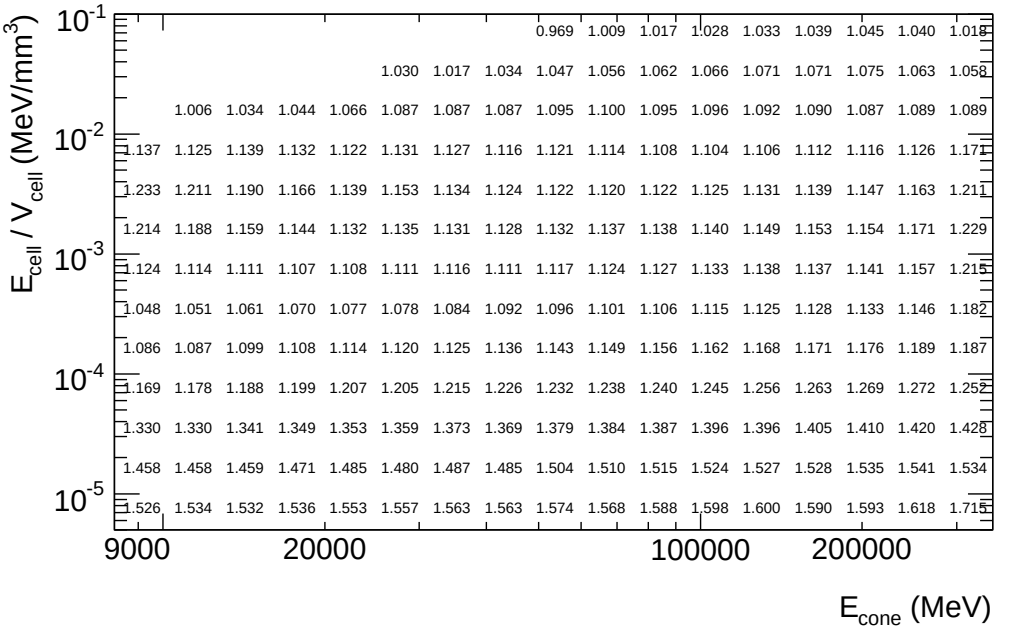

Figure 66: Weight table for LAr second sampling layer (middle), high E_{cone} values.

A.3 Weight tables for third LAr sampling layer

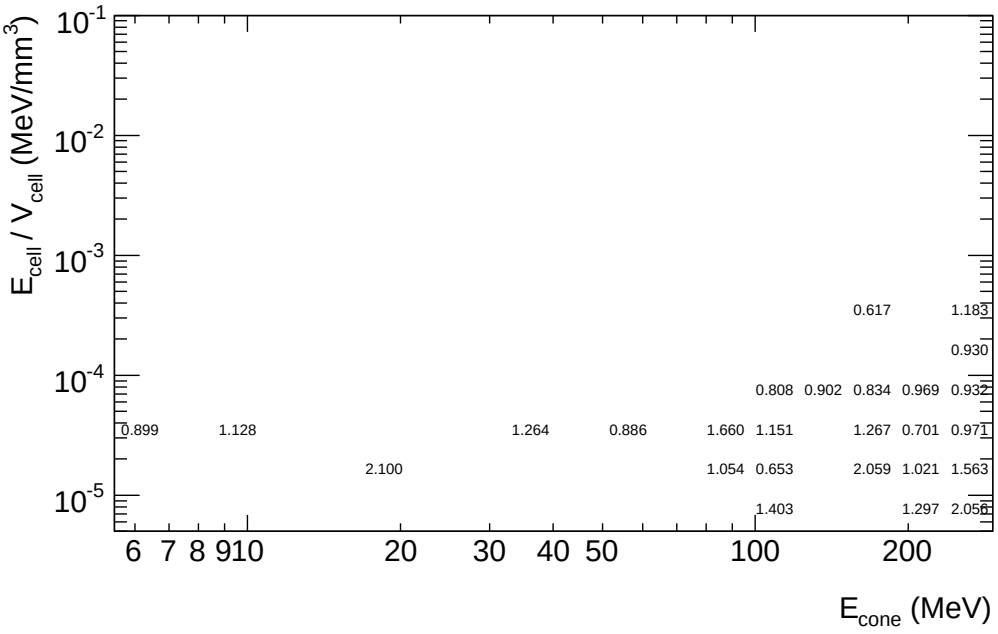

Figure 67: Weight table for LAr third sampling layer (back), low E_{cone} values.

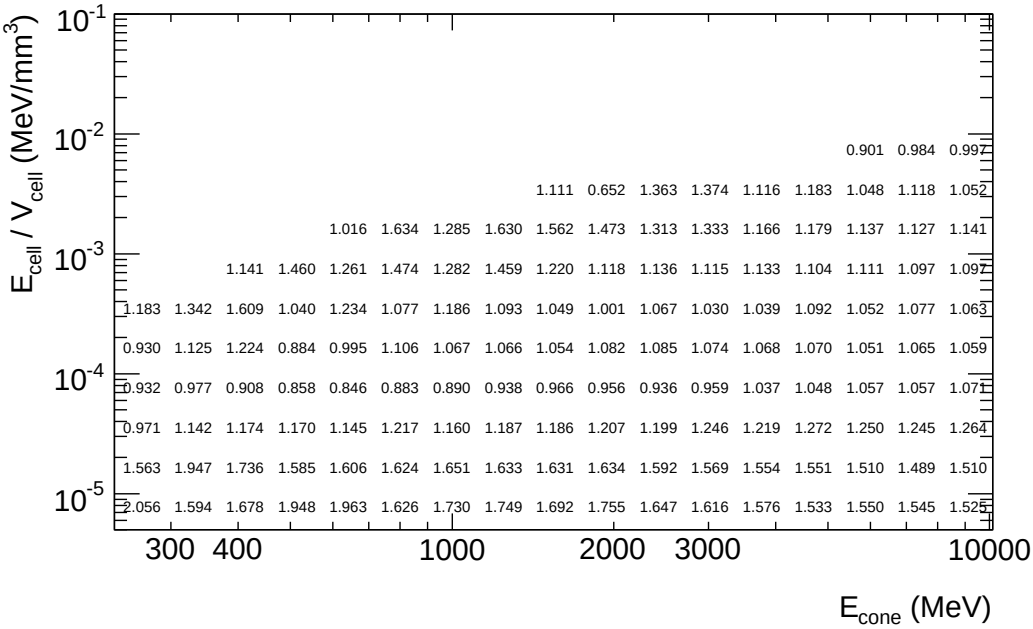

Figure 68: Weight table for LAr third sampling layer (back), medium E_{cone} values.

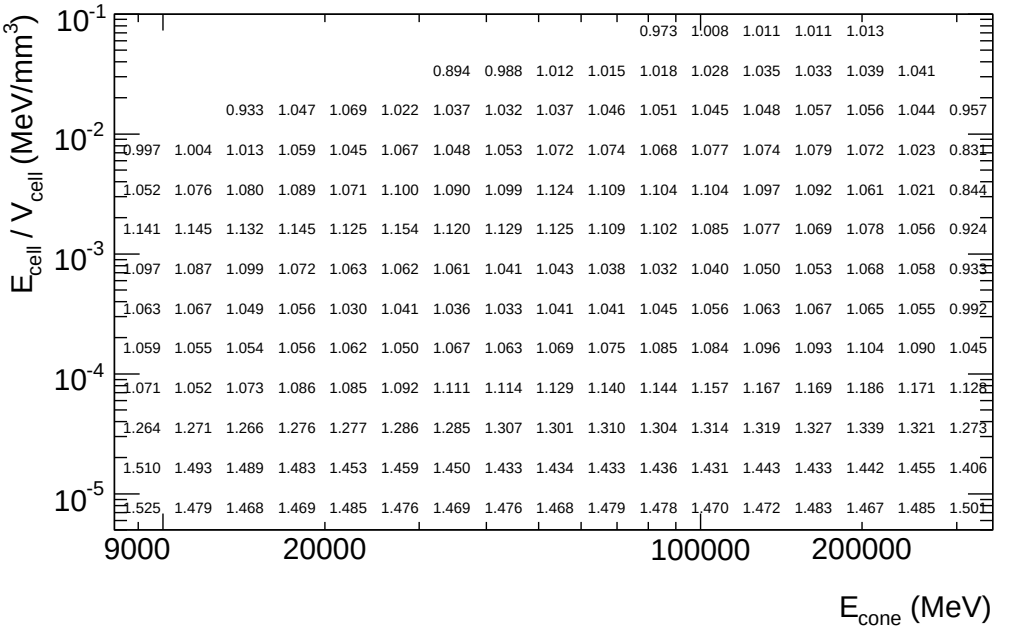

Figure 69: Weight table for LAr third sampling layer (back), high E_{cone} values.

A.4 Weight tables for first Tile sampling layer, the A-cells

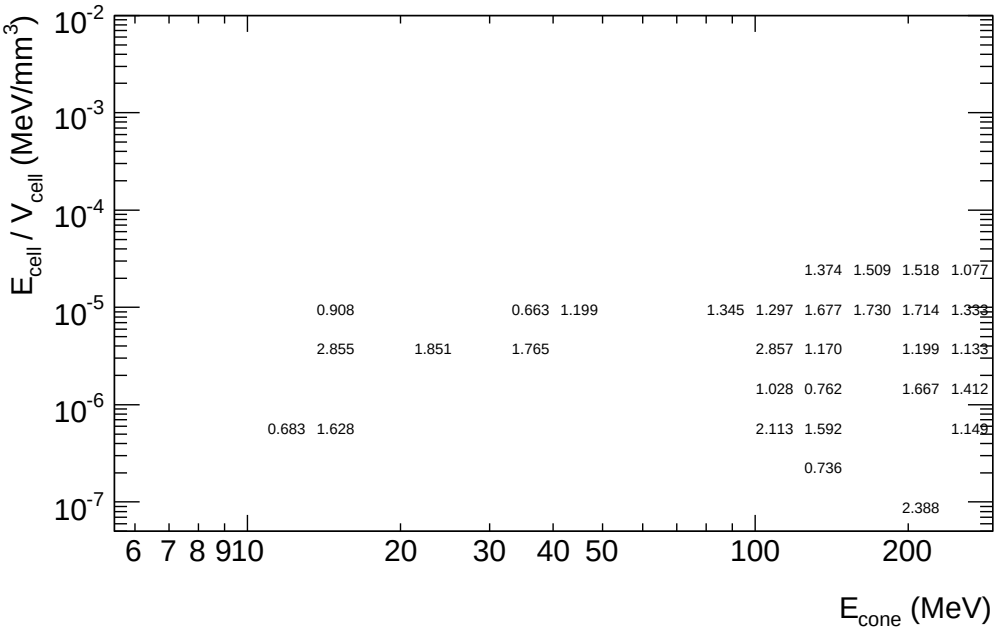

Figure 70: Weight table for Tile first sampling layer (the A-cells), low E_{cone} values.

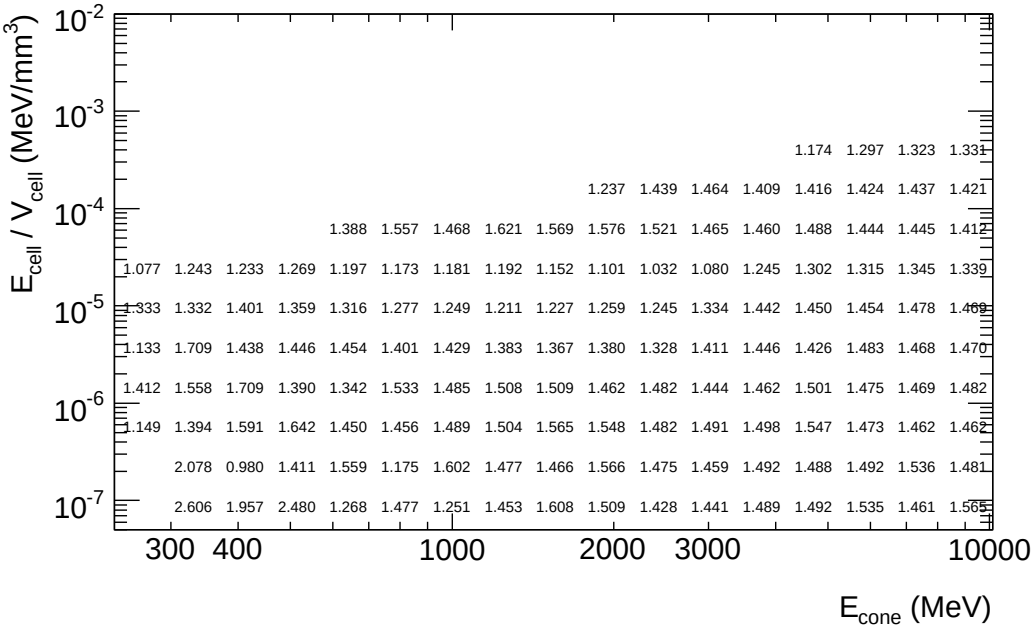

Figure 71: Weight table for Tile first sampling layer (the A-cells), medium E_{cone} values.

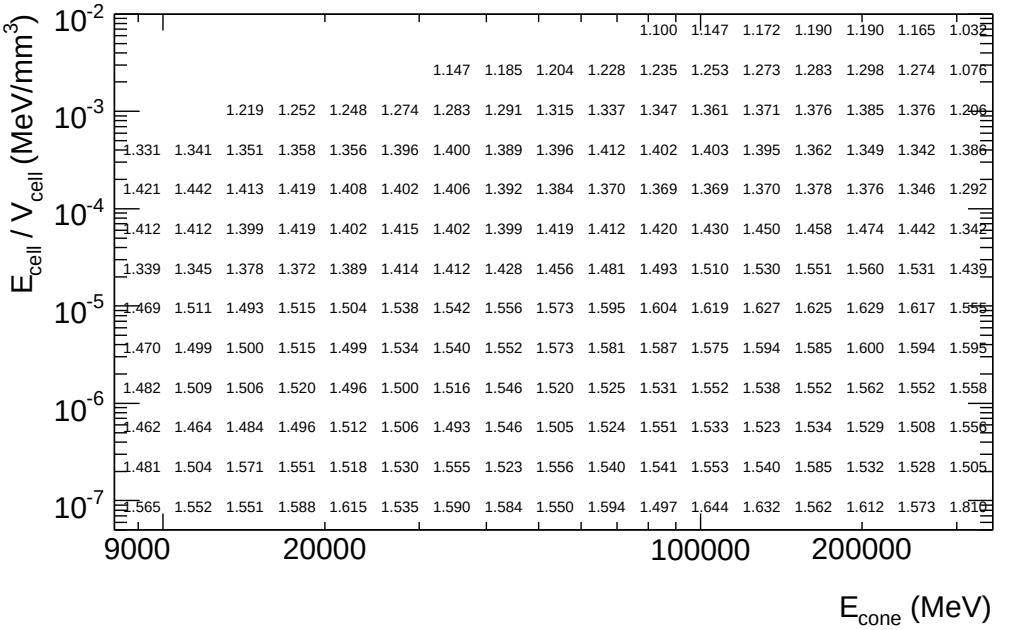

Figure 72: Weight table for Tile first sampling layer (the A-cells), high E_{cone} values.

A.5 Weight tables for second Tile sampling layer, the BC-cells

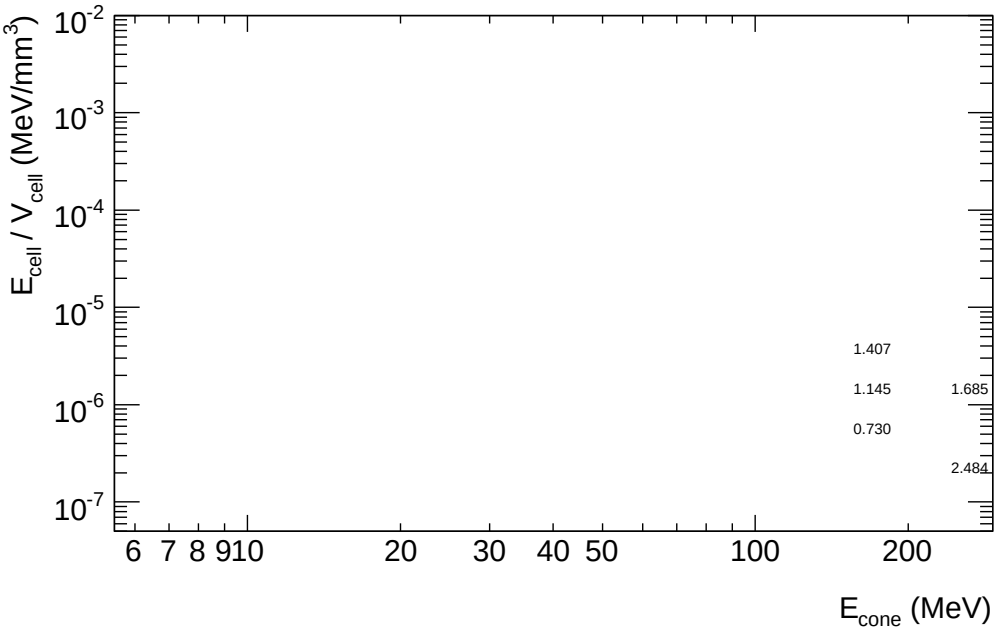

Figure 73: Weight table for Tile second sampling layer (the BC-cells), low E_{cone} values.

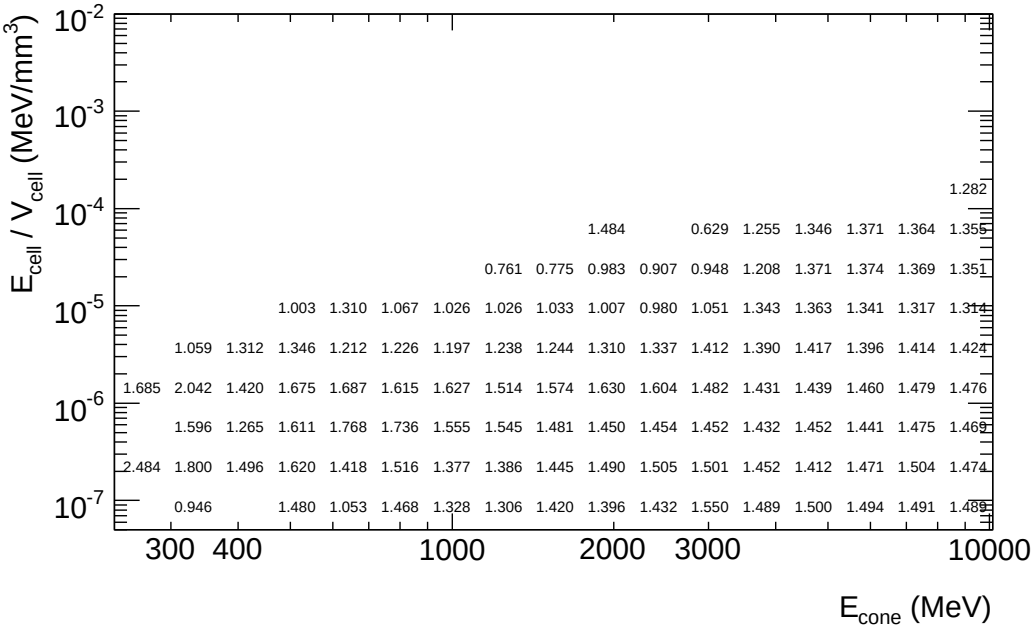

Figure 74: Weight table for Tile second sampling layer (the BC-cells), medium E_{cone} values.

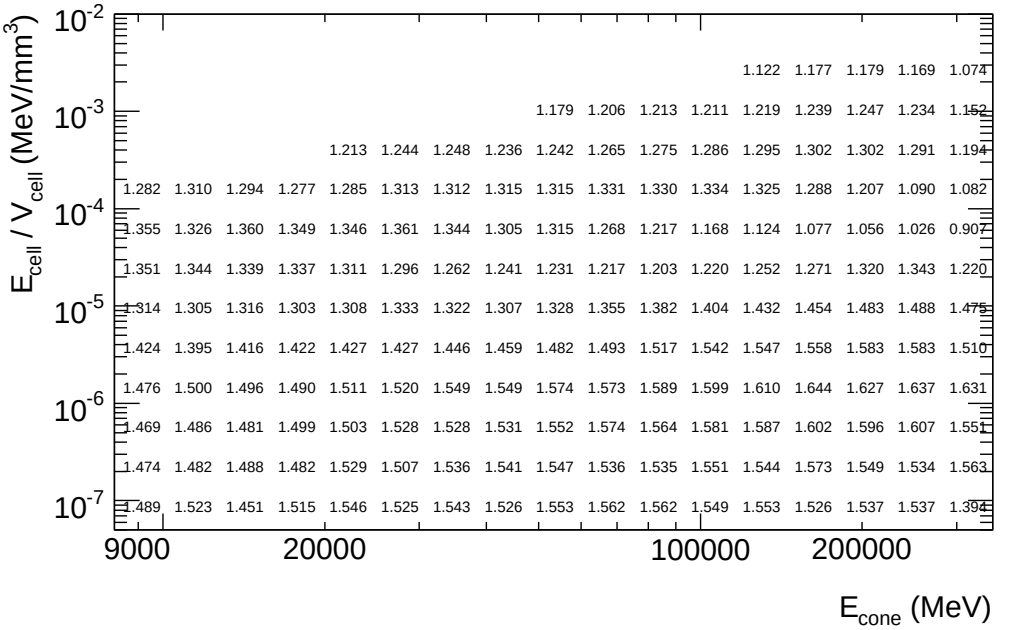

Figure 75: Weight table for Tile second sampling layer (the BC-cells), high E_{cone} values.

A.6 Weight tables for third Tile sampling layer, the D-cells

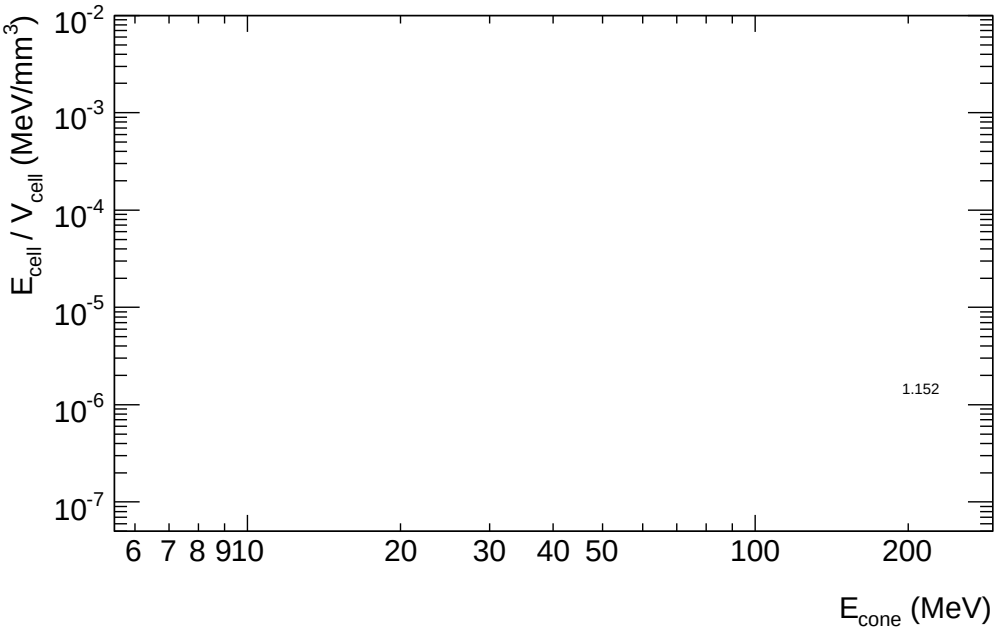

Figure 76: Weight table for Tile third sampling layer (the D-cells), low E_{cone} values.

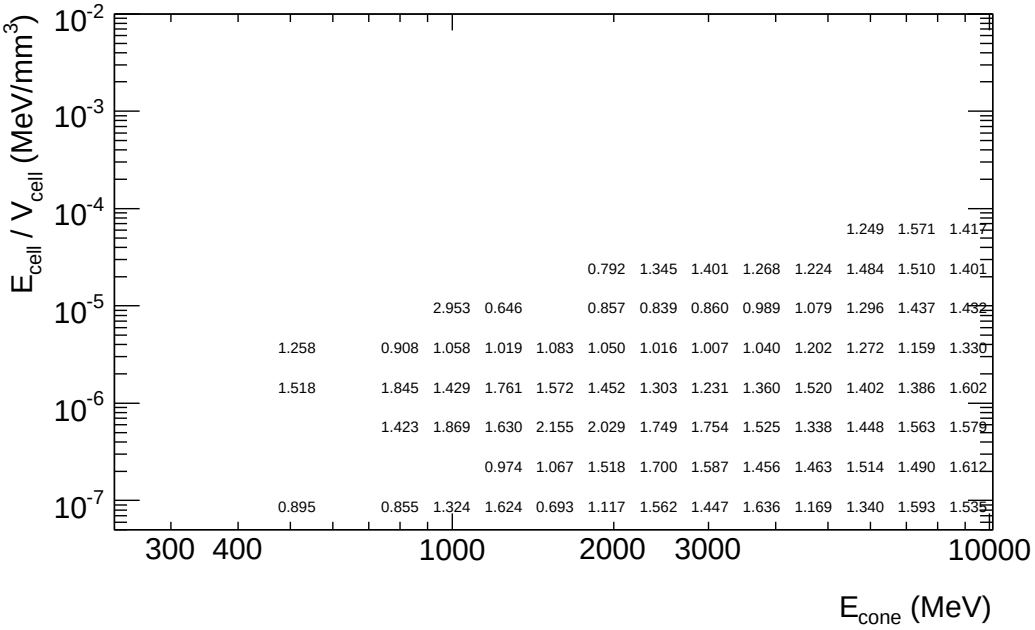

Figure 77: Weight table for Tile third sampling layer (the D-cells), medium E_{cone} values.

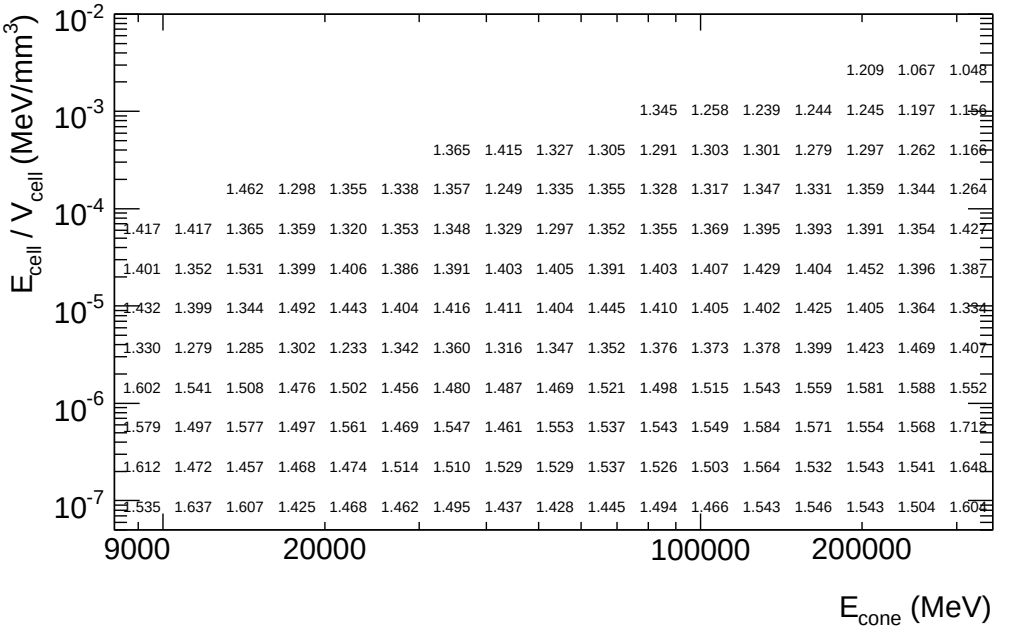

Figure 78: Weight table for Tile third sampling layer (the D-cells), high E_{cone} values.

B Systematic effects of the dead material corrections and electron cut

As described in Section 4.2, the electron removal cut will give a bias to the energy scale, which becomes significant at low energies. In Section 4.4, the corrections for losses in dead material were discussed, and a small bias from the correction factors not being constant with beam energy was demonstrated. In Tables 11-12, the effect of the electron cut and the dead material, when applied to a pure sample of simulated pions is demonstrated. In Tables 13-14, the systematic effect of the electron cut on the unweighted energy signal is given.

E_{beam} (GeV)	Resolution (%)	Stat. error (%)	Syst. err. from DM corr. (%)	Syst. err. from electron cut (%)	Total error (%)
300.00	5.07	0.09	0.30	0.07	0.32
250.00	5.95	0.10	0.05	0.38	0.40
200.00	6.13	0.10	0.33	0.50	0.60
180.00	6.46	0.10	0.14	0.06	0.18
150.00	7.03	0.11	0.34	0.11	0.37
100.00	8.52	0.14	0.13	0.13	0.23
90.00	8.75	0.14	0.35	0.41	0.56
80.00	9.41	0.16	0.04	0.25	0.30
70.00	9.74	0.16	0.18	0.05	0.24
60.00	10.26	0.17	0.12	0.04	0.21
50.00	11.28	0.17	0.16	0.06	0.25
40.00	12.92	0.22	0.16	0.57	0.63
30.00	14.28	0.24	0.60	0.84	1.06
25.00	15.58	0.27	0.19	0.78	0.84
20.00	17.18	0.31	0.00	0.79	0.85
15.00	19.54	0.37	0.36	0.15	0.54
10.00	26.42	0.53	0.63	0.07	0.83
9.00	29.35	0.67	0.31	2.87	2.96
7.00	41.53	1.37	4.64	2.29	5.35
6.00	36.06	0.80	0.55	2.77	2.93
5.00	34.43	0.84	0.25	0.53	1.02
4.00	30.56	0.81	0.01	9.92	9.95
3.00	32.92	1.01	0.45	12.17	12.22
2.00	34.74	1.11	0.65	28.10	28.13
1.50	38.41	1.63	1.84	30.79	30.89
1.00	45.87	2.69	0.37	44.08	44.16
0.75	59.38	5.14	2.33	61.21	61.47
0.50	96.58	19.98	36.22	317.72	320.40

Table 11: Systematic uncertainties in the resolution of the simulated energy signal, after weighting and dead material correction, as a consequence of the electron removal cut and the corrections for losses in dead material.

E_{beam} (GeV)	E_{mean}/E_{beam} (%)	Stat. error (%)	Syst. err. from DM corr. (%)	Syst. err. from electron cut (%)	Total error (%)
300.00	98.28	0.09	0.39	0.14	0.42
250.00	98.61	0.10	0.31	0.06	0.33
200.00	98.39	0.10	0.13	0.08	0.19
180.00	98.33	0.10	0.01	0.10	0.14
150.00	97.90	0.11	0.51	0.03	0.53
100.00	96.89	0.14	0.94	0.42	1.04
90.00	96.48	0.14	0.85	0.14	0.87
80.00	95.93	0.15	1.05	0.37	1.12
70.00	95.29	0.16	0.94	0.01	0.95
60.00	94.58	0.16	1.33	0.60	1.47
50.00	94.44	0.18	1.73	0.09	1.74
40.00	93.48	0.21	1.46	0.84	1.70
30.00	91.57	0.23	1.60	0.45	1.68
25.00	91.25	0.25	2.33	0.21	2.35
20.00	90.00	0.28	2.83	0.25	2.85
15.00	86.78	0.32	1.99	1.63	2.59
10.00	83.25	0.44	3.22	2.85	4.32
9.00	83.90	0.51	3.70	3.80	5.33
7.00	79.11	0.91	1.19	3.49	3.80
6.00	80.26	0.68	2.77	4.15	5.03
5.00	75.72	0.65	0.76	5.35	5.44
4.00	77.62	0.60	2.62	4.95	5.63
3.00	81.43	0.75	2.19	12.76	12.97
2.00	88.94	0.99	7.85	25.97	27.14
1.50	90.58	1.34	7.24	27.55	28.51
1.00	85.64	1.94	13.05	37.68	39.93
0.75	70.05	2.80	6.84	34.38	35.17
0.50	55.67	6.70	4.37	36.35	37.22

Table 12: Systematic uncertainties in the E_{mean}/E_{beam} ratio of the simulated energy signal, after weighting and dead material correction, as a consequence of the electron removal cut and the corrections for losses in dead material.

The statistical errors are given from the Gaussian fit to the energy distribution of the weighted and dead material corrected energy. The systematical uncertainties have been estimated using two independent samples of the simulated energy: one containing the events with odd event number (sample A), and one containing the even event numbers (sample B). The uncertainty is estimated as the difference

$$\Delta_{syst} = r_{A,\ corrected} - r_{B,\ uncorrected} \tag{13}$$

where r is either the resolution or the ratio E_{mean}/E_{beam}, indices A and B refer to quantities computed from the odd or even event number samples respectively, *corrected* refers to the quantity after the electron cut and dead material correction using one correction constant per

region and *uncorrected* means that no electron cut was applied or the dead material corrections using beam energy dependent factors were used.

The systematic uncertainties dominate over the statistical errors for most energies. The total error exceeds 10% of the measured value at energies around 9 GeV (for the resolution) and 4 GeV (for the E_{mean}/E_{beam} ratio).

E_{beam} (GeV)	Resolution (%)	Stat. error (%)	Syst. err. from electron cut (%)	Total error (%)
300.00	10.52	0.17	0.14	0.22
250.00	10.79	0.18	0.46	0.50
200.00	11.10	0.19	0.13	0.23
180.00	11.14	0.20	0.61	0.64
150.00	12.08	0.22	0.21	0.30
100.00	12.81	0.23	0.08	0.24
90.00	12.85	0.22	0.19	0.29
80.00	13.90	0.25	0.41	0.48
70.00	14.44	0.27	0.08	0.28
60.00	14.43	0.27	0.64	0.70
50.00	14.98	0.27	0.06	0.27
40.00	16.01	0.28	0.48	0.55
30.00	16.85	0.28	0.75	0.80
25.00	18.25	0.35	0.64	0.73
20.00	19.83	0.38	0.08	0.39
15.00	21.97	0.41	0.53	0.67
10.00	29.16	0.71	1.20	1.39
9.00	33.00	0.74	2.73	2.82
7.00	32.44	0.68	2.65	2.73
6.00	31.97	0.67	1.67	1.80
5.00	30.61	0.74	2.46	2.57
4.00	30.79	0.76	8.36	8.39
3.00	36.94	1.12	9.46	9.52
2.00	40.76	1.29	24.87	24.90
1.50	41.42	1.46	33.91	33.95
1.00	54.20	2.77	31.05	31.18
0.75	65.72	4.64	53.63	53.83
0.50	101.79	22.94	517.76	518.27

Table 13: Systematic uncertainties in the resolution ratio of the simulated energy signal, before weighting and dead material correction, as a consequence of the electron removal cut.

E_{beam} (GeV)	E_{mean}/E_{beam} (%)	Stat. error (%)	Syst. err. from electron cut (%)	Total error (%)
300.00	76.48	0.14	0.01	0.14
250.00	75.85	0.14	0.06	0.15
200.00	75.28	0.14	0.11	0.18
180.00	75.17	0.14	0.13	0.19
150.00	74.67	0.15	0.33	0.37
100.00	73.35	0.16	0.33	0.37
90.00	73.29	0.16	0.40	0.43
80.00	72.48	0.17	0.13	0.22
70.00	72.15	0.18	0.08	0.20
60.00	71.73	0.18	0.68	0.70
50.00	70.81	0.19	0.36	0.40
40.00	70.00	0.20	0.19	0.27
30.00	68.81	0.21	0.36	0.42
25.00	68.19	0.23	0.45	0.50
20.00	66.09	0.24	0.88	0.91
15.00	63.15	0.26	0.76	0.81
10.00	58.49	0.37	1.65	1.69
9.00	57.43	0.41	1.93	1.97
7.00	58.20	0.43	2.02	2.06
6.00	57.19	0.41	1.63	1.68
5.00	55.96	0.41	0.56	0.69
4.00	58.55	0.44	1.74	1.79
3.00	61.39	0.64	7.34	7.36
2.00	65.93	0.83	14.63	14.65
1.50	65.25	0.92	17.69	17.72
1.00	56.98	1.35	16.06	16.12
0.75	49.09	2.02	16.52	16.64
0.50	38.51	5.45	33.04	33.49

Table 14: Systematic uncertainties in the E_{mean}/E_{beam} ratio of the simulated energy signal, before weighting and dead material correction, as a consequence of the electron removal cut.

Acknowledgements

The work presented in this note would not have been possible to do without the help from many people:

We would like to thank Tancredi Carli, Sten Hellman, Peter Loch, Sven Menke, Peter Schacht and Francesco Spanó for valuable suggestions and feedback regarding hadronic calibration.

Sven Menke has performed the important task of implementing the cone-based local hadronic calibration scheme in ATHENA, which enabled the jet study, and also provided us with the necessary help to make it work.

The advice from Martin Aleksa, Tancredi Carli, Vincent Giangiobbe, Hayk Hakobyan, Per Johansson, Nicolas Kerschen, Claudio Santoni and Sasha Solodkov was crucial for our understanding of the combined test beam.

Without Karl-Johan Grahn's help, the dead material corrections in this note would not have existed.

For help with the test beam implementaions in ATHENA, we wish to thank Peter Speckmayer and Sasha Solodkov.

For miscellaneous help we also thank Thomas Burgess, Christophe Clément, Elizabeth Gallas, Ambreesh Gupta, Ana Henriques, Marianne Johansen, Bengt Lund-Jensen and Christin Wiedemann.

Thank you!

List of Figures

List of Tables

References

[1] ATLAS COLLABORATION, *ATLAS Calorimeter Performance Technical Design Report*, Internal Report LHCC 96-40, CERN, 1997.

[2] R. SEUSTER, AIP Conf. Proc. **867** (2006) 274–281.

[3] S. JORGENSEN ROCA, AIP Conf. Proc. **867** (2006) 433–438.

[4] ATLAS COMPUTING GROUP, *ATLAS Computing Technical Design Report* (third revision), Internal Report LHCC-2005-022, CERN, 2005.

[5] C. COJOCARU et al., Nucl. Instrum. Meth. **A531** (2004) 481–514.

[6] Ç. İŞSEVER, K. BORRAS and D. WEGENER, Nucl. Instrum. Meth. **A545** (2005) 803–812.

[7] C. SCHWANENBERGER, Calorimetry in Particle Physics, Pasadena (2002) 761–766, physics/0209026.

[8] S. MENKE, *Local Hadron Calibration Session*, ATLAS Hadronic Calibration Workshop, Milan, Italy, 26 April 2007.

[9] S. AGOSTINELLI et al., Nucl. Instrum. Meth. **A506** (2003) 250–303.

[10] ATLAS COMPUTING GROUP, *ATLAS Computing Technical Design Report*, third revision, Internal Report LHCC-2005-022, CERN, 2005.

[11] THE LHC STUDY GROUP, *The Large Hadron Collider Conceptual Design*, Internal Report AC/95-05 (LHC), CERN, 20 October 1995.

[12] ATLAS COLLABORATION, *ATLAS Technical Proposal*, Internal Report LHCC94-43 LHCC/P2, CERN, 1994.

[13] ATLAS COLLABORATION, *ATLAS Detector and Physics Performance*, ATLAS TDR 14, Internal Report LHCC 99-14, CERN, 25 May 1999.

[14] R.K. BOCK and A. VASILESCU, *The Particle Detector BriefBook*, (Springer, 1998), Web version available at `http://rkb.home.cern.ch/rkb/titleD.html`.

[15] LAR CALORIMETER COLLABORATION, *ATLAS Liquid Argon Calorimeter Technical Design Report*, Internal Report LHCC 96-41, CERN, 1996.

[16] TILE CALORIMETER COLLABORATION, *ATLAS Tile Calorimeter Technical Design Report*, Internal Report LHCC 96-42, CERN, 1996.

[17] R. WIGMANS, *Calorimetry. Energy Measurement in Particle Physics*, (Oxford Science Publications, Oxford, 2000).

[18] B. DI GIROLAMO et al., *Beamline instrumentation in the 2004 combined ATLAS testbeam*, ATLAS technical note, ATL-TECH-PUB-2005-001, CERN, 27 July 2005.

[19] V. GIANGIOBBE, P. JOHANSSON, K. JON-AND and C. SANTONI, *Hadronic calorimeter performance in the ATLAS combined testbeam 2004*, ATLAS note. ATL-TILECAL-PUB-2005-008, CERN, 10 November 2005.

[20] M. ALEKSA, private communication.

[21] *ATLAS Simulation Validation*, http://atlas-computing.web.cern.ch/atlas-computing/packages/simulation/geant4/validation/Validation.html.

[22] S. MENKE, *Status of Weighting: "Standard Approach"*, ATLAS Calorimeter Calibration Workshop, Barcelona, Spain, 7 September 2006.

[23] S. MENKE, *Local hadronic calibration status*, Combined performance: jets/Etmiss/tau meeting, CERN, 27 October 2005.

[24] T. CARLI, private communication.

[25] ROOT, An Object-Oriented Data Analysis Framework, http://root.cern.ch/.

[26] *Combined test beam run list*, period 8, http://atlas.web.cern.ch/Atlas/GROUPS/LIQARGON/Comb_TB/CBT_Barrel/RunLists/RunListp8.txt.

[27] N. KERSCHEN, private communication.

[28] H. HAKOBYAN, private communication.

[29] P. SPECKMAYER, *DATA-MC comparison of pion showers*, CTB LAr+Tile pion analysis meeting at CERN, 13 December 2006.

[30] A. SOLODKOV, private communication.

[31] M. SIMONYAN, H. HAKOBYAN, T. CARLI and A. M. HENRIQUES CORREIA, *Measurement of Pion and Proton Longitudinal Shower Profiles up to 20 Nuclear Interaction Lengths with the ATLAS Tile Calorimeter*, ATLAS communication ATL-COM-TILECAL-2006-014, CERN, 11 December 2006.

[32] W.-M. YAO et al., Journal of Physics G **33** (2006) 1+, Web version available at http://pdg.lbl.gov.

[33] K-J. GRAHN and T. CARLI, *Systematics in pion energy reconstruction using Monte Carlo*, CTB LAr+Tile pion analysis meeting at CERN, 13 December 2006.

[34] S. MENKE, *Status of Out-Of-Cluster Corrections and other Local Hadron Calibration news*, Hadronic Calibration Meeting, CERN, February 21, 2007.

[35] S. MENKE, *Status of Out-Of-Cluster Corrections and other Local Hadron Calibration news*, Hadronic Calibration Meeting, CERN, March 20, 2007.

[36] ATLAS COLLABORATION, *ATHENA - ATLAS Computing framework*, 2007, https://twiki.cern.ch/twiki/bin/view/Atlas/WorkBook.

[37] ATLAS COLLABORATION, *TopoCluster Classification and Weighting CSC note*, Internal Report in preparation, CERN, 2007.

[38] S. MENKE, *Status of Local Hadron Calibration Weights*, Hadronic Calibration Meeting, CERN, 31 October 2006.

[39] S. MENKE, private communication.

[40] A. PRONKO, Acta Phys. Polon. **B36** (2005) 451–460.

[41] B. ANDERSSON, G. GUSTAFSON, G. INGELMAN and T. SJOSTRAND, Phys. Rept. **97** (1983) 31.

[42] S. CHEKANOV, *Jet algorithms: A mini review*, 2002, hep-ph/0211298.

[43] G. BLAZEY et al., *Run II jet physics*, 2000, hep-ex/0005012.

[44] T. SJOSTRAND, S. MRENNA and P. SKANDS, JHEP **05** (2006) 026.

[45] D. CAVALLI, A. GUPTA, F. PAIGE, S. RESCONI and C. RODA, *Jet Reconstruction for Athena 12.0.4*, ATLAS Physics Validation meeting, CERN, 5 December 2006.

[46] M. KANEDA, *Jet Reconstruction in the ATLAS Calorimeters*, Joint Meeting of Pacific Region Particle Physics Communities (DPF-JPS2006), October 2006.

[47] P. KRIEGER, private communication.

[48] G. POSPELOV, *Status of MC studies and dead material corrections*, Hadronic Calibration Meeting, CERN, 6 June 2007.

[49] T. CARLI, *Summary of G4 validation results of ATLAS and CMS*, the GEANT4 review 2007, CERN, 16 April 2007.